Radboud Repository

Radboud University Nijmegen

PDF hosted at the Radboud Repository of the Radboud University Nijmegen

The following full text is a publisher's version.

For additional information about this publication click this link.
http://hdl.handle.net/2066/146220

Please be advised that this information was generated on 2018-07-07 and may be subject to change.

A luminosity measurement at LEP using the L3 detector

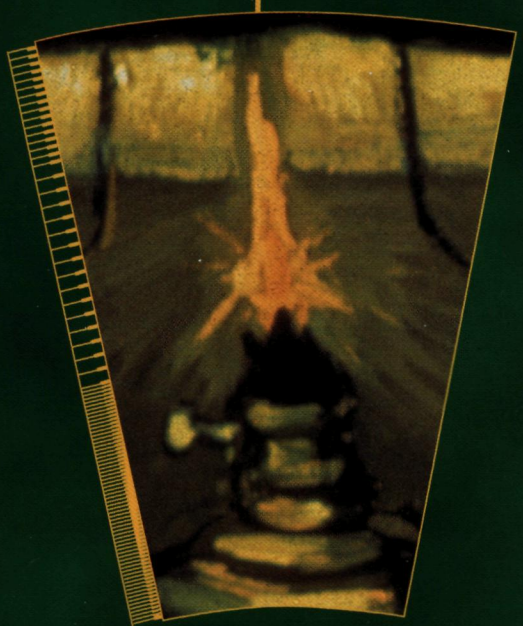

E.N. Koffeman

Cover detail:
De aardappeleters, Nuenen 1885
Vincent van Gogh
Amsterdam, Van Gogh Museum
(Vincent van Gogh Stichting)

Cover design: Jaap Joziasse
Cover photo: Loek van Beers
Prepress: Hennie Spermon

A luminosity measurement at LEP using the L3 detector

Een wetenschappelijke proeve op het gebied
van de Natuurwetenschappen.

Proefschrift

ter verkrijging van de graad van doctor
aan de Katholieke Universiteit Nijmegen,
volgens besluit van het College van Decanen
in het openbaar te verdedigen
op 25 Juni 1996,
des namiddags te 15.00 uur precies,

door

Elisabeth Nikolaja Koffeman

geboren op 3 november 1967 te Nuenen.

Promotores: **Prof. Dr P. Duinker**
Prof. Dr F. L. Linde
Co-promotor: **Dr M. H. M. Merk**

Manuscriptcommissie: **Dr D. J. Schotanus**
Dr G. J. Bobbink

The work described in this thesis is part of the research programme of the 'Nationaal Instituut voor Kernfysica en Hoge-Energie Fysica (NIKHEF)'. The author was financially supported by the 'Stichting voor Fundamenteel Onderzoek der Materie (FOM)'.

ISBN: 90-9009549-7

Un savant dans son laboratoire n'est pas seulement un technicien c'est aussi un enfant placé en face des phénomènes naturels qui l'empressionnent comme un conte de fées Nous ne devons pas laisser croire que tout progrès scientifique se réduit a des mécanismes, des machines, des engrenages, qui, d'ailleurs ont aussi leur beauté propre

Marie Curie-Sklodowska (1867–1934)

Contents

Introduction

The present understanding of matter and forces in our universe is the result of an everlasting interplay between the development in theory and experiment. The theoretical model describing the interactions between elementary particles to our best present knowledge is the Standard Model. One way to study the interactions experimentally is the use of a particle collider.

At CERN near Geneva a large collider is constructed (LEP) where electrons and their anti particles are brought into collision. The electrons and positrons are injected in a circular tunnel with a length of 27 km. At four points the particle beams collide and large detectors have been constructed to study the results of these collision processes. The LEP machine is specially designed to study the weak interactions. Millions of Z bosons - the boson responsible for the weak neutral current interaction - are produced and its properties are studied in detail and with high precision.

To perform high precision measurements at particle colliders it is crucial to know the exact intensity of the colliding beams. In particle physics this quantity is generally referred to as the luminosity. The determination of the luminosity in one of the experiments (L3) is the topic of this thesis. The implementation and the use of a silicon strip detector in L3, will be described in detail.

In chapter one the most important parameters measured at LEP are discussed, preceded by a short introduction to the Standard Model. The process generally used for luminosity measurements in electron positron colliders is small angle Bhabha scattering. This process is discussed at the end of chapter one. In chapter two the characteristics of the collider and the L3 experiment are given. Together with the signature of the small angle Bhabha scattering, these experimental conditions determine the specifications for the design of the luminosity monitor.

The general features of silicon strip detectors for their application in high energy physics are presented in chapter three. Some special attention is given to the behaviour of the sensors used for the tracking detector in the luminosity monitor. The more specific design details of the luminosity monitor are constricted to chapter four.

In chapter five the conversion from detector signals into coordinates relevant for the analysis is explained. The selection of the small angle Bhabha scattering events and the subsequent determination of the luminosity, are presented in chapter six. Systematic uncertainties are carefully studied. Important for a good understanding of the Bhabha selection are the events where a photon is produced in the scattering process. These events are separately studied. In chapter seven a comparison is presented between the radiative events observed in the data an their modelling in the Bhlumi Monte Carlo programme.

Chapter 1

Theory

1.1 Introduction

The purpose of this chapter is to emphasise the importance of the luminosity measurement and to give a theoretical description of the process used for this measurement small angle Bhabha scattering

The chapter starts with a short introduction to the Standard Model Its basic concepts need to be understood in order to put the experimental results in perspective

Subsequently a description is given of the most important parameters measured at the Large Electron Positron collider at CERN The LEP collider is designed such that the total available energy in a collision can be adjusted to the mass of the neutral mediator of the weak interactions, the Z boson Under these conditions the probability of the process of electron positron annihilation into a Z boson is strongly enhanced The LEP collider therefore provides a unique environment to study the weak interaction processes

In the last part of this chapter the theoretical calculation of the Bhabha scattering cross section is given A first order approximation is presented as this leading order behaviour is used to determine most detector design specifications Higher order predictions are discussed since their precision remains one of the limiting factors in the final luminosity determination

1.2 The Standard Model

1.2.1 Particles and fields

The search for unification of different theories explaining a variety of observable phenomena is one of the driving forces of (particle) physicists In the past Maxwell achieved an important step in this unification with the description of the electric and magnetic forces in one theory

Many years later a new theory was developed by Glashow, Weinberg and Salam [1, 2, 3] which unifies the weak interactions with the electromagnetic force The Standard Model of electroweak interaction The model describes the interaction between elementary particles caused by electroweak forces Although the strong interactions are also implemented in the Standard model framework they are not specifically discussed here

The particles with spin = 1/2 the fermions, are divided into quarks and leptons Furthermore

FERMIONS spin = 1/2				
generation	quarks		leptons	
	Q=2/3	Q= 1/3	Q=-1	Q=0
1	u	d	e	ν_e
2	c	s	μ	ν_μ
3	t	b	τ	ν_τ

BOSONS spin = 1	
mediator	field
photon (γ)	electromagnetic
W^+, W^-, Z	weak
gluon (g)	strong

Table 1.1: *The basic constituents of matter and the mediators of the fundamental forces (Q is the charge in units of the elementary charge e)*

the quarks and leptons can be subdivided into different generations ordered by increasing mass Such a generation or family, contains two quarks and a lepton with its corresponding neutrino The neutrinos are believed to be massless The number of generations is not predicted by the Standard Model It can be determined from measurements performed at LEP

An important difference between quarks and leptons is the fact that quarks feel the strong forces whereas the leptons are not sensitive to this interaction Due to the strong force quarks are confined, so far they have only been observed in bound states Bound states of quarks are called hadrons and consist of either two quarks (mesons) or three quarks (baryons) The proton and the neutron are examples of bound quark states The proton contains two up quarks and one down quark (uud) The neutron is a combination of two down quarks and one up quark (udd) Together with the most familiar lepton (the electron), the proton and the neutron are the construction blocks of all atoms known from the periodic table of elements

An interaction between elementary particles can be interpreted as the exchange of bosons, which are particles with spin = 1 The electromagnetic attraction between two charged particles for example, can be represented as the exchange of a photon In a similar way the gluons (in the Standard Model eight different types of gluons exist) are the mediators for the strong force and the W^+, W and Z bosons the mediators for the weak force

The existence of another boson, with spin = 0, is predicted by the model the Higgs boson, but it has not yet been observed In the Standard Model the presence of the Higgs boson is required to explain the masses of the elementary particles The experimentally observed elementary particles are given in table 1 1 The τ neutrino has not been observed in direct measurements

1.2.2 GWS model

Starting in the sixties Glashow, Weinberg and Salam developed a method to describe the weak interactions coherently with the theory for electromagnetic interactions The model predicts the existence of three massive vector bosons in addition to the massless, neutral photon Two charged

bosons (the W^+ and the W^-) and one neutral boson (the Z boson) The W boson couples to a lepton and its corresponding anti-neutrino or to a quark pair in which case transitions between different generations are even allowed The Z boson couples to leptons and quarks but the fermion flavour does not change in this interaction The allowed vertices with their strengths are shown in figure 1 1

The Standard Model does not constrain all the parameters in fundamental interactions Since the parameters are related some freedom exists in the choice of the input parameters This relation is mostly due to the mixing of the electromagnetic and weak fields which can be parametrised by the weak mixing angle θ_w Once the value of this angle is known the coupling strength of the Z boson to the fermions can be calculated (see figure 1 1)

If the masses of the fermions and bosons are used as input parameters the Standard Model prediction for the weak mixing angle is in a lowest order approximation expressed as

$$\sin^2 \theta_w = 1 - \frac{M_W^2}{M_Z^2} \approx 0\,23 \tag{1 1}$$

The mass of the W boson is usually replaced by the Fermi constant (G_μ) which is determined with more accuracy The relation between the Fermi constant and the mass of the W boson is given by

$$G_\mu = \frac{\pi\alpha}{\sqrt{2}} \frac{1}{M_W^2 sin^2\theta_w} \tag{1 2}$$

where α is the fine structure constant and equal to 1/137

1.3 The Z boson

1.3.1 Decay modes

Strong support for the believe in the validity of the Standard Model was obtained with the discovery of the W boson and the Z boson with masses close to their prediction However, still many parameters are predicted by the Standard Model which remain to be tested One of the largest experiments designed to put the Standard Model at trial is the LEP collider built at CERN near Geneva The most important parameters on the collider can be found in chapter two At LEP phase 1, electrons and positrons collide with centre of mass energies around 90 GeV The advantage of studying collisions at this energy is the resonance behaviour of the weak force due to the fact that there is enough energy available for the production of a real Z boson As a result reactions can be studied where the electromagnetic interactions between the particles are no longer dominant with respect to the weak interaction

The lowest order processes which are allowed are governed by the exchange of a Z boson or a photon The Feynman diagrams [1] for these processes are shown in figure 1 2 The main reaction of interest is the reaction where an electron and a positron annihilate to a Z boson which subsequently decays into a (final state) fermion pair Through study of each of these final states separately (muons, electrons, taus, quarks and neutrinos) the Standard Model can be tested extensively The ratio of the observed number of Z bosons decaying into a specific fermion pair over

[1] In all Feynman diagrams in this thesis the chronology is from the left to the right

VERTICES

photon $iQe\gamma^{\mu}$

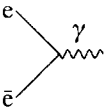

W boson $\frac{-ie\gamma^{\mu}(1-\gamma^{5})}{2\sqrt{2}\sin\theta_{w}}$

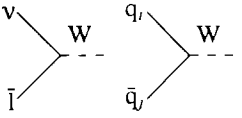

Z boson $\frac{-ie\gamma^{\mu}(g_{v}-g_{a}\gamma^{5})}{2\sin\theta_{w}\cos\theta_{w}}$

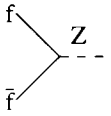

	g_v	g_a
$\nu_{e,\mu,\tau}$	$\frac{1}{2}$	$\frac{1}{2}$
e, μ, τ	$-\frac{1}{2}+2\sin^2\theta_w$	$-\frac{1}{2}$
u, c, t	$\frac{1}{2}-\frac{4}{3}\sin^2\theta_w$	$-\frac{1}{2}$
d, s, b	$-\frac{1}{2}+\frac{2}{3}\sin^2\theta_w$	$-\frac{1}{2}$

Figure 1.1: *Vertex factors needed in Feynman's calculation of probabilities of interactions between elementary particles. In the factors 'e' is the charge of the positron and γ^{μ} represent the Dirac matrices. In the diagrams 'e' is any charged particle, 'f' is a fermion and 'l' is any lepton with its corresponding (anti)neutrino ν. 'q_i' is a u,c or t quark and 'q_j' is a d,s or b quark.*

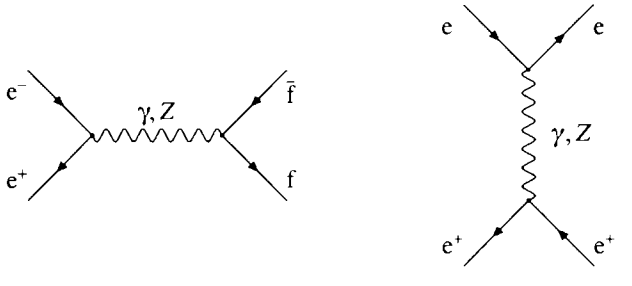

Figure 1.2: *The lowest order Feynman diagrams for the exchange of a γ or Z boson representing respectively the s-channel and the t-channel exchange*

decay	branching ratio
hadrons	69 9 ± 0 2 %
electrons	3 357 ± 0 008 %
muons	3 36 ± 0 01 %
taus	3 37 ± 0 01 %
invisible	20 0 ± 0 1 %

Table 1.2: *The decay of the Z boson and its branching ratios Numbers obtained from the combined LEP experiments*

the total number of observed decays (hence into any fermion pair) is called the branching ratio From the combined data of all four LEP experiments [4] the branching ratios are determined and given in table 1 2

1.3.2 Cross section

The probability for the annihilation of an electron and a positron into a Z boson subsequently decaying into a fermion pair is expressed in terms of a cross section Experimentally it is determined by counting the number of events, N, in which a fermion pair is observed This number of events is than normalised with the collision intensity The cross section, σ, therefore is given by

$$\sigma = \frac{N}{\mathcal{L}} \tag{1 3}$$

where $\mathcal{L}$ is the luminosity The luminosity itself is determined from the measurement of a process with a theoretically well known cross section, *e g* small angle Bhabha scattering (see the following section)

The cross section of the process $e^+e^- \rightarrow Z \rightarrow f\bar{f}$ is strongly dependent on the centre of mass energy, $\sqrt{s}$ Standard parameters for the Z boson are obtained from the line shape analysis, the measured cross section of the process $e^+e^- \rightarrow Z \rightarrow ff$ is plotted as a function of $\sqrt{s}$ and the result is fitted to a Breit Wigner distribution An example of such a distribution is shown in figure 1 3 The Breit Wigner distribution is parametrised by three quantities

1 **Peak position.**
The position of the peak on the $\sqrt{s}$ axis represents the mass of the Z boson, M_Z

2 **Peak height.**
The peak height of the cross section distribution is related to the branching ratio of the process under study The total height of the peak (when the cross sections of all fermion channels are added) is determined by the unitarity limit

3 **Peak width.**
The width of the distribution represents the total decay width Γ_Z, of the Z boson and hence its lifetime ($\tau = \frac{1}{\Gamma}$)

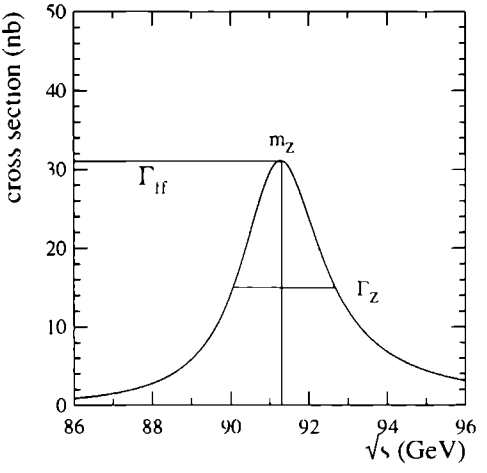

Figure 1.3: *Sketch of the cross section of the process $e^+e \rightarrow Z \rightarrow f\bar{f}$ plotted as function of the centre of mass energy*

To first order the cross section without any contribution from the electromagnetic interaction is given by the equation

$$\sigma_0 = \frac{12\pi\Gamma_{Z\rightarrow ee}\Gamma_{Z\rightarrow ff}}{M_Z^2}\frac{s}{(s-M_Z^2)^2+M_Z^2\Gamma_Z^2} \tag{1.4}$$

This equation provides an accuracy of one percent If a higher accuracy is needed electroweak corrections have to be implemented

Since the mass and the decay width of the Z boson are determined from the horizontal position of the peak of the Breit-Wigner distribution they are to a large extend insensitive to differences in the vertical scale of the distribution, in other words these two parameters are not affected by an overall shift in the luminosity measurement The luminosity determination should still have a small statistical error, high reproducibility and a well known dependence on $\sqrt{s}$ Preferentially it should not even depend too much on $\sqrt{s}$

1.3.3 The number of light neutrino species

The total width of the Z-resonance, Γ_Z, equals the sum of the widths of its decay products According to the Standard Model the Z boson couples to all fermions and the width can be expressed as

$$\Gamma_Z = \Gamma_{Z\rightarrow qq} + 3\,\Gamma_{Z\rightarrow ll} + N_\nu\,\Gamma_{Z\rightarrow\nu\nu} \tag{1.5}$$

where N_ν is the number of neutrino families and $\Gamma_{Z\rightarrow\nu\nu}$ is the decay width of the Z boson into a neutrino pair Obviously this is only true for neutrinos which are lighter than half the Z mass, otherwise they would not contribute to the width of the Z resonance

The measurement of the number of neutrinos using these partial widths requires the partial width of the invisible decay of the Z, $\Gamma_{Z\to\nu\nu}$, as input This can be calculated in the Standard Model, however the result is very sensitive to the masses of the top quark and the Higgs boson Although the mass of the top quark is at present measured at Fermi lab, the Higgs mass is still unknown Since the widths of the Z decaying into leptons and neutrinos depends in a similar way on these masses the problem can be circumvented with the help of the following expressions

$$\begin{aligned} N_\nu &= \Gamma_{\rm inv}/\Gamma^{SM}_{Z\to\nu\nu} \\ &= (\Gamma_Z - \Gamma_{Z\to qq} - 3\Gamma_{Z\to ll})/\Gamma^{SM}_{Z\to\nu\nu} \\ &= \left(\frac{\Gamma_Z - \Gamma_{Z\to qq}}{\Gamma_{Z\to ll}} - 3\right)\left(\frac{\Gamma_{Z\to ll}}{\Gamma_{Z\to\nu\nu}}\right)^{SM} \end{aligned} \tag{1 6}$$

Using equation 1 5 the expression for the number of neutrinos is

$$N_\nu = \left(\sqrt{\frac{12\pi}{M_Z^2\sigma_{Z\to ll}}} - \frac{\sigma_{Z\to qq}}{\sigma_{Z\to ll}} - 3\right)\left(\frac{\Gamma_{Z\to ll}}{\Gamma_{Z\to\nu\nu}}\right)^{SM} \tag{1 7}$$

The experimental error on the determination of the number neutrinos is strongly dependent of the systematic error on the luminosity measurement The desire to increase the accuracy of the determination of the number of neutrinos has been one of the main reasons to upgrade the L3 luminosity monitor

1.4 Small angle Bhabha scattering

1.4.1 Introduction

Bhabha scattering is the processes where both the initial and the final state consist of an electron and a positron The most important properties of small angle Bhabha scattering are summarised below (in fact these are requirements for any type of process that could be used for a luminosity measurement)

1 **Large cross section.**
The cross section is high compared with the cross section of the reactions used to study the Z lineshape The statistical uncertainty in the luminosity determination is then not a limiting factor in the determination of the electroweak parameters

2 **Clear experimental signature.**
The final experimental systematic uncertainty in the luminosity measurement heavily depends on the purity of the identification of small angle Bhabha events The amount of data collected with the L3 detector and the resulting high precision needed for the luminosity determination require a high precision detector and an extensive study of detector performance

3 **Well known cross section.**
Uncertainties in the calculations of the cross section limit the precision of the luminosity determination Small angle Bhabha scattering is dominated by the exchange of a photon

and can therefore be calculated with high accuracy using QED calculations. Given the accuracy level required at current LEP physics a small correction due to interference with the exchange of a Z boson has to be taken into account.

1.4.2 First order QED cross section

In this section a lowest order derivation is given of the theoretical value of Bhabha scattering cross section. Allowing an additional photon in the final state, all events of the type

$$e^+e^- \rightarrow e^+e^-(\gamma) \tag{1.8}$$

are called Bhabha scattering.

For two body-scattering in the centre of mass frame the 'Golden Rule' for the differential cross section reduces to

$$\frac{d\sigma}{d\Omega} = \frac{S|\mathcal{M}|^2}{64\pi^2 s}\frac{|p_i|}{|p_f|} \tag{1.9}$$

where S is a statistical factor equal to $1/j!$ for j identical particles in the final state: in this case $S = 1$. The momenta of the incoming and outgoing particles are equal: $|p_f|$ equals $|p_i|$. The matrix element, $\mathcal{M}$, is calculated using the Feynman diagrams [2]. To calculate the QED part of this process in first order the following diagrams are involved:

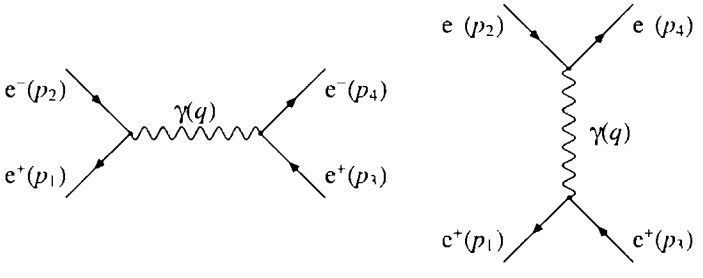

The diagrams represent respectively the photon exchange in the s-channel and in the t-channel. Calculation of the matrix element of these diagrams leads to the following contributions

$$\begin{aligned}\mathcal{M} &= \mathcal{M}_{t-channel} + \mathcal{M}_{s-channel} \\ &= \frac{-g_e^2}{(p_2-p_4)^2}[\bar{v}(p_2)\gamma_\mu v(p_4)][\bar{u}(p_3)\gamma^\mu u(p_1)] \\ &\quad -\frac{g_e^2}{(p_1+p_2)^2}[\bar{v}(p_2)\gamma_\nu u(p_1)][\bar{u}(p_3)\gamma^\nu v(p_4)]\end{aligned} \tag{1.10}$$

with $g_e = \sqrt{4\pi\alpha}$ and u and v are the Dirac spinors for the electron and the positron. When calculating the square of this matrix element it is useful to introduce the Mandelstam variables which make the equation more compact.

$$\begin{aligned}s &= (p_1+p_2)^2 = 4E_{beam}^2 \\ t &= (p_2-p_4)^2 = 2E_{beam}^2(\cos\theta - 1) \\ u &= (p_3-p_2)^2 = -2E_{beam}^2(\cos\theta + 1)\end{aligned} \tag{1.11}$$

[2] A good introduction to the application of the Feynman rules can be found in reference [5]

In the rest of this chapter cos θ will be written as c. The average matrix element squared than reads as

$$\left\langle |\mathcal{M}|^2 \right\rangle = 4g_e^4 \left(\frac{s^2+u^2}{t^2} + \frac{2u^2}{st} + \frac{t^2+u^2}{s^2} \right) \tag{1.12}$$

When the value of the matrix element is substituted in the equation for the cross section the following differential cross section is obtained

$$\frac{d\sigma}{d\Omega} = \left(\frac{\alpha^2}{4s} \right) \frac{(3+c^2)^2}{(1-c)^2} \tag{1.13}$$

There is a divergence when the scattering angle θ, approaches zero. This reflects the fact that the coulomb potential has an infinite range. At these small angles the momentum transfer is small. Since the cross section is large at small angles the luminosity detectors are located at very small angles. If the detectors cover the full azimuthal angle and in polar angle, θ, range from θ_{min} to θ_{max} the total visible cross section is

$$\sigma = \frac{16\pi\alpha^2}{s} \left(\frac{1}{\theta_{min}^2} - \frac{1}{\theta_{max}^2} \right) \tag{1.14}$$

This lowest order cross section calculation is called the Born approximation.

1.4.3 Corrections to the Born QED cross section

Electroweak interference

Although the QED contribution to Bhabha scattering is by far the most important, the annihilation of the electron positron pair into a Z boson has to be taken into account. This contribution can be calculated in the same way as the Born QED cross section, by replacing the photon with the Z boson in the relevant Feynman diagrams.

The total cross section depends on the matrix element squared, which consists of the following contributions

$$\mathcal{M} = \mathcal{M}_{\gamma(t)} + \mathcal{M}_{\gamma(s)} + \mathcal{M}_{Z(t)} + \mathcal{M}_{Z(s)} \tag{1.15}$$

The products of the first two terms are present in the first order QED cross section given in equation 1.14. From the other products the most significant terms are the so called $\gamma - Z$ interferences resulting in a cross section expressed as

$$\begin{aligned} \frac{d\sigma}{d\Omega} = & \left(\frac{\alpha^2}{s} \right) \\ & \left[\chi(s) \frac{1}{2} (g_v^2(1+c^2) + 2g_a^2 c) + \right. \\ & \chi(t) \frac{4(g_v^2 - g_a^2) + (g_v^2 + g_a^2)(1+c)^2}{(1-c)^2} + \\ & \left. (\chi(s) + \chi(t)) \frac{(g_v^2 + g_a^2)(1+c)^2}{2(1-c)} \right] \end{aligned} \tag{1.16}$$

where $\chi(s)$ and $\chi(t)$ are the Breit-Wigner terms of the Z resonance [6] Although this is also an $\mathcal{O}(\alpha^2)$ contribution the correction is numerically small for small polar angles For large polar angles however the exchange of a Z boson in the s channel is dominant and it is in fact used to calculate some of the electroweak parameters The effect of the γ-Z interference is plotted in figure 1 4

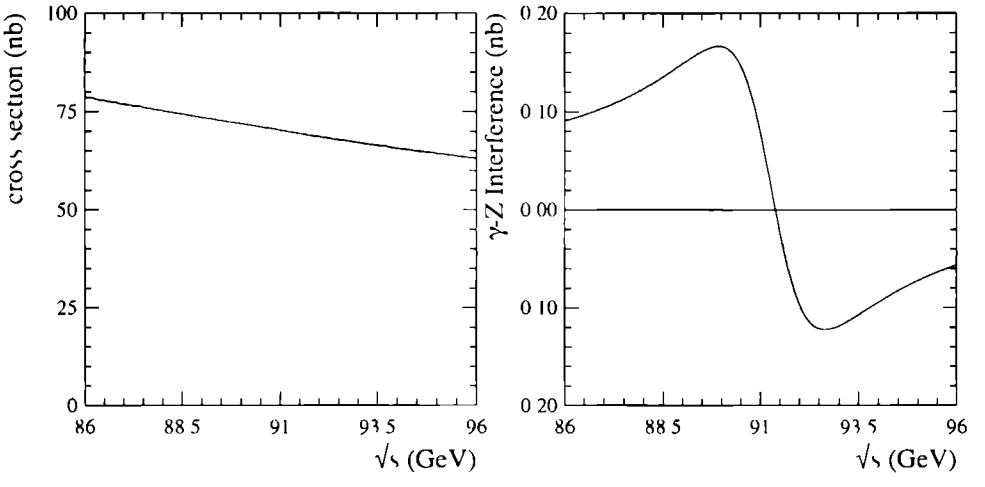

Figure 1.4: *The contribution of the Z(s)γ(t) interference (right) compared to the first order QED part (left) The cross sections are integrated over an angular range from 32 to 54 mrad*

QED corrections

In the data analysis a delicate set of requirements is used to select a sample of Bhabha events with a well defined detector acceptance Due to these constraints on the phase space of the particles in the final state the cross section is determined with the help of a Monte Carlo simulation This technique allows a change of the selection criteria without the need to recalculate the total cross section

The disadvantage of this method as opposed to the analytical calculation is that the cross section of intermediate processes used in the derivation of the total cross section need to be positive and finite The higher QED corrections to the Born cross section are divided into virtual photon loops and real bremsstrahlung Considering only the first order corrections (one loop diagrams) the cross sections are found to be divergent for small values of the momentum of the additional photon, k Part of the bremsstrahlung correction is added to virtual photon correction to solve this problem all photons with a momentum below a cut-off value k_0 are considered as virtual photons This procedure is justified since virtual photons with no energy are indistinguishable from real photons with no energy

From an experimental point of view this value of k_0 should be as low as possible but there is a problem For small values of k the cross section for the soft photons (virtual plus soft brems-

strahlung) becomes negative To overcome this problem the higher order terms of the QED corrections are considered Summing the leading logarithmic terms of all higher order corrections an exponential form is obtained which solves the problem The implementation of this exponentiation' method in the Monte Carlo simulation has first been developed by Yennie, Frautschi and Suura The event generator Bhlumi is based on the use of this method [7]

Visible cross section

The Monte Carlo event sample used for the analysis in this thesis, has been generated with the Monte Carlo program Bhlumi version 2 01 [8] The accuracy on the generated cross section is claimed to be 0 25% Recently a new version of Bhlumi has been released with an improved accuracy of 0 16% [9] Unfortunately the time involved in the simulation of the detector response on the generated events is such that the event sample could not be replaced Comparison of the cross section on generator level showed that the cross section does not change between the two versions of Bhlumi and therefore the error on the theoretical cross section is estimated to be 0 16%

In total 4 1 million events have been generated requiring the momentum transfer t to be in the range $0\ 83 < t < 83$ GeV The corresponding range of the scattering angle of the electron is $20 < \theta < 200$ mrad The event sample is generated at an energy of $\sqrt{s}$=91 25 GeV

The exact dependence of the cross section on the centre of mass energy is determined with Bhlumi version 4 02 and is close to the expectation from the Born approximation To obtain the cross section at an energy $\sqrt{s'}$, the cross section is scaled with a factor $\mathcal{F}_{s/s} = (s/s')^{0\ 9933}$

The small γ-Z interference, discussed in the previous section, has to be taken into account as well To calculate this correction the polar range is taken to be $32 < \theta < 54$ mrad In version 4 02 the calculation of the γ-Z interference has been substantially improved To make use of this improved calculation in the events generated with version 2 01 the difference in the γ Z contribution between the two version has been determined For each centre of mass energy point the γ-Z interference is calculted seperately, $\mathcal{F}_{\gamma\ /}$ The precise visible cross section including the exact detector acceptance is determined after the data sample has been analysed The generated cross section, $\sigma(91\ 25)$ is corrected for the centre of mass energy and the γ-Z interference for each LEP fill seperately The total cross section is thus obtained by

$$\sigma_{\text{Bhlumi}}(s) = \sigma(91\ 25)\ \ \mathcal{F}_{\gamma-Z}\ \ \mathcal{F}_{s/s} \tag{1 17}$$

The numerical results foi these values are are presented in chapter 6

Chapter 2

LEP and L3

2.1 Introduction

Close to the city of Geneva a Large Electron Positron collider (LEP) has been constructed to study the electroweak interactions between elementary particles The electron and positron beams are accumulated in a storage ring and brought into collision at four intersection points To enable the study of both the Z and the W boson the centre of mass energy of the machine was designed to range from 80 to 200 GeV

The first studies on the design of a large electron positron storage ring at CERN date from 1976 [10] In the summer of 1989 the beams were injected into the ring and the first decays of the Z boson were observed During the LEP phase I (1989-1995) the beam energies are tuned to range from 44 to 47 GeV The resulting centre of mass energies of the colliding e^+e^- pair are thus close to the Z mass of about 91 GeV

This chapter starts with a description of the LEP machine Subsequently the L3 detector is introduced Extra attention is given to the BGO calorimeter of the luminosity monitor

2.2 The Large Electron Positron collider

2.2.1 The accelerator

The size of a storage ring is closely related to the energy range of the stored beams Bending charged particles causes them to lose energy through the process of synchrotron radiation The energy loss per turn is given by [11]

$$\Delta E = \frac{4\pi}{3} \frac{r_e}{\rho} \frac{E_{beam}^4}{m_e^3} \tag{2.1}$$

where m_e and r_e are the mass and the classical radius of the electron, E_{beam} is the beam energy and ρ is the radius of the storage ring With a beam energy of 45 GeV this leads to an energy loss of 100 MeV per turn for one electron (positron)

The energy loss is compensated by the radio frequency (RF) acceleration system At the time LEP was designed, an upper limit on the feasible RF power was assumed to be 100 MW To enable LEP phase II, with foreseen beam energies up to 100 GeV and a current per beam of 3 mA, this

leads to an optimum bending radius of 3.5 kilometres. Together with the need for extra space to house the RF cavities this resulted in a ring with a circumference of 26.7 kilometres with 8 bending sections and 8 straight sections.

In figure 2.1 the location of the storage ring is indicated as well as the interaction points at which the four detectors are built: L3, Aleph, Opal and Delphi.

At the point of injection in the LEP storage ring the electrons and the positrons are already accelerated to 20 GeV. The acceleration process starts with a linear accelerator (LIL), producing electrons of 200 MeV. At a stationary target these electrons generate positrons. With the next, linear accelerator these electrons and positrons are brought to an energy of 600 MeV.

After accumulation in an electron positron accumulator (EPA) the particles are injected into the proton synchrotron (PS) which accelerates the particles to 3.5 GeV. Subsequently the particles are accelerated even further in the super proton synchrotron (SPS). In the SPS the energy of the particles reaches 20 GeV; sufficient for injection in the LEP ring. After the injection in LEP (filling) the beams are accelerated to the required energy. Finally the beams are brought into collision in the four interaction points and the collision rate is optimised. When the collision rate starts to decrease too much, the beams are dumped and the machine is refilled. The average lifetime of a fill is around 20 hours, while the time needed to fill LEP is approximately half an hour.

Both the PS and the SPS were designed for the acceleration of proton beams and were used long before the construction of LEP. After modifications it became possible to use the synchrotons in a multi-cycle mode which enables the production of electron (positron) beams in parallel with other particle beams used in the other experiments at CERN.

The energy calibrations of the electron and positron beams are a crucial aspect in all cross section measurements. They are performed by the LEP machine group for every fill. The precision of the calibration has improved substantially over the years. Surprising are the variations on the energy due to the tidal forces, the water level in the lake of Geneva, the amount of rain in the Jura mountains and the passing of the TGV on its way from Geneva to Lyon. The change in energy by the tidal forces (the actual shape of the ring is slightly deformed and therefore the orbit of the particles through the magnets is changed) is the largest and in the order of 10 MeV [12].

The best energy calibration has an uncertainty of 1.7 MeV [12]. For the 1993 data the error on the mass of the Z boson due to the LEP energy calibration is 1.4 MeV [13].

2.2.2 The luminosity

At LEP the electrons circulate in one direction, concentrated in small bunches equally spaced in the ring. Likewise bunches of positrons circulate in opposite direction. The production rate of Z bosons at the interaction points is proportional to the 'collision' rate at the interaction point: the luminosity. For head on electron and positron collisions, the luminosity is defined as

$$\mathcal{L} = \frac{N_e \cdot N_p \cdot k \ f_r}{4\pi \cdot \sigma_x^* \sigma_y^*} \tag{2.2}$$

where N_e (N_p) is the number of electrons (positrons) in a bunch, k is the number of bunches in one beam and $\sigma_x^* \sigma_y^*$ is the area of the colliding bunches, f_r is the revolution frequency given by the circumference of the ring divided by the velocity of light. Increasing the luminosity is hindered by the electromagnetic interaction between the two beams. Taking this 'beam-beam' force into

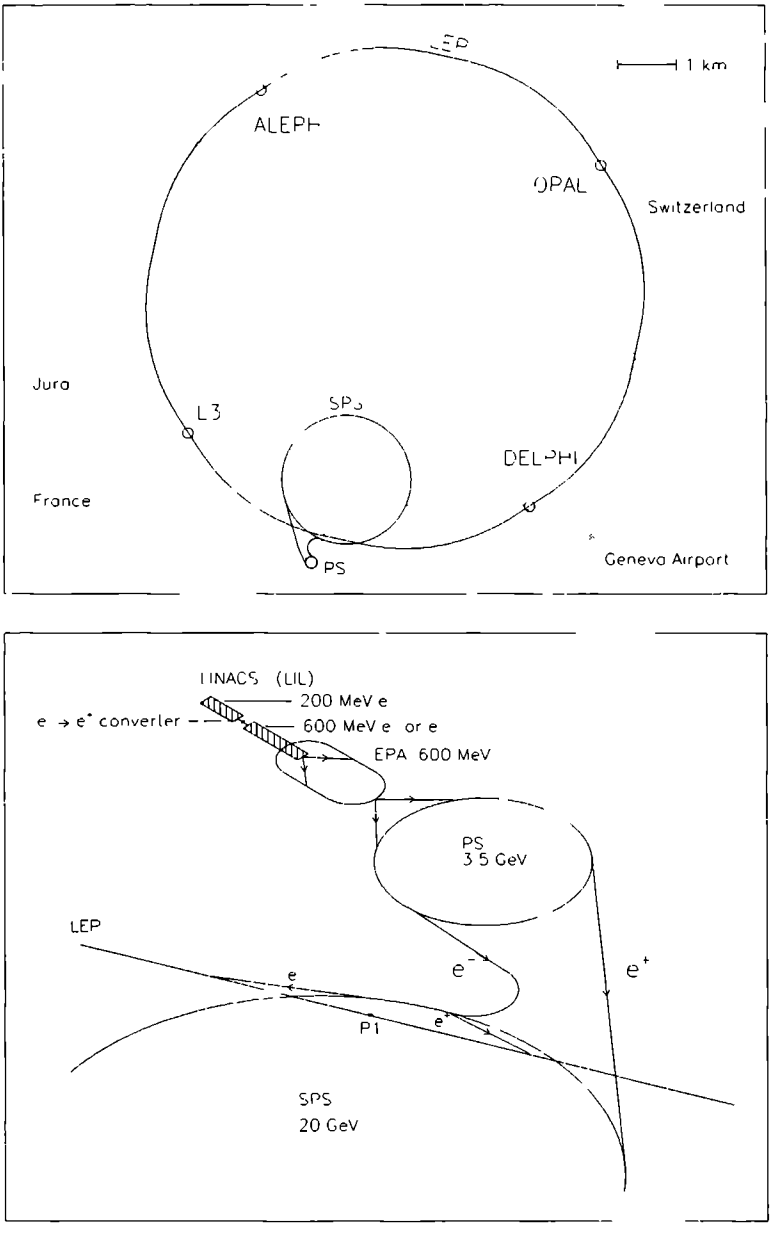

Figure 2.1: *The location of the LEP ring near Geneva (top) The electrons and positrons are accelerated to 20 GeV before they are injected in the storage ring (bottom) The maximum acceleration energy for the electrons and positrons, of the different accelerators of the injection system is indicated*

account, the equation for the luminosity becomes

$$\mathcal{L} = \frac{E_{beam} \quad f_r \quad k \quad N_b \quad \xi_y}{2 m_e \quad r_e \quad \beta_y} \tag{2 3}$$

where N_b is the average number of particles per bunch, ξ_y is the beam strength parameter representing the size of the beam-beam force It is inversely proportional to the third power of the beam energy [11] β_y^* is the betatron amplitude function specifying the focusing strength at the collision points A low value of beta corresponds to strong focusing The luminosity is increased by optimising the beam spot and the total number of particles in the ring in the following way

1 **Minimising the betatron amplitude function.**
The parameter β_y^* can be reduced by strong focusing For this purpose strong quadrupole magnets are used close to the experiments, the low beta magnets The minimal value of β_y^* is essentially determined by the chromatic aberrations in these magnets due to small variations in the beam energy the trajectories of the particles through the magnets are not all exactly similar, thus distorting the focusing effect Moreover the beam strength parameter is a function of the beam spot size and therefore the luminosity does not necessarily increase when the beam spot is squeezed

2 **Increasing the total beam current.**
The number of bunches must be at least two for each type, to provide all four experiments with colliding beams However, if the number of bunches is higher, they cross each other outside the experiments as well To prevent a large loss of intensity due to beam-beam interaction at these points, the beams can be separated by electrostatic plates For the separation of the bunches in the 8 bunch mode of LEP, the beams are brought into an orbit which slowly oscillates around the centre of the beam pipe Details on this special scheme of beam separation, the Pretzel scheme, can be found in [14]

Another effect prohibiting a high luminosity is the interaction amongst the bunches of one type, this coupling increases when the distance between two bunches decreases This effect is mainly caused by the field produced in the RF cavities when the particles pass Within the bunches this mechanism limits the number of particles in one bunch In 1993 LEP was operated with 8 electron and 8 positron bunches

Increasing the beam current always requires extra RF power which is a practical limit to the maximum luminosity as well

In table 2 1 the original LEP design specifications are compared with the results of 1993 [12] In figure 2 2 the delivered luminosity to the L3 experiment is shown The luminosity is expressed in inverse picobarn

2.3 The L3 detector

A detailed description of the layout and the performance of the L3 detector can be found in [15, 16] The design of the detector is optimised for the measurement of photons, electron and muons To enable the momentum determination of charged tracks the L3 detector is contained in a large

Parameter	design value	achieved
total current (mA)	6.0	10.0
vertical beam strength	0.03	0.049
betatron amplitude function (m)	0.07	0.037
peak luminosity (10^{30} cm $^{-2}$ s $^{-1}$)	13	24

Table 2.1: *Design parameters of the LEP collider and the best obtained performance.*

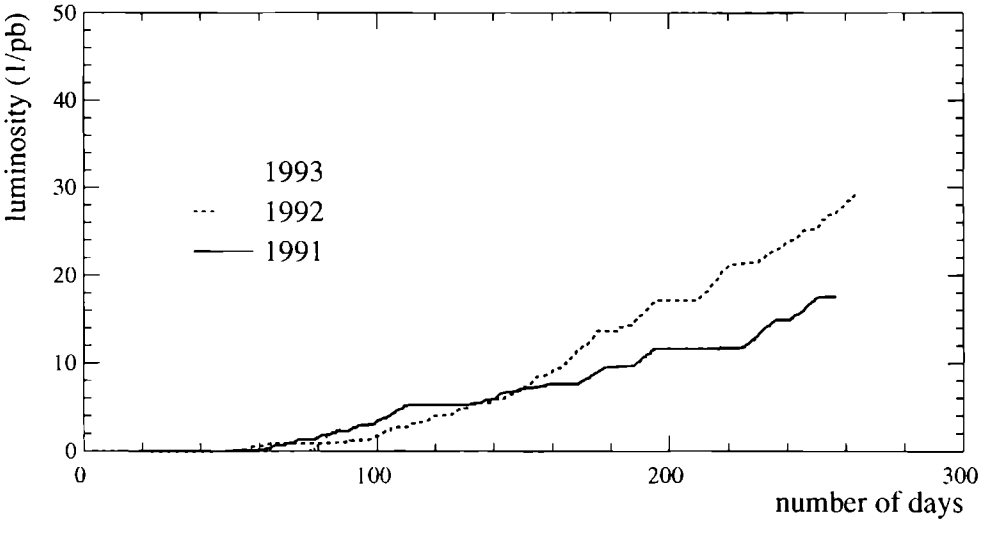

Figure 2.2: *The integrated luminosity at the L3 intersection point, for the years 1991, 1992 and 1993*

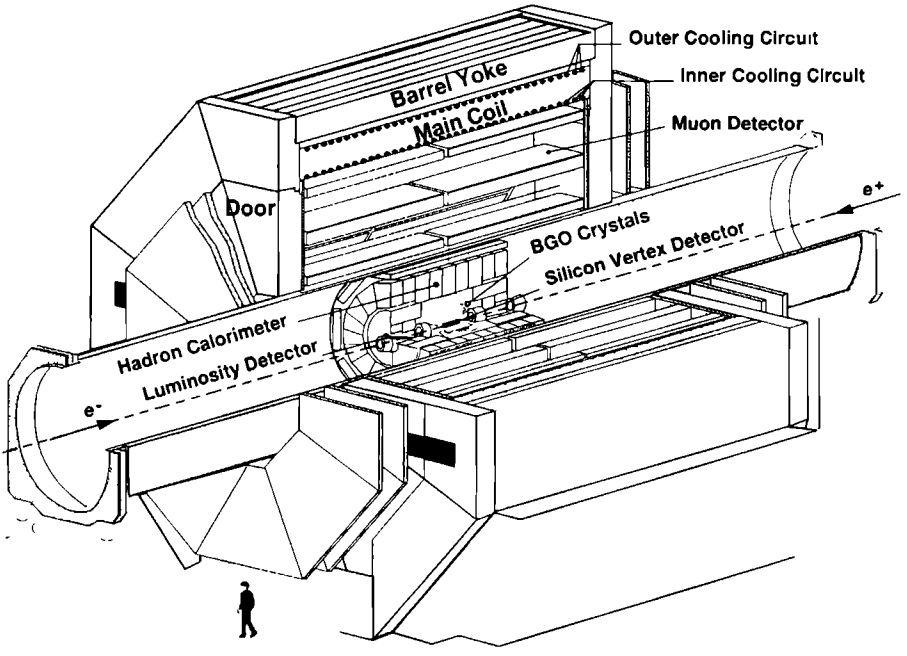

Figure 2.3: *A three dimensional view of the L3 detector.*

solenoid magnet with a central field of 0 5 Tesla In the three dimensional view of L3 (figure 2 3) the different detector parts can be distinguished

1 **The muon detector.**
The outermost detector consists of three layers of drift chambers, providing a high precision measurement of the muon momentum The muon barrel system measures the curvature of the tracks in the solenoid magnetic field During 1993 and 1994 additional muon chambers have been installed in the forward and backward regions measuring the muon tracks curved by a toroidal field in between these chambers

2 **The calorimeters.**
A calorimeter consisting of Bismuth Germanate (BGO) crystals is used to measure the en ergy and positions of the electrons (positrons) and photons In the polar direction the crystals of this calorimeter (ECAL) point to the interaction point In the azimuthal direction they are slightly tilted For the measurement of the hadronic particles a uranium calorimeter has been constructed (HCAL) It is a sampling calorimeter with uranium absorber plates inter spersed with proportional wire chambers Just outside the hadron calorimeter a muon filter is mounted consisting of brass absorber plates adding another interaction length of material before the muon chambers

Between the ECAL and the HCAL, plastic scintillating counters are located used for the triggering of hadronic events Cosmic rays can be rejected with the timing information of the scintillators

Both calorimeters are divided into a barrel part, positioned as a cylinder around the beam pipe, and two end caps located at the forward and backward region Both barrel and end caps can be seen in figure 2 4

3 **The inner detector.**
The inner detector consists of a tracking chamber based on the time expansion principle (TEC) and a silicon micro strip detector (SMD) These detectors are used in conjunction to determine the position of the vertex and the momentum of charged particles The SMD was installed in 1993 In figure 2 4 the inner detector is shown in somewhat more detail

2.4 The luminosity monitor

The original luminosity detector of L3 consisted of a BGO calorimeter Before the 1993 run this setup was upgraded with a silicon tracker, the SLUM The luminosity measurement using this tracker in combination with the BGO is the subject of this thesis Since the BGO detector is an essential part of the luminosity monitor as a whole, it is described here in more detail than the rest of L3 In figure 2 4 the position of the luminosity monitors can be seen In the enlarged view in figure 2 5, the relative positions of the BGO and the SLUM are shown A particle originating from the interaction point causes hits in the three layers of the SLUM and is stopped in the BGO crystals producing an electromagnetic shower

The BGO calorimeter consists of 304 BGO crystals on each side of the interaction point The location of the BGO is just in front of the low beta magnets of LEP The nominal position is 2 8

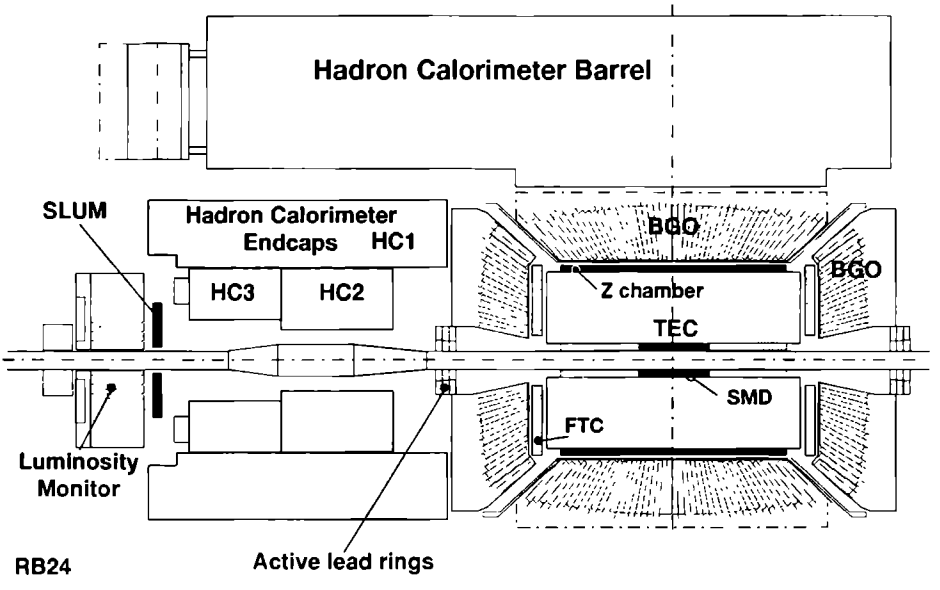

Figure 2.4: *The inner detector on the +z-side of the interaction point. The L3 detector is symmetric with respect to the interaction point. The conical beam pipe is only installed on the +z-side; it is straight on the −z-side.*

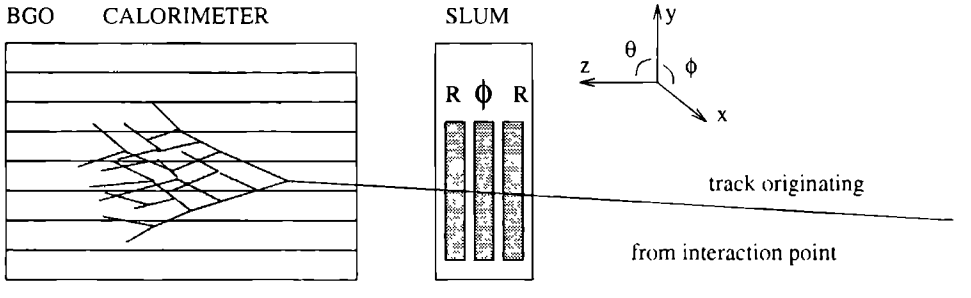

Figure 2.5: *Schematic drawing of the luminosity monitor. In the calorimeter eight layers of BGO crystals are shown. The silicon tracker (SLUM) consists of three layers, two r-measuring layers and one ϕ-measuring layer.*

meters from the interaction point (in the z direction) The exact position changes from year to year as the luminosity detectors are removed in each winter shut down The exact position after installation is obtained through optical measurements by the LEP survey group [17] These measurements are repeated several times per year The overall accuracy obtained on the detector position by the survey group is 300 μm

The BGO crystals (24 radiation lengths long) have an excellent energy resolution [18] but they are sensitive to radiation damage [19] The crystals are stacked in eight rings, concentric around the beam axis Azimuthally they are grouped in 16 sectors containing 19 crystals each The front view of the BGO can be seen in figure 2 6 In this figure the black rectangles represent the energy deposited as seen when a Bhabha scattering event is recorded The crystals cover a radius of 68 mm on the inside to 192 mm on the outside of the detector

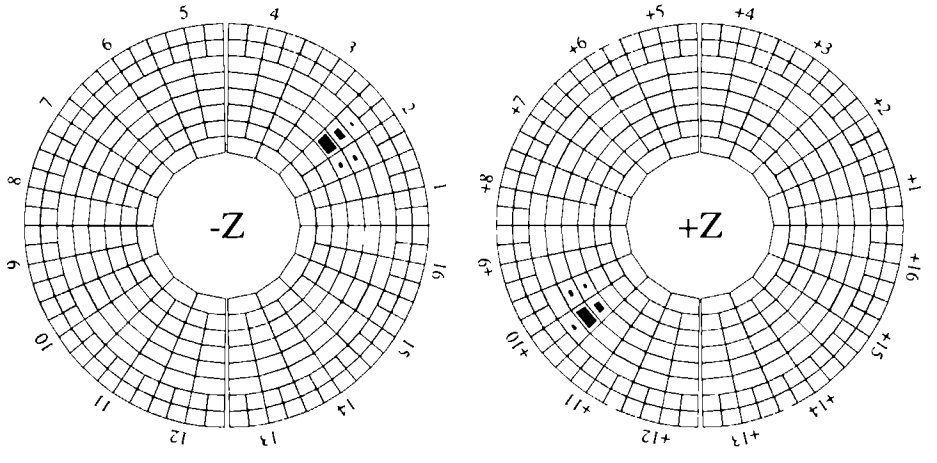

Figure 2.6: *The BGO calorimeter seen from the interaction point on both sides (−z and +z) The black rectangles represent energy deposits*

The BGO detector consists of two halves, split in the x-z plane When LEP is being filled, or when the beams are tuned, the BGO detector can be retracted to reduce the chance of radiation damage in case of beam loss To enable the retraction, the detector is divided in two halves, the split being in the x-z plane The BGO is read out with photo diodes On the backside of each crystal a photo-diode is glued Close to the detector the analogue signals of the diodes are digitised To calibrate and monitor the crystals they are flashed with a light emitting diode, mounted on the front side of each crystal Especially in the case of beam accidents the light emission of the crystal can degrade substantially However, the crystals do recover from this damage A detailed description of this effect and of the readout of the BGO can be found in [20]

During the LEP runs from 1989 until 1992 the BGO detector provided a luminosity determination with an uncertainty of 0 5% In addition it was used as a reliable online radiation monitor for radiation levels at LEP

Chapter 3

Silicon strip detectors

3.1 Introduction

Although in nuclear physics silicon detectors appeared in the early fifties, they were not used in high energy physics experiments until 1970 [21]. The ongoing development of techniques allowing application of fine surface structures on large area sensors [22, 23] stimulated their use in high energy physics. Silicon micro-strip sensors are nowadays often used as vertex detectors in collider experiments, reaching position resolutions in the order of 10 micron [24]. In the first part of this chapter the general characteristics of silicon detectors are given.

In future collider experiments silicon strip detectors will play a significant role. One of the main concerns for these applications is the deterioration of the sensors due to radiation damage. The leakage current running through a detector is an important indication of the damage induced. To monitor the status of the L3 luminosity tracker the leakage current is measured daily. This monitoring is especially important in the case of beam accidents. In the second part of this chapter the outcome of these measurements is presented. The exact nature of the observed currents is studied in a dedicated test setup.

Although most of the theory in the following sections is valid for all semiconductor materials, only the use of silicon is specifically discussed.

3.2 Measurement of high energy particles in silicon

3.2.1 Principle of detection

An important property of a semiconductor detector is its high detection efficiency. The energy needed to create one information carrier (in this case an electron-hole pair) is low and the density of the solid state material is high. This means that a short path length of a particle traversing the detector already provides a large signal. As the energy resolution is dominated by the statistical fluctuations in the number of information carriers created, the resolution compares favourably with a gas filled detector.

An additional advantage of a semiconductor detector is its fast response. The time needed to collect the charge created by an incoming particle is in the order of ten nanoseconds. The time

involved in the production of the information carriers is only a few picoseconds and can be neglected

The energy levels of the electrons in a semiconductor can be represented by a band structure, consisting of a conduction band and a valence band An electron in the valence band is fixed to its place in the crystal An electron in the conduction band is free to drift through the crystal The valence band and the conduction band are separated by an energy gap, which for silicon is 1 115 eV (at 300 K) If an electron gains enough energy to overcome this gap, both the electron and the hole that it has left in the crystal, contribute to conductivity In silicon the energy of such an electron hole pair is 3 6 eV [25] This energy is much higher than the energy gap because part of the energy lost by the traversing particle is absorbed by the crystal [26] The numerical values of the important silicon properties are shown in table 3 1

atomic number	14
atomic weight	28 09
density (g/cm^{-3})	2 33
dielectric constant	12
energy gap (eV)	1 115
carrier density (cm ^{3})	1 5 10^{10}
resistivity (Ω cm)	2 10^{5}
electron mobility (cm^2/Vs)	1350
hole mobility (cm^2/Vs)	480
energy electron hole pair (eV)	3 6
radiation length (cm)	8 9

Table 3.1: *Properties of silicon at 300 K Due to the presence of impurities the resistivity is in practice usually much lower The relatively large energy gap allows operation of silicon at room temperature*

The process by which incident radiation deposits energy in the crystal depends on the type of particle and on its velocity and energy The number of generated electron hole pairs equals the deposited energy (in eV) divided by 3 6 The energy deposition of high energy electrons and photons is treated in the next section

3.2.2 Charged particles

The energy loss due to ionisation of a charged particle traversing a thin layer is given by the well known Bethe-Bloch [27] equation

$$-\frac{1}{\rho}\frac{dE}{dx} = 4\pi N_A m_e r_e^2 z^2 \frac{Z}{A}\frac{1}{\beta^2}\left[\ln\left(\frac{2m_e\beta^2}{I(1-\beta^2)}\right) - \beta^2 - \frac{\delta}{2}\right] \qquad (3\,1)$$

where N_A is the Avogadro number r_e is the classical radius of the electron Z and A are the atomic number and mass (in g/mol), m_e is the electron rest mass (in MeV) I is the average ionisation potential (172 eV for silicon), ρ is the density, $\beta = v/c$ and δ is the screening effect (see below)

From equation 3 1 it can be derived that the energy loss reaches a minimum around $\beta\gamma = 4$ with $\gamma^{-1} = \sqrt{1-\beta^2}$ For relativistic particles the energy loss increases logarithmic with their energy This can be understood by the fact that the transverse field of the particle increases, the particle sees' more atomic electrons The original Bethe Bloch equation does not take into account the screening effect, at a certain energy the particle can not interact with even more electrons because they are screened off by the surrounding nearby electrons

The Bethe Bloch equation was derived under the assumption that the mass of the incoming particle is much higher than the mass of the electron obviously an invalid assumption for an electron The main difference in the derivation of the Bethe Bloch equation for an electron is the maximum energy transfer in a collision, E_{max} The difference in F_{max} for electrons and for particles with a mass larger than the electron mass is

$$\begin{aligned} (M >> m_e) \quad E_{max} &= \gamma^2 2 m_e \beta^2 \\ (M - m_e) \quad E_{max} &= \frac{\gamma^2 m_e \beta^2}{1+\gamma} \end{aligned} \tag{3 2}$$

The correct equation for an electron including the screening effect can be found in [28] its results though is numerically not very different from equation 3 1

The screening effect, for particles with $\beta\gamma$ larger than 10^3, traversing a silicon layer is given by [25, 29]

$$\delta = 4\,6 \log \beta\gamma - 4\,38 \tag{3 3}$$

The screening effect causes the flattening of the energy loss for ultra relativistic particles At this plateau the energy loss is not very sensitive to the type of the incident particle nor to its energy Particles at this plateau (Fermi plateau) are often referred to as minimum ionising particles (MIP s) although strictly spoken this is only valid for particles with $\beta\gamma = 4$

The mean energy loss in a 300 μm silicon layer is shown in figure 3 1 (left), for protons, muons and electrons as a function of their momentum From this plot it can be seen that the energy loss of a MIP is around 90 keV The energy loss of a 45 GeV particle is slightly higher (120 keV) In the same figure (right) a plot of the fluctuations of the energy deposit from a 45 GeV electron is shown The fluctuations in energy loss in a thin layer follow to a good approximation a Landau distribution

For completeness the energy loss due to Bremsstrahlung is also mentioned In this process an electron slows' down in the field of a nucleus in the material, losing energy by radiating a photon A useful quantity in the evaluation of this process is the radiation length X_0 It is defined as the distance at which the initial particle loses a factor $1/e$ of its energy For thin layers the process of Bremsstrahlung is negligible

3.2.3 Photons

Photon interactions in detectors are generally distinguished from charged particle interactions because they do not gradually lose their energy Due to the discrete character of their interactions the absorption of photons is rather described in terms of an incident beam which is absorbed by a medium After traversing a layer of thickness t, a photon beam of original intensity I_0, has an intensity I equal to

$$I = I_0 \exp\left[\frac{-t\rho}{\lambda}\right] \tag{3 4}$$

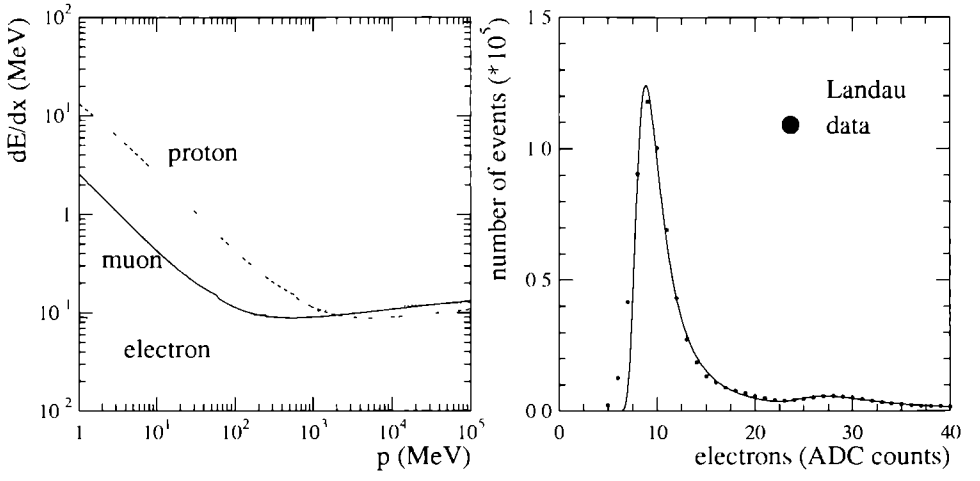

Figure 3.1: *The energy deposition in 300 μm silicon On the left the energy loss by ionisation as a function of momentum. On the right the measured fluctuations in the energy loss of a 45 GeV electron in the L3 silicon luminosity tracker (one ADC count corresponding to 0.01 MeV). The small enhancement around 28 ADC counts is due to multiple particles passing through one strip.*

where λ is the mean free path of the photon (or attenuation length) expressed in $cm^2\ g^{-1}$ and ρ is the density of the material.

Three processes contribute to the cross section of photon interactions in material. For low energy photons (below 100 keV) the cross section is dominated by photo electric absorption; excitation or ionisation of an atom. In the energy range from 100 keV to 10 MeV, Compton scattering dominates the interaction. Compton scattering is defined as the scattering of a photon on an atomic electron. Finally, for a high energy photon (above 10 MeV) the main contribution to the total cross section is pair production. In pair production a photon converts to an electron and a positron. The average distance a photon travels before it creates the e^+e^- pair is X_γ. It differs from the radiation length, X_0, by a factor 9/7 [30]. As a result the probability of detection of a high energy photon in a 300 μm thick silicon layer is small. Substitution of X_γ for the attenuation length in equation 3.4, reveals that less than one percent of the photons is converted in an electron positron pair. If photon conversion occurs (for example in the material in front of the detector) both the electron and the positron will behave as minimum ionising particles.

3.3 Silicon detector characteristics

3.3.1 General properties

The transition of the electron from the valence band to the conduction band can be caused by absorption of energy deposited by a traversing particle or by thermal effects. The number of charge

carriers in intrinsic (high purity) material, n_i, is strongly dependent of the temperature:

$$n_i \propto \exp\left[\frac{-E_g}{2kT}\right] \tag{3.5}$$

where T is the temperature, E_g the energy gap and k the Boltzmann constant.

In an ideal intrinsic semiconductor the number of conduction electrons matches exactly the number of holes in the crystal. In practice it turns out that even in very high purity material there is a small amount of impurities. A material in which the donor (e.g. a five valence atom) impurities dominate is n-type material, if there are more acceptor (e.g. a three valence atom) impurities it is p-type material. In practice impurities are intentionally added to manipulate the properties of semiconductor materials.

In most detectors currently in use, the bulk material of the sensors is n-type. To decrease the current through the detector a rectifying pn-junction is applied. A small layer of extra doped p-type material (denoted as p^+) is applied on top of the bulk. From the p^+-type region there is a flow of holes to the n-type region, in the opposite direction there is a flow of electrons. The electrons that leave the n-type layer will immediately recombine with a hole on the p^+-side. In the p^+-type region there are now immobile donor impurities left which have absorbed electrons and therefore have a negative charge. As a result charge is being built up, reducing the free flow of holes and electrons. The resulting potential difference is called the built-in potential, V_{bi}. The most important quantities of the pn-junction are shown in figure 3.2.

An external voltage can be applied in the same direction of the built-in potential; this is called a reverse bias. As a result the size of the n-type region saturated with holes from the p^+-layer, the depletion layer, increases. If the bias voltage is increased until the thickness of the depletion layer equals the thickness of the silicon layer the sensors are fully depleted.

Below the limit of full depletion the thickness of the depletion layer is approximately given by

$$d \cong [2\varepsilon V \mu \rho]^{\frac{1}{2}} \tag{3.6}$$

where ε is the dielectric constant, μ is the mobility of the majority carriers in the bulk material, V is the applied reverse bias voltage (plus the built-in voltage which is usually negligible) and ρ is the resistivity of the semiconductor.

An additional advantage of applying an external voltage is the decrease of the collection time of electron hole pairs. To enhance the speed of the charge collection a detector can be operated at a voltage higher than the depletion voltage (overbias). In the luminosity tracker the sensors are operated at a bias voltage which ensures full depletion, so no substantial overbias.

From equation 3.6 and the values given in table 3.1 the average depletion voltage of the sensors is calculated to be 40 to 50 V. In practice it can be determined by measuring the capacitance as a function of the applied external voltage difference. When the sensor is fully depleted the capacitance reaches a minimum.

Using equation 3.6, the capacitance per unit area, A, of the detector can be expressed as

$$C = \frac{\varepsilon A}{d} \cong \left[\frac{\varepsilon}{2V\rho\mu}\right]^{\frac{1}{2}} A \tag{3.7}$$

The calculated capacitance of a typical strip of the luminosity tracker (see the next section for a detailed description of the sensor geometry) is 10 pF at full depletion. A schematic view of the construction of a DC-coupled silicon strip detector is shown in figure 3.3.

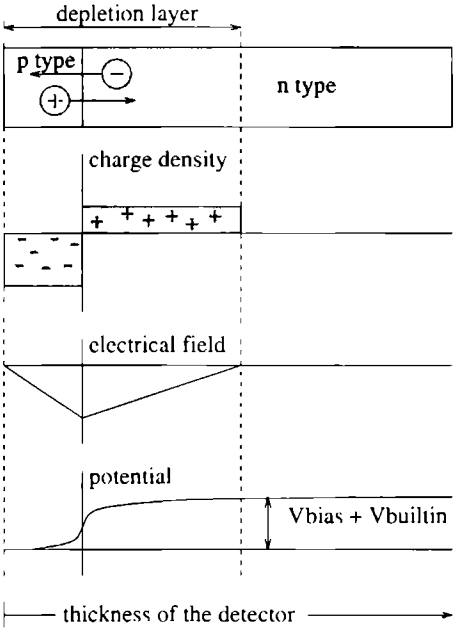

Figure 3.2: *A sketch of an abrupt pn-junction, showing the charge built up and the resulting field and potential across the junction.*

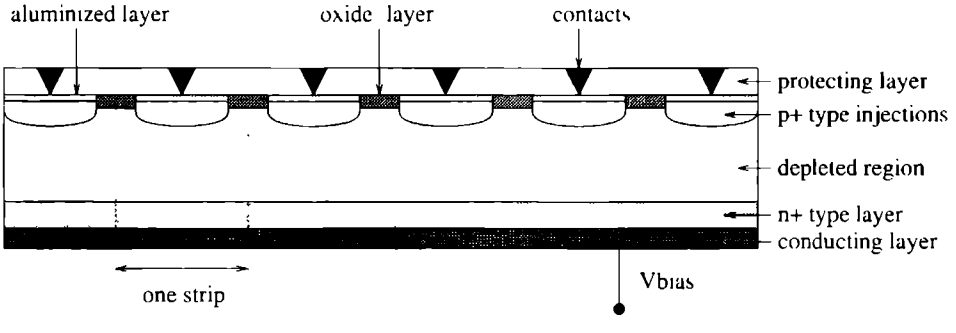

Figure 3.3: *Cross section of a silicon strip detector, perpendicular to the strip direction.*

3.3.2 Sensors used in the luminosity detector

The design of the sensors in the luminosity detector is based on the use of silicon wafers with a precise strip geometry The detector is designed such that the charge created by a traversing electron is predominantly collected on one strip The region between two strips in which the created electron hole pairs are distributed to both strips, is in the order of a few microns

Two different sensor types are used, one with strips in the ϕ and one with strips in the r direction Both types have the same size and cover an angle of 24 degrees in ϕ In r they cover the region from r = 76 mm to r = 154 mm The sensors are shown in figure 3 4 and are referred to as ϕ-sensor and r-sensor The ϕ sensor consists of 64 strips with a pitch of 0 375 degrees On the r sensor three different regions can be distinguished The first region consists of 64 strips with a pitch of 0 500 mm The second and third region have 16 strips each with pitches of 1 875 and 1 000 mm respectively The distribution of these different pitch regions is optimised for the luminosity measurement, keeping the number of readout channels to a minimum

Around the strips at the border of the silicon wafer there is one additional strip, the guard ring The guard ring, with a width of 100 µm, is used to shape the electric field near the ends of the strips, as well as near the outside strips, and thus it provides a uniform behaviour of all strips [31, 32] Its total area is comparable with the area of an average strip

On the boundaries of each sensor five survey marks are imprinted to enable metrology measurements after assembly of the detector The survey marks can be seen as black dots in figure 3 4

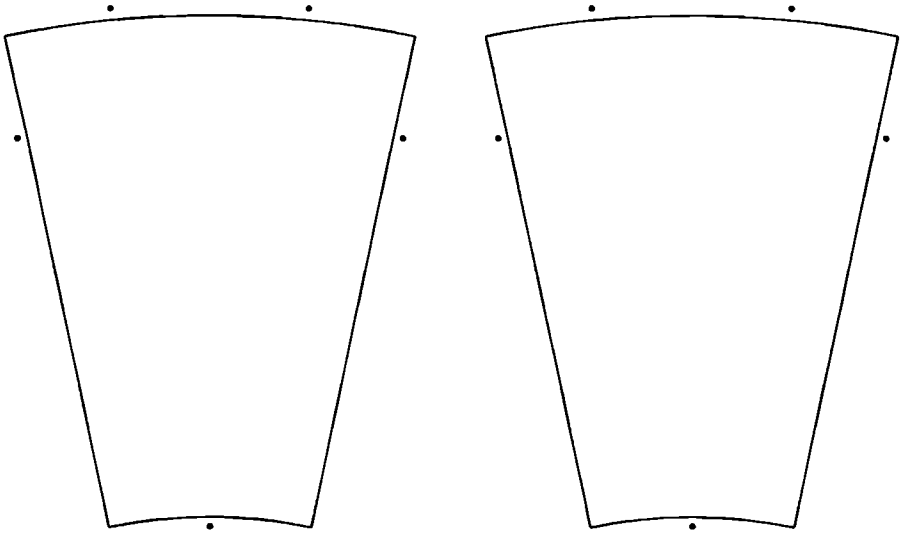

Figure 3.4: *The ϕ-sensor (left) and the r-sensor (right) On the r sensor the three different pitch regions can be distinguished The black dots on the edges of the sensors are the survey marks The thick black line indicates the location of the guard ring*

To protect the sensors from dust and moisture the surface is coated with a protection layer (or passivation layer) Most sensors are covered with silox (SiO_2) but 10 percent have a polyimide passivation layer Due to the relative new procedure at the time of production there were some difficulties in meeting the specifications for the sensors with the polyimide layer

The relevant specifications for the sensors are shown in table 3 2

	value	tolerance
resistivity (kΩcm)	7	> 5
inter strip resistance (MΩ)		> 1
wafer thickness (μm)	300	± 20
depletion voltage (V)	30	< 50
operation voltage (V)	50	
breakdown voltage (V)		> 100
leakage current strip (nA)	1	< 20
leakage current sensor (nA)	300	< 1000

Table 3.2: *Specifications for the production of the silicon sensors used for the L3 luminosity tracker at an operation voltage of 50 V and a temperature of 20 °C The quoted values are the expected averages the tolerances represent the maximal deviations from these specifications*

3.4 Leakage current

In spite of the application of a rectifying junction a small current through the detector usually remains It is generally referred to as reverse current or leakage current Measurements of the reverse current in a sensor can reveal imperfections in the crystal structure or in the implanted strip structure Monitoring the long term behaviour of the leakage current can give an indication of the amount of radiation damage in a sensor The sources contributing to the leakage current are

1 **Generation current.**
Electron hole pairs are generated and drift towards the electrodes under influence of the applied field This current is proportional to the area of the strip and the thickness of the depletion layer It also increases with temperature This dependence is proportional to the increase in the number of intrinsic carriers n_i A rule of the thumb is that a temperature increase of 8 degrees causes a rise in the leakage current of a factor two (see equation 3 5 for the temperature dependence of n_i)

2 **Diffusion current.**
A usually small current, caused by generation of pairs outside the depletion region Some of the electrons (or holes) drift into the depleted area before recombination has occurred On the edges of the detector this can be a significant contribution to the leakage current due to the presence of a none depleted part of material The diffusion current is proportional to n_i^2 [33]

3 **Surface current.**
This current flows around the edges of the detector and through the protection layer on the surface This component is expected to be small after manufacturing of a sensor However, after assembling (gluing and bonding) the sensors can be damaged or become less clean and the surface current can become important

The surface current can be distinguished from the generation current because it does not depend on the thickness of the depletion layer Since the width of the depletion layer grows with the square root of the applied voltage (equation 3 7), the nature of the leakage current can be determined by studying the current as a function of the voltage In case of surface effects a deviation from the $\sqrt{V}$ dependence is observed Surface currents are influenced by surface contaminations and can be a function of time, temperature and humidity [25]

In most semiconductor detectors the leakage current is dominated by the generation current The allowed leakage current in a detector is determined by noise considerations and by the linearity of the readout electronics In chapter 4, where the readout system is described, this is explained in more detail

3.4.1 Test measurements

In case high currents run through the strips one should be concerned by non linear behaviour of the amplifiers At NIKHEF a testing device has been constructed which enables the study of the current in each strip and the guard ring separately One ϕ-sensor is investigated which has not been mounted for operation in the real detector The sensor is not affected by the gluing and bonding processes and the contribution of the surface current is therefore expected to be small The actual measurement is performed by positioning an aluminium needle on a strip (probing) For this purpose a small cut away is made in the protection layer at the time of manufacturing A probe card with 64 equally spaced, adjacent needles allows to probe all channels in one operation Series of measurements can be performed without the need to access the test device, of which a schematic overview is given in figure 3 5

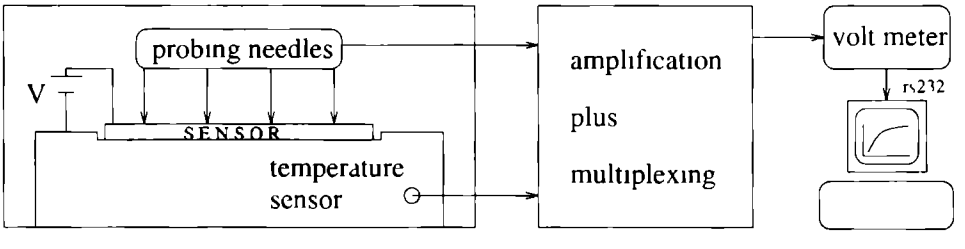

Figure 3.5: *The experimental arrangement used for the measurements of the leakage current in the silicon wafers Note that in reality there are 64 probing needles*

The currents through the strips are measured sequentially All strips (except for the one being measured) are grounded At each measurement the sensor is operated at 50 V and thus fully depleted (unless specifically mentioned otherwise) The temperature is registered at the start of each measuring sequence The time between two sequences can be varied

Temperature dependence

To interpret the measurements the effects of the change in temperature have to be unfolded Special measurements are performed during which the sensor is heated artificially The large temperature differences invoked this way (large compared with day to day changes) allow a precise determination of the temperature dependence Separating the generation current, I_{gen} (proportional to n_i), and the diffusion current I_{diff} (proportional to n_i^2), combined with equation 3 5 the overall temperature dependence can be fitted with the following expression

$$I_{leak} = A \exp\left[\frac{-E_g}{2kT}\right] + B \exp\left[\frac{-E_g}{kT}\right] + C \qquad (3\,8)$$

where T is the temperature, E_g the energy gap and k the Boltzmann constant The first term represents the generation current, the second term the diffusion current The constant C, is introduced to account for offsets in the readout system and an eventual surface current

In figure 3 6 the rise of the dark current as a result of the temperature increase is shown (left) This current is fitted using equation 3 8 In the right plot the current as a function of time is shown, after it has been corrected for temperature changes The numerical values of the resulting fit are given in table 3 3 together with the different current contributions (normalised to a reference temperature of 20°C)

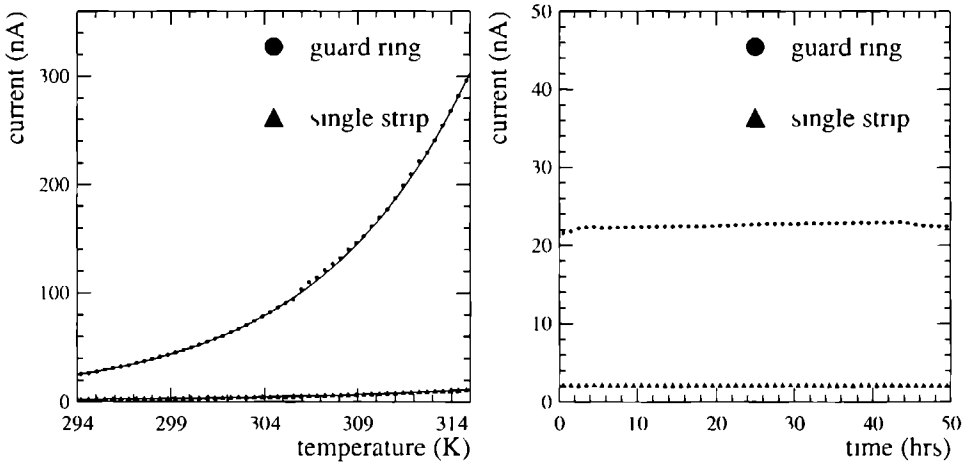

Figure 3.6: *The current as a function of temperature (left) The currents in the guard ring and in a single strip are separately fitted On the right plot the current as a function of time normalised to 20°C*

The fit results show that the component of the diffusion current in an average strip is indeed low as was expected However, in the guard ring it is substantial The generation current in the guard ring is five times higher than the generation current in a strip, whereas the area of the guard ring is comparable to the area of one strip An explanation for this enhancement is the extension of the depletion zone outside the actual area of the guard ring Since the bias voltage extends over the complete backside of the sensor the resulting electric field can spread outside the area of the

	single strip	guard ring
A	$6.9 \cdot 10^{9}$	$4.1 \cdot 10^{10}$
B	$2.9 \cdot 10^{18}$	$2.1 \cdot 10^{20}$
C	0.8	0.3
current at 20°C in nA		
I_{gen}	1.6	8.1
I_{dif}	0.2	11

Table 3.3: *Results of the fit for the temperature dependence. The overall error on the current measurement is about 0.2 nA*

guard ring, which is only 100 µm on the (top) surface of the sensors. The effective area of the guard ring is therefore larger.

Using the results of these measurements all the following measurements are normalised to a temperature of 20°C.

Reproducibility

In a reproducibility test a sensor is kept at 50 V bias voltage and the leakage current is measured during one week. The observed rise in the dark current can be attributed to an increase of the current through the guard ring as can be seen in figure 3.7. If the bias voltage is switched off for the same period the current decreases to its original value. After one week the same measurement is repeated. The second measurement shows the same increase in the current through the guard ring.

The key parameters in the behaviour of the surface current are not well understood. Therefore, the value of the time constant involved in the increasing current can not be explained. The effect could be influenced by different degrees of humidity. The assumption that the observed rise is established by an increasing current in the guard ring is however justified. The performance of the strips is therefore not affected.

Current versus bias voltage

To determine the nature of the current (especially for the guard ring), the behaviour of the current as a function of the applied bias voltage is studied. The voltage is increased from 1 to 100 V thus going from a small depletion layer to a fully depleted, overbiased sensor.

The measured current-voltage curve, shown in figure 3.8, is fitted with the following functional form.

$$I_{leak} = A \cdot V^{1/2} + B \cdot V + C \tag{3.9}$$

The first term represents the generation current. Since this current is proportional to the volume of the depletion layer, it is proportional to the square root of the bias voltage (see equation 3.6). When full depletion is obtained (in this case at 10 V) the first term in the equation is kept constant. The second term is introduced to describe the surface current, I_{surf}. The assumption is made that the surface current behaves as a current through an ohmic resistor. The constant is again added to absorb offsets in the measurements.

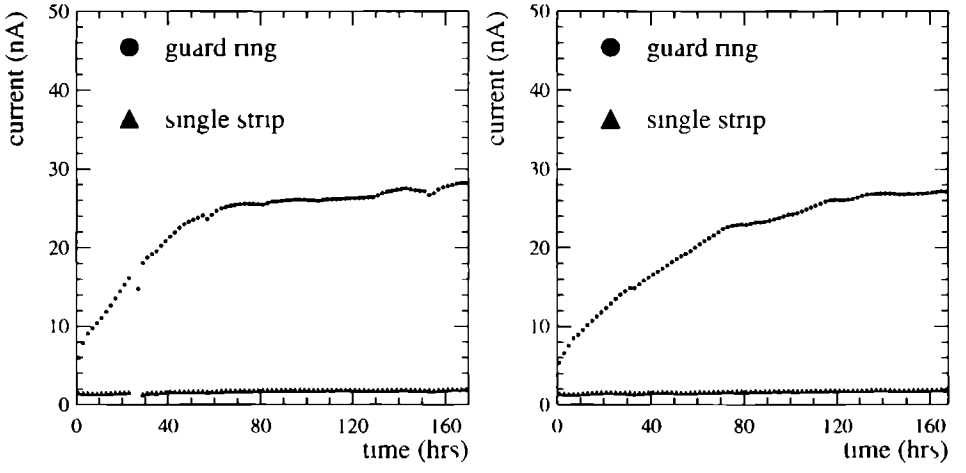

Figure 3.7: *The current as a function of time during one week at a bias voltage of 50 V (left) After the sensor has been without bias voltage for one week the measurement is redone (right)*

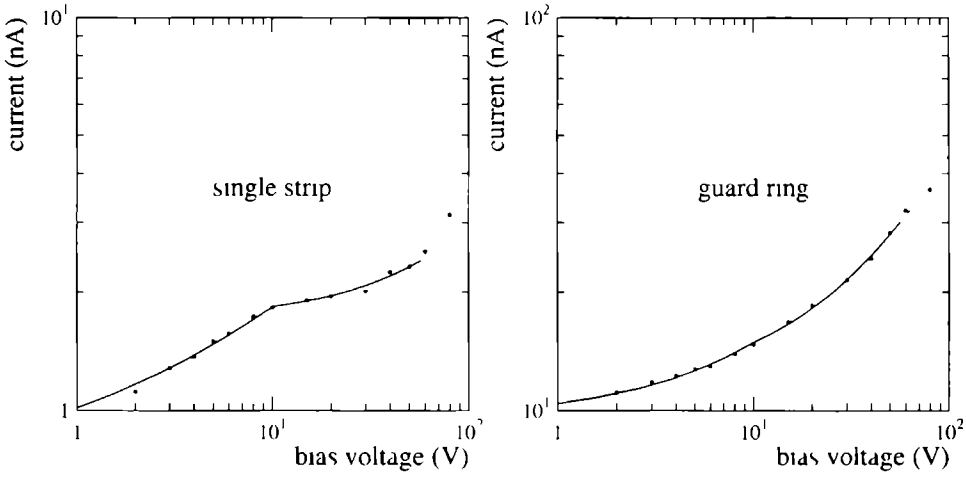

Figure 3.8: *The reverse current as a function of the applied bias voltage, in a typical strip (left) and in the guard ring (right)*

	single strip	guard ring
A	0 33	0 73
B	0 01	0 33
C	0 68	9 4
current at 50 V in nA		
I_{gen}	1 0	2 3
I_{surf}	0 5	16 5

Table 3.4: *Results of the fit for the voltage dependence The overall error on the current measurement is 0 2 nA*

From results of the fit, shown in table 3 4, it can be concluded that the surface component in an average strip is negligible, whereas it is dominant in the guard ring It explains why the current in the guard ring behaves so differently from the current in the rest of the sensor

When care is taken in keeping the sensors at full depletion the performance of the detector will not be affected by the observed increasing current However, it is useful to measure the leakage current of a DC coupled detector in two separate circuits, one for the guard ring, one for the strips

3.4.2 Long term behaviour at LEP

During operation in 1993 and 1994 the total leakage current has been monitored for all silicon sensors The current running through the individual strips and through the guard ring is not separately measured Since a large resistor (1 MΩ) is used in series with the detector in the bias voltage circuitry, monitoring the total current is essential A current surpassing several μA causes a significant voltage drop, which in turn can lead to a decrease in the thickness of the depletion layer

In figure 3 9 the long term behaviour of the sensors is shown Although a diversity exists in the behaviour of different sensors, a general observation is the rise in the dark current over long periods The increase is consistent with the measurements on the isolated sensors, although the current seems to rise over longer periods

A somewhat different behaviour is observed between sensors with a passivation layer of polyimide and silox The sensors with a silox coating show a slow rise in the current over a period of several weeks The polyimide passivated sensors show stable currents At the time the sensors were produced the polyimide passivation was a new procedure Problems during manufacturing led to sensors with initial high leakage currents Therefore it is at this point not possible to conclude which type of passivation is better in the long run

In 1993 the bias voltage of one sensor had to be increased to ensure full depletion Since the measurements described in the previous section showed that the main part of the leakage current is absorbed by the guard ring the behaviour of the detector strips is not affected

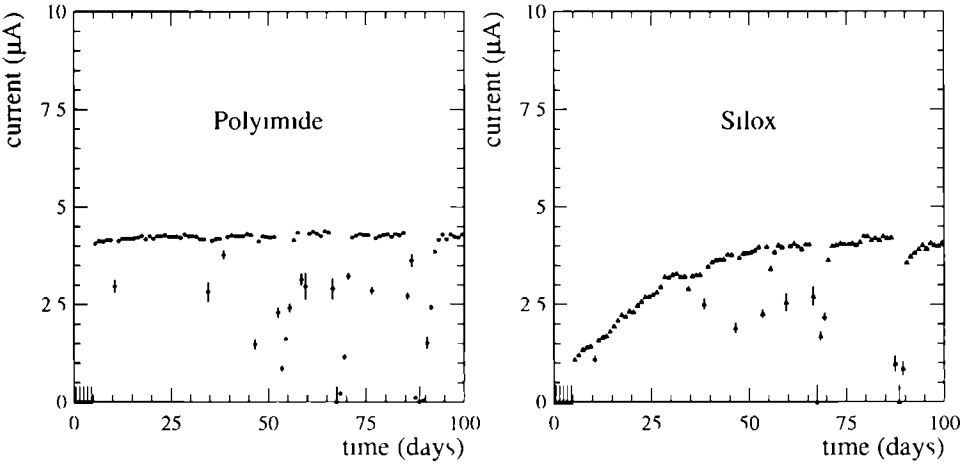

Figure 3.9: *The results from monitoring the long term dark current behaviour The first 100 days of the 1994 running period are shown The left plot represents the current in a typical sensor with a polyimide passivation layer the right plot the current in a silox coated sensor*

Chapter 4

The Silicon Luminosity Tracker

4.1 Introduction

Until 1993 the luminosity in the L3 experiment was determined with the sole use of a calorimeter consisting of BGO crystals. Bhabha events were selected by making requirements based on the energy deposited in the crystals and the reconstructed impact points. The accuracy of the final calculated luminosity using the BGO is mainly limited by the uncertainty in the knowledge of the crystal locations. The total systematic experimental error on the luminosity measurement using only the BGO is 0.5% [34].

In particular the uncertainty on the position of the inner boundary of the acceptance volume is very important. As the differential cross section for small angle Bhabha scattering behaves like $d\sigma/d\theta \propto 1/\theta^3$ a small error in the θ measurement translates in a relatively large luminosity variation.

For the 1993 run a silicon tracker has been developed aiming at a significant reduction of the experimental systematic error on the luminosity measurement from 0.5% to 0.2%. The main improvement is to be expected from a better definition of the fiducial volume. The tracker is always used in conjunction with the calorimeter since the latter still provides the trigger and the energy measurement, essential in the identification of Bhabha events. Hereafter the luminosity detectors are referred to as BGO (for the calorimeter) and the SLUM (for the silicon tracker).

4.2 Mechanical construction

In front of the BGO luminosity monitor a silicon detector is placed with strips perpendicular to the beam axis (measuring the ϕ-angle) and strips concentric around the beam axis (measuring θ-angle). Although silicon is in principle sensitive to radiation damage the detector is not retracted at injection time. The mechanical stiffness is therefore not affected. The location of the SLUM is measured by the LEP survey group together with the BGO. The overall precision on the geometry of the SLUM after its assembly is designed to be better than 50 micron.

The overall view of the detector is shown in figure 4.1. The silicon setup consists of two identical detectors, positioned at the $-z$ and $+z$ side of the interaction point. The silicon is protected with a 1 mm thick, brass cover providing electric shielding and light tightness as well.

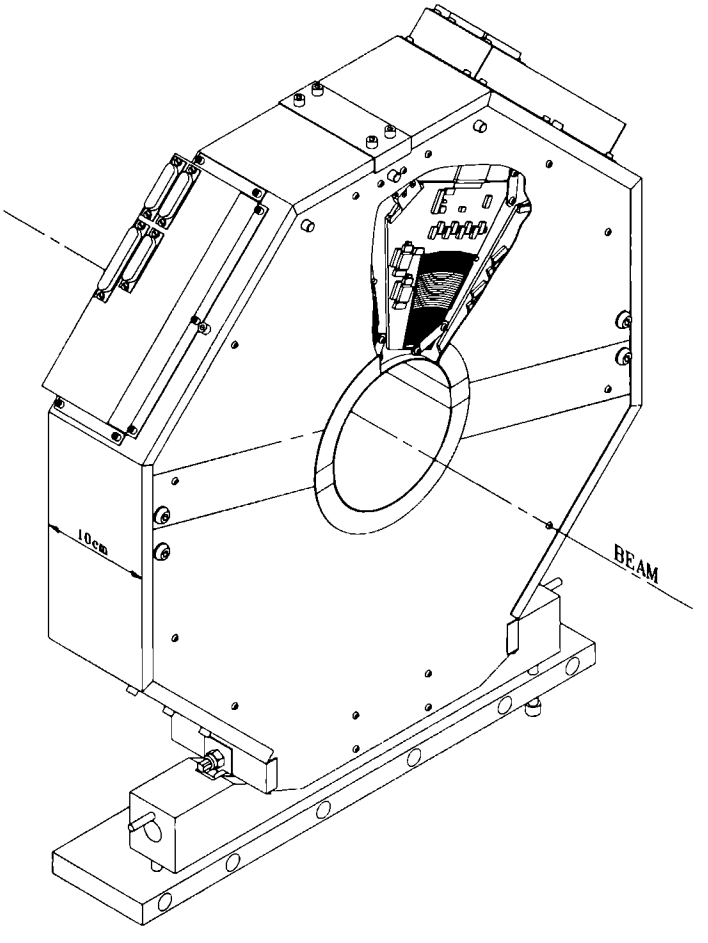

Figure 4.1: *A three dimensional view of the detector with details of the r measuring layer*

4.2.1 Sensor geometry

Although the layout of the sensors has been discussed already in the previous chapter some of their mechanical properties are recalled here for the sake of continuity

The accurate definition of the fiducial volume in the event selection is obtained through the sharp boundary which separates two strips and the accurate knowledge of the detector geometry Two sensor types are used which have the same size and cover an angle of 24 degrees in ϕ In r they cover the region from $r = 76$ mm to $r = 154$ mm The sensors as shown in figure 3 4 are referred to as ϕ sensor and r sensor The ϕ sensor consists of 64 strips with a pitch of 0 375 degrees On the r sensor three different regions can be distinguished The first region consists of 64 strips with a pitch of 0 500 mm The second and third region have 16 strips each with a pitch of 1 875 and 1 000 mm respectively The distribution of the different pitch regions is such that the inner boundary of the fiducial volume is located in the fine pitch region The outer boundary is located in the intermediate sized pitch region A limited number of strips (cost reduction[1]) provides optimal performance since the position of particles traversing the detector well inside the fiducial volume is not so important

Alignment

On the boundaries of each sensor five survey marks are printed to enable metrology measurements after assembly of the detector With these measurements the knowledge of the detector geometry is improved The silicon sensors are glued on printed circuit boards incorporating the first level of the signal processing Part of this board is milled away to ensure that the surface of the silicon is at the same level as the surface of the printed circuit board The alignment of such a module with respect to the support structure is obtained by placing the well defined edge of the silicon sensor area directly against alignment pins These stainless steel pins are glued into brass inserts Each sensor is aligned with the help of three pins Figure 4 2 shows how the sensor is mounted to the printed circuit board and to the alignment pins

To allow the installation of the SLUM around the beam pipe the detector can be divided in two parts These parts are attached with two large dowel pins for each layer The reproducibility of the assembly procedure is measured to be 3 μm

The original design aimed at a geometry knowledge of the two detector halves of 30 μm, reproducible after each assembly To confirm the accuracy of the positions of the sensors on the support structure, optical measurements were foreseen From these measurements it can be concluded that the geometry deviations with respect to the design values are within the specifications or even better After assembly the average deviation from the design value of the inner boundary is 20 μm as is shown in table 4 1 The uncertainty in the *known* position is, however, even smaller After full assembly and metrology the positions of the silicon sensors are known with a precision of 4 μm, obtained as the quadratic sum of the uncertainty of the detector assembly (3 μm) and of the optical survey bench precision (3 μm)

The mechanical stability of the detector was again tested after the 1993 run period The detector was dismounted, transported and re measured The sensor locations were found to be within 4 μm equal to the locations measured prior to installation in L3 When this is interpreted as an independent uncertainty the total error on the inner boundary is 6 μm This is a worst case estimate

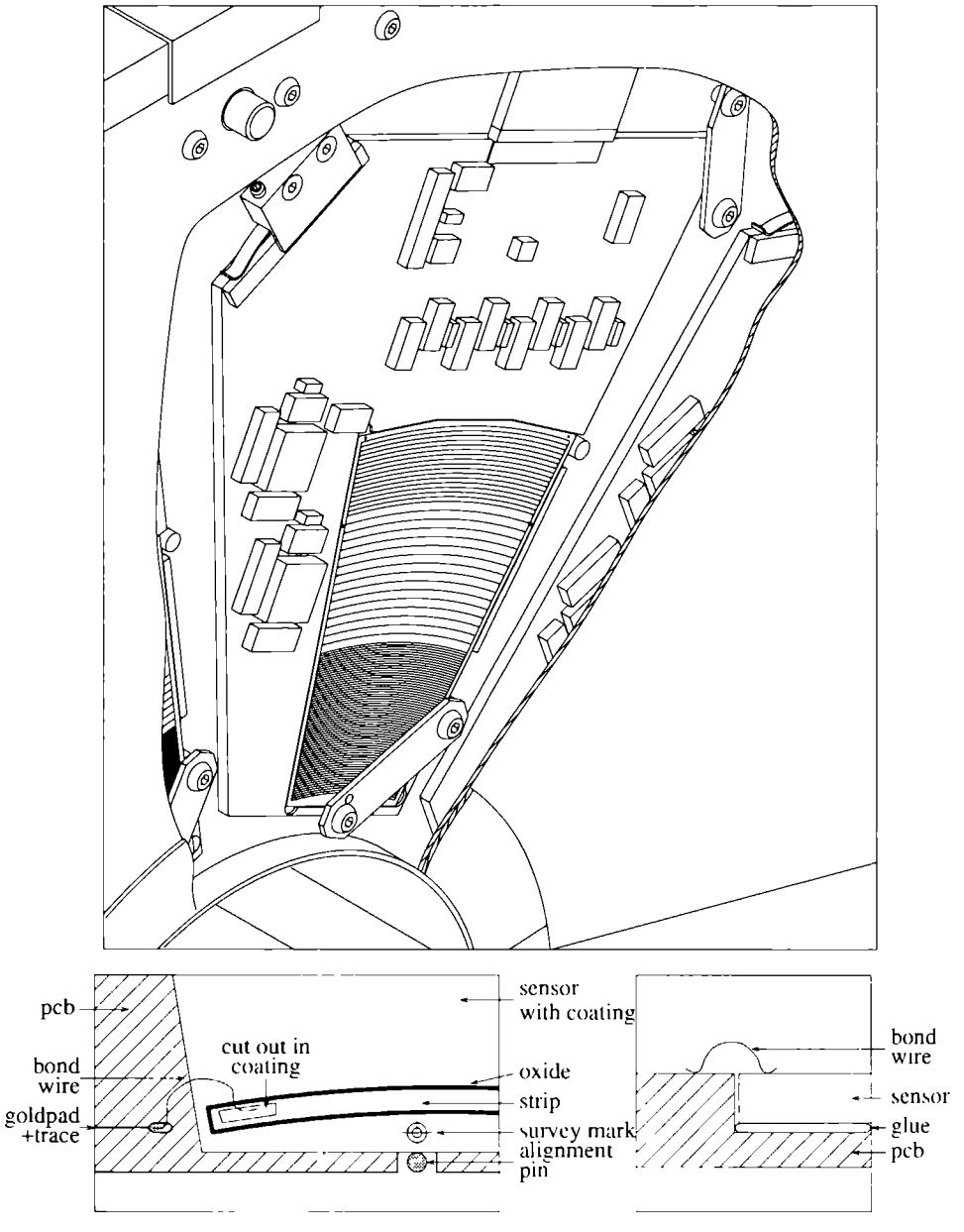

Figure 4.2: *The r-sensor mounted on the printed circuit board and two enlarged details. On the left the special notch in the border of the PCB, at the position of the alignment pin, is visible. On the right a side view showing the bond from a strip to the trace on the PCB.*

design r = 76 450	fitted radius (mm)	rms (μm)
− layer1 front	76 470	20 4
−z, layer1 back	76 475	28 7
−z layer2 front	76 464	30 8
z, layer2, back	76 497	36 3
+z layer1, front	76 481	18 9
+z layer1 back	76 474	36 1
+z, layer2, front	76 460	36 5
+z, layer2, back	76 465	28 5

Table 4.1: *The radius of the first strip boundary determined by fitting a circle to the measured positions The rms is the standard deviation of the positions of the individual sensors from the fitted radius*

4.2.2 Detector support

Each part of the SLUM (-z and +z) consists of three circularly shaped Stesalit layers, two r layers and one ϕ layer, holding 16 sensors each The location of the layers has been shown in figure 2 5

On the back and front side of each layer eight sensors are placed Since each sensor covers an azimuthal range of 24 degrees, two neighbouring sensors have a small overlap (1 5 degrees) The three support layers are rotated over an azimuthal angle of 7 5 degrees with respect to each other This rotation prevents that sensor boundaries notorious critical regions, are all in one line

A logic unit for readout purposes is a sector A combination of two r sensors and one ϕ sensor One sector consist of 256 strips Figure 4 3 shows the configuration of the sectors The complete silicon detector, consisting of 2x16 sectors contains 8192 strips to be read

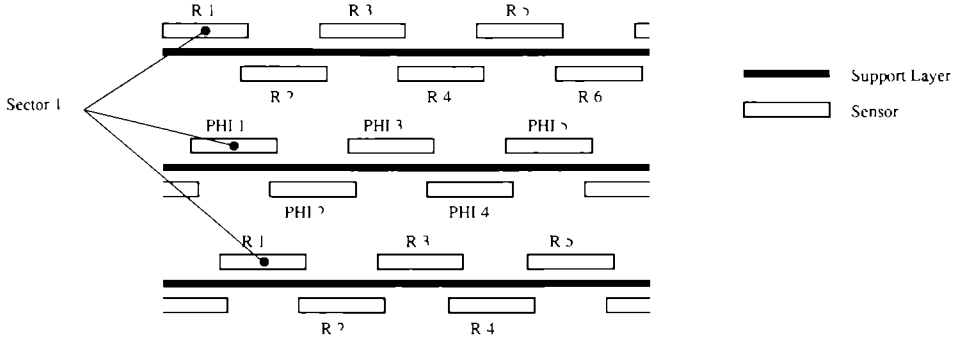

Figure 4.3: *The formation of sensors into sectors*

4.3 Data Acquisition

4.3.1 Layout

The data acquisition system (DAQ) of the silicon detector is designed such that the signals are only digitised after they are transported from the detector to the counting room, 120 meters away The digitisation is based on a flash analogue to digital converter almost identical to the one of the central tracking detector of L3 (the TEC [35]) A schematic overview of the DAQ system is shown in figure 4 4

A signal, generated by a traversing particle is preprocessed by the electronics located on the printed circuit board inside the detector This is the first level of the DAQ system and it is based on the use of an AMPLEX chip [36], with 16 input channels The ϕ sensor has 64 channels and is read with four chips, the r-sensor has 96 strips and is read with six chips

The silicon strips are directly coupled to the input of the chip using aluminium wire bonds from the strip to a golden pad on the printed circuit board The diameter of the aluminium wires is 30 μm The strength of the bonds is checked to be 8 ± 2 g

Two r sensors and one ϕ-sensor are read sequentially The analogue signal of the 256 channels of one sector is thus chained into a train of 256 pulses, representing the amplified output of the sector

The power system is located close to the detector Both detector sides have separate supplies The status of these supplies and the current they draw are continuously monitored The power for the first level electronics is plus and minus 5 V Inside the support tube this is fanned out and transmitted to all sectors The connections are all made on the ϕ board, subsequently the power is transmitted to the two r-sensors To protect the electronics against too large a voltage a fuse is included for each sector

The power needed to apply the bias voltage to the silicon sensors can be tuned for each sensor separately In case the leakage current increases above 5 μA the voltage drops since there is a large resistor in series with the backplane of the silicon Under normal conditions all sensors are operated at 50 V but the voltage can be raised to 100 V

The higher level of the readout system (called the FADC system) is located in the counting room The main task of the FADC system is to digitise the signals The logic modules controlling the synchronisation of the readout are integrated with the FADC system A key module is the carillon described in section 4 3 3 The carillon communicates with the L3 trigger and readout system and enables synchronous operation of the SLUM with the L3 data acquisition system

Finally the data are merged with the other L3 detectors on an event by event basis

4.3.2 The AMPLEX chip

The AMPLEX chip consists mainly of a pre-amplifier, a shaping amplifier and a multiplexer The schematics of the chip are shown in figure 4 5 There are two different modes, TRACK and HOLD In TRACK mode, charge is continuously collected The charge on the 16 input channels of the amplex is transmitted via a pre amplifier to a shaping amplifier with a typical shaping time of 700 ns The interaction time of a traversing particle in the silicon layer plus the time of the charge collection on the electrodes of the silicon wafer is negligible compared to this shaping time

When the chip is switched from TRACK to the HOLD the output of the shaping amplifier is

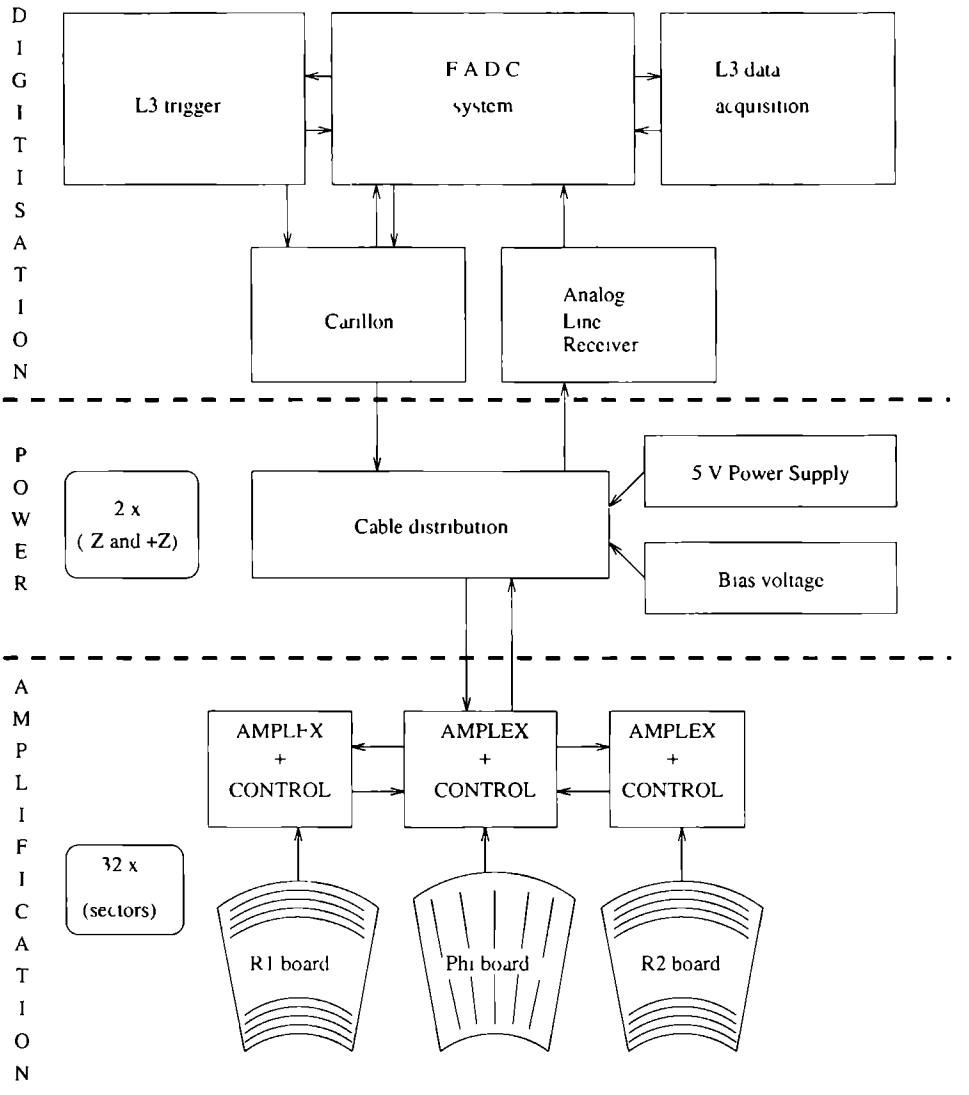

Figure 4.4: *The readout system of the SLUM Inside the detector the* AMPLEX *chips are mounted The power system for both the electronics and the bias voltage of the silicon are located just outside the support tube The FADC system is housed in one of the counting rooms After digitisation the data are merged with the rest of the L3 data on an event by event basis*

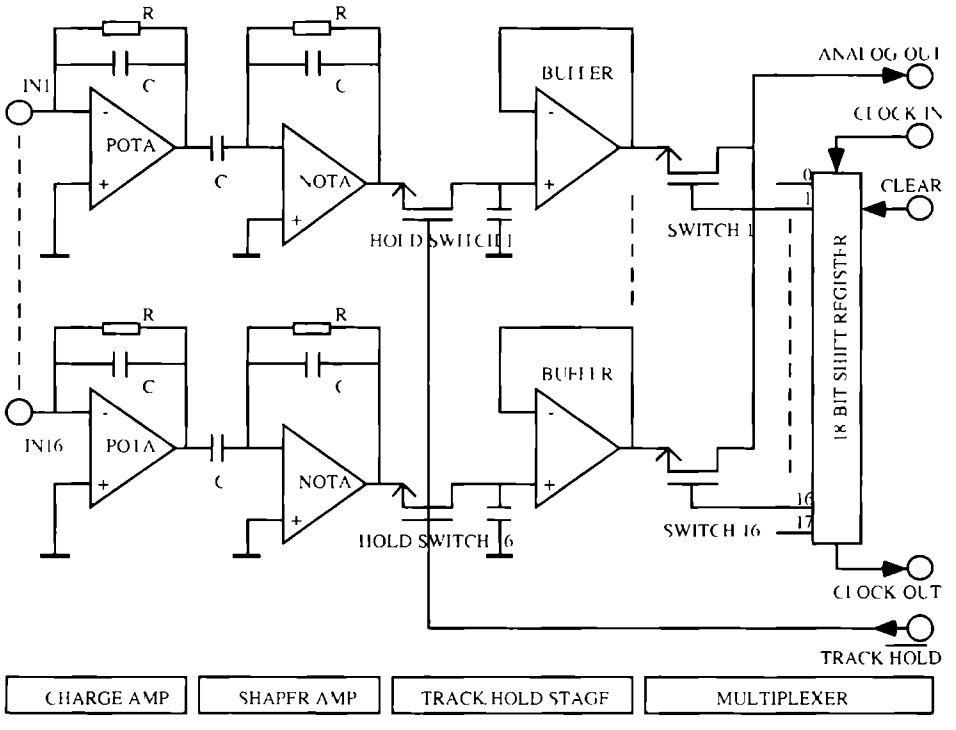

Figure 4.5: *Schematic view of the* AMPLEX *chip. Two out of the sixteen channels of one chip are shown (IN1 and IN16). Three different parts can be clearly distinguished, the charge amplifier (POTA), the shaping amplifier (NOTA) and the multiplexer.*

stored in a buffer, waiting for further readout To optimise the signal to noise ratio the switch from TRACK to HOLD mode, should occur when the charge on the capacitance of the shaping amplifier is maximal This maximum occurs 700 ns (the shaping time) after a particle traversed the detector The TRACK/HOLD timing signal is generated by the carillon and transmitted via a patch panel to all ϕ-sensors Subsequently the electronics on the ϕ sensors transmit the signal to the r sensors After the chip is switched to hold, the signals in its buffer can either be read and transported or cleared This choice depends on the validity of the event a decision made by the L3 trigger system

On each AMPLEX chip a register points to the channel to be read After a positive trigger decision, the chip receives a clock signal from the carillon and on the rising edges of this clock signal the register switches from one channel to the next After all channels have been read, the clock signal is passed on to the neighbouring AMPLEX chip In total a series of 16 chips is read out sequentially All 2x16 sectors are operated in the same way and are processed in parallel The analogue signals are transported differentially from the detector to the counting room Analogue line receivers (ALR) convert them into signals between 0 and 1 Volt The output from the analogue line receivers is directly transmitted to fast analogue to digital converters (FADC s)

The AMPLEX chip is switched back to TRACK mode as soon as a full read cycle is completed, in order to be ready for the next event Also the register pointing to the last channel at the end of a read cycle, has to be cleared so that it points to the first channel again The timing of the control signals such as the TRACK to HOLD switch, the clock and the clear pulse is very critical The timing is explained in section 4 3 3

4.3.3 Digitisation and synchronisation

The L3 data acquisition system sets well defined timing constraints on all operations in a read cycle The operation of L3 is controlled by the general run control program When LEP physics data are recorded the detectors are operated together the GLOBAL mode During beam stops the sub detectors can run independently in their own LOCAL mode The readout of the luminosity detector is completely embedded in the run control program Two processes can be distinguished which enable the communication of the silicon detector with the outside world One is controlled by a program called TAROT (originally designed for the readout of the L3 Time Expansion Chamber, hence the abbreviation meaning TEC And Read Out Task) The TAROT program can be used to download the software instructions for the FADC system For each mode, GLOBAL or LOCAL small programs are sent to the data reduction processor (DRP) described at the end of this section The second process CARIL, controls the communication with the carillon Via this program commands can be send to the carillon unit in order to switch the SLUM readout from GLOBAL to LOCAL

The most important modules in the higher level of the data acquisition system are 32 FADC s with 16 data reduction processors (DRP's) The module enabling the communication between the carillon and the FADC's is called the lumi connector module (LCM)

Two FADC s are located together with one DRP in one logic module The FADC converts a pulse train of analogue signals into digital signals governed by the frequency of a clock signal (1 Mhz) that is received from the LCM The FADC digitises the signal on the rising edge of the clock signal This clock signal together with an example of the analogue pulse train is shown in figure 4 6 Each FADC converts a train of 256 analogue pulses into 256 words of 6 bits each its dynamic range

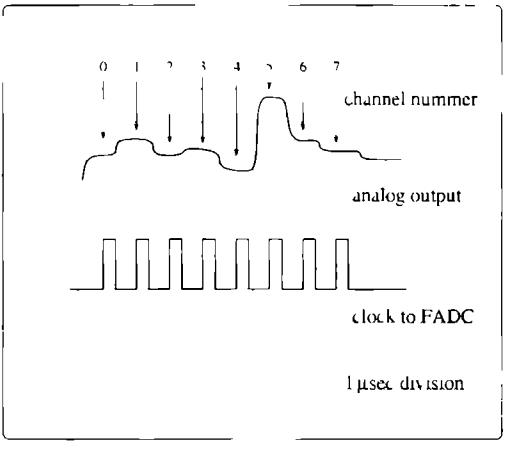

Figure 4.6: *The analogue and a clock signal are simultaneously fed to the FADC The digitisation occurs at the rising edge of the clock signal*

With the DRP an important reduction of the data is obtained For all SLUM channels the pedestals [1] with their standard deviations are stored in the memory of the DRP modules, using the TAROT program For the SLUM readout the DRP is programmed such that only the channels with a signal of at least one ADC count above pedestal are read As a consequence only non empty channels are read and therefore address information is needed The output record of the DRP modules thus contain an address word and a data word for each selected channel

Timing

Various run types

To understand the operation of the DAQ some special attention is given to the synchronisation of the readout signals The most important timing signals, playing a role in the subsequent stages of an event cycle, are discussed

The chronology of an event cycle can differ somewhat for different run modes As mentioned before the SLUM can be operated in LOCAL and GLOBAL mode A third mode has been developed allowing the detector to be operated outside the L3 environment This mode was used in a test beam where the detector was studied prior to installation All signals controlling the synchronisation are generated by the carillon

The data analysed in this thesis are recorded with the LEP machine operating with eight electron and eight positron bunches circulating in the ring The rate of bunch crossings at the interaction point is 88 kHz, thus the time interval between two bunches is 11 2 µs

In GLOBAL mode all L3 subdetectors are read simultaneously Every bunch crossing is fol lowed by a decision of the trigger level one system, TL1 This trigger decision is a logical OR

[1] the average output in the absence of real signal

of the trigger decisions of all subdetectors A positive decision starts the readout sequence of all subdetectors When after a positive level 1 trigger the detector is read out, the SLUM is occupied for approximately 300 μs While a full readout cycle is being executed, all L3 detectors are insensitive for new triggers, introducing a dead time On a negative trigger level 1 decision (a trigger level 1 abort) the detectors are reset and must be ready for the next bunch crossing

When there are no colliding beams in the LEP machines the L3 data acquisition system is switched to LOCAL In this mode test runs and calibrations can be done in which the subdetectors are operated independently In LOCAL mode there are no timing signals or L3 triggers available so they are all generated locally at subdetector level

For the SLUM this time is used to perform calibration runs used for pedestal determination and performance checks

Event cycle

The important timing signals of the event cycle are shown in figure 4 7

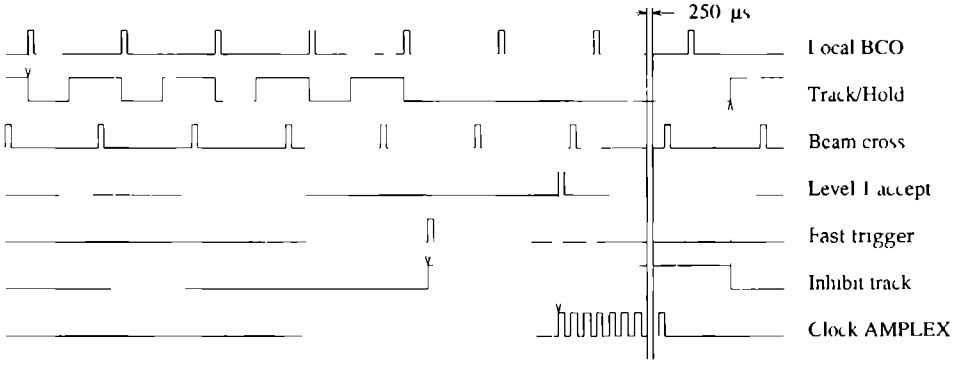

Figure 4.7: *Timing of an event cycle during a global run The dotted lines indicate the edges of a given signal triggering the signal to which the arrow points Note the fast trigger which prohibits the* AMPLEX *to switch back to* TRACK

If none of the L3 detectors is occupied and the trigger decision of the last event was negative then the AMPLEX chip is in TRACK mode at the time a bunch crossing occurs (BCO) Dictated by the shaping time of the AMPLEX chip it is switched 700 ns after the bunch cross to HOLD and the data are buffered

Because the negative L3 trigger decision (skip this event) is too late for a proper reset of the AMPLEX a special trigger is set up, the luminosity fast trigger This trigger is set up similar to the luminosity double tag trigger but during 1993 the thresholds were adjusted to increase its efficiency The luminosity fast-trigger is based on the analogue sum of the BGO luminosity monitor and is positive for a Bhabha candidate After approximately 3 μs the luminosity fast trigger arrives at the carillon, if there is a positive trigger the AMPLEX chip stays in HOLD so that it is ready to be read out If there is no luminosity fast trigger then the AMPLEX chip is switched back to TRACK mode

It has to be noted that the *decision* to switch from TRACK to HOLD is based on triggers whereas the *timing* of the switch is related to the bunch crossing time For this purpose a signal called LOCAL-BCO is used, it is synchronous with the real BCO but it can be shifted in time The LOCAL BCO is always available contains no trigger information and is in principle used as a clock In the luminosity monitor readout the LOCAL-BCO is shifted such that it arrives always after the fast-trigger decision but 5 μs or more before the next beam crossing This critical timing is necessary because the AMPLEX chip must be in TRACK mode for at least 5 μs before its voltage output level is stable and the noise level is acceptable

After a positive fast trigger the system waits for the L3 level 1 trigger decision This trigger is generated two microseconds before the next BCO When a positive level 1 decision arrives the FADC system generates a signal that starts the actual readout this signal is called LUMIGO A negative level 1 decision triggers the detector to be ready for the next BCO as soon as possible There are four different states that can occur The first two situations are common situations 3 and 4 are expected to be rare in normal LEP conditions

1 The luminosity fast trigger is negative and the L3 trigger level 1 is negative The AMPLLX is in TRACK and is ready for the next event as is the rest of the detector There is no readout and not a single beam crossing is missed

2 The luminosity fast trigger is positive and the L3 trigger level 1 is positive The AMPLLX is in HOLD mode and on the generated LUMIGO the readout will start This is a valid event for the luminosity analysis The readout is completed in 300 μs Numerous beam crossings are skipped

3 The luminosity fast trigger is negative and the L3 trigger level 1 is positive After the BCO the AMPLEX chip will still be in TRACK mode although L3 readout cycle is starting This trigger sequence will be detected by the carillon and a zero volt signal will be generated on the input of the FADC This procedure prevents corrupted SLUM information being used in the analysis

4 The luminosity fast trigger is positive and the L3 trigger level 1 is negative
This situation can occur because the fast trigger is not part of the L3 level one trigger (it is said to be inactive) The AMPLEX is in HOLD mode after the positive luminosity trigger but the L3 trigger is negative and the detector is required to be ready before the next bunch crossing The AMPLEX will have been switched to TRACK but not in time Since it should have been in TRACK mode for at least 5 μs it is not ready to capture the coming event in a proper way The carillon will detect this trigger sequence and again generate a zero output

The carillon

The carillon is the central control unit of the exchange of all timing and control signals in the first and second level of the readout of the silicon detector It forms the interface between the local electronics on the printed circuit board and the FADC system

The carillon generates all control signals needed by the first level electronics on the detector The silicon detectors at both sides of the interaction point are not at an equal distance from the counting room Therefore all signals to the nearest detector have to be delayed as the analogue

signals of all 32 sectors of the detectors have to arrive simultaneously at the FADC s Inside the carillon, programmable delays enable synchronisation of the TRACK/HOLD switches the clock to the AMPLEX and the reset signals for both sides (z and +z) of the detector

A small micro processor inside the carillon makes it possible to change the values of the delays to select the run mode and to set the parameters of the test mode A program interpreted by this processor is stored on an EPROM [2] The flow chart of this program is shown in figure 4 8 It allows a fast switching between the different run modes

After every external reset or power failure the program stored in the EPROM will automatically reset all parameters such that the carillon is ready for GLOBAL data taking

The carillon provides a test-BCO signal in case of a local run In combination with this TEST BCO a test pulse can be sent from the carillon to the silicon wafers on the detectors

4.3.4 Calibration

The printed circuit board includes a circuit allowing to test the performance of the board and the silicon sensor The electronics on the board can be tested separately as well as in combination with the silicon sensor strips The electronics are tested by pulsing the input pads of the AMPLEX chips via capacitive coupling A voltage modulation is applied on a metal strip, implemented in the printed circuit board just below the input pads of the AMPLEX chip Either the odd or the even numbered channels can be pulsed This is the so called *odd even* test A voltage modulation on the bias voltage on the backplane of the silicon sensor can be applied, to test all the strips of the silicon sensor, a *backplane* test In this case not only the electronics are tested but also the strip and the bond In figure 4 9 the results of both an *odd even* test and a *backplane* test are shown

Generally the silicon luminosity monitor is operated in data reduction mode The values of the pedestals and their standard deviations stored in the data reduction processors are obtained with a *backplane* type of run The only difference is that the modulation of the voltage is zero To achieve a high reliability of this method, the pedestal data should be updated regularly In practice these pedestal calibration runs are therefore taken on a daily basis in between fills An additional reason for taking calibration runs is the need to keep track of dead or, on the contrary, noisy channels In the 1993 run four dead channels were found and five channels had such an elevated noise level that they were declared dead on the analysis level During 1993 the pedestal values have shown to be very stable The evolution of their values and *rms* values are shown in figure 4 10

[2] Erasable Programmable Read Only Memory

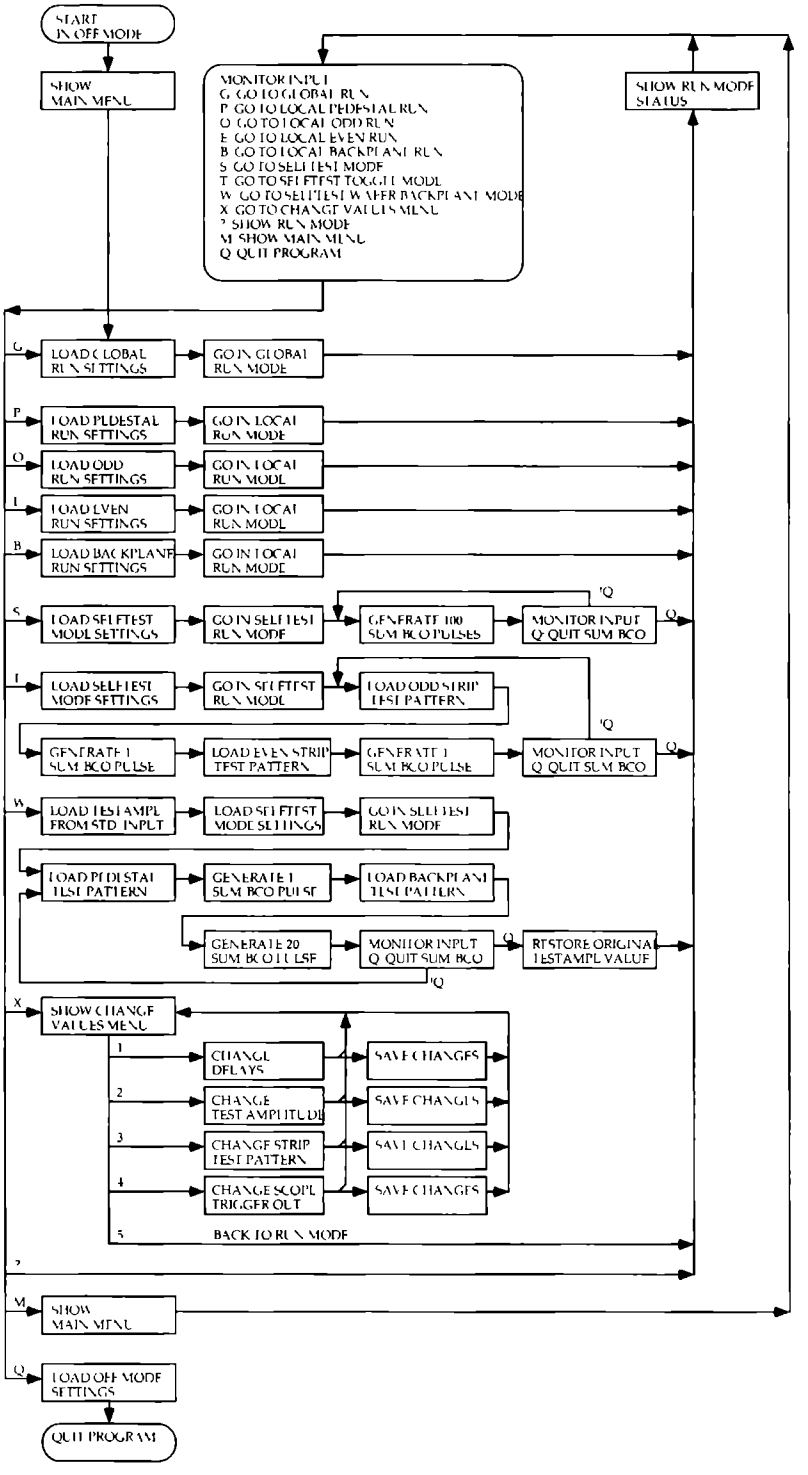

Figure 4.8: *Flowchart of the carillon control program.*

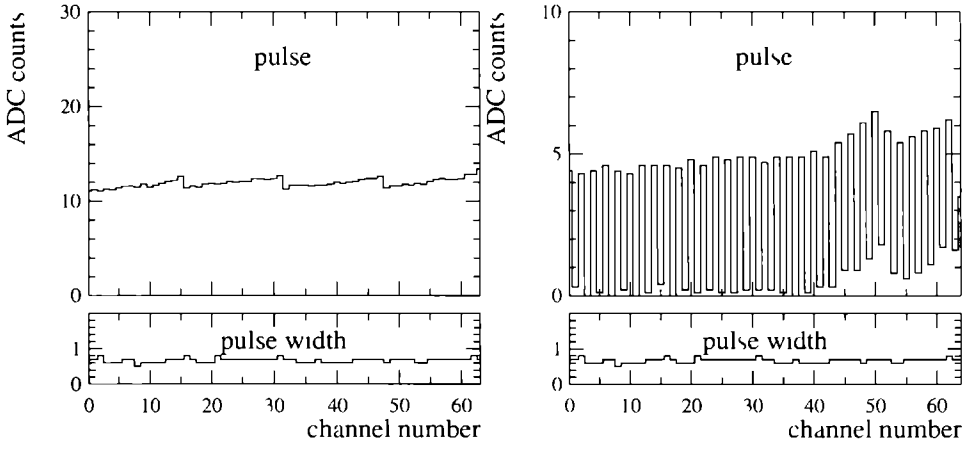

Figure 4.9: *Testing one ϕ-sensor by pulsing the backplane (left) and the inputs of the* AMPLEX *chip for even strip numbers (right)*

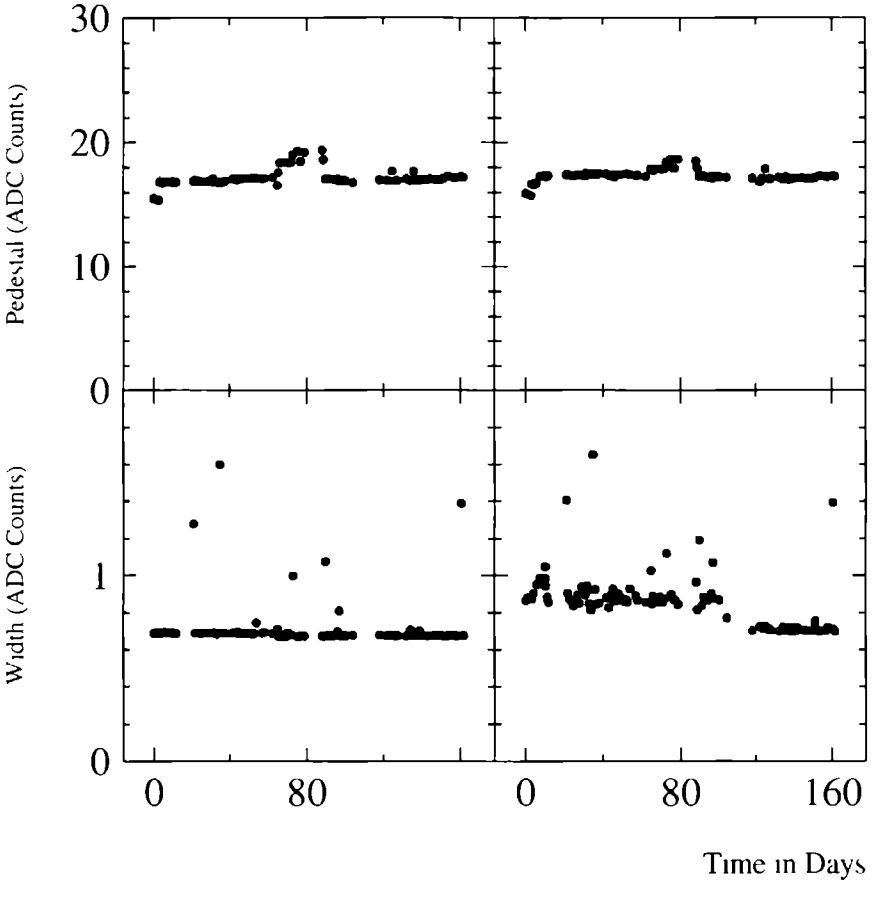

Figure 4.10: *The online pedestal stability during 1993 (top) The evolution of the pedestal width is indicated as well (bottom)*

Chapter 5

Event reconstruction

5.1 Introduction

The identification of Bhabha events and their acceptability depend on energy and position measurements. The exact selection criteria and the subsequent calculation of the luminosity are presented in chapter 6. This chapter describes the procedure to translate the recorded detector signals into physics coordinates.

The triggering of Bhabha events and the processing of the data are described first. Secondly the energy calibration of the BGO and the method used for the reconstruction of the energy and impact point of an incoming particle are presented. Thirdly the position measurement using the SLUM is explained. The treatment of multiple hits is especially important in this procedure. The origin of these multiple hits has been studied in a dedicated experiment in which the detector was exposed to a 50 GeV electron test beam.

A distinction is made between global and local coordinates. local coordinates are relative to the centre of either the BGO or the SLUM, whereas global coordinates are related to the centre of the L3 detector or more precisely the actual interaction point. The two coordinate systems differ by geometrical imperfections in the location of the luminosity monitors. To relate the impact point in the BGO with the hits in the SLUM the local BGO coordinates are translated to coordinates in the SLUM frame. The alignment of the BGO and the SLUM is described in the last part of this chapter.

5.2 Trigger and Data Flow

During a L3 physics run data are collected on tape with an event rate which is approximately 5 Hz. Each event contains the information of all L3 subdetectors together with the trigger information of the event.

The digitised sums of the analogue signals from each BGO sector are used to decide whether a possible Bhabha event has occurred. To avoid the loss of Bhabha candidates on sector boundaries the signals of two adjacent sectors are added. The trigger decisions are optimised such that the trigger rate is not excessive since each event reading causes several bunch crossings to be skipped. Yet there is a need for a highly efficient trigger to be satisfied as well. The total rate of the trigger in normal background conditions is 2-3 Hz. Approximately 25% of these events are selected for

the final sample of Bhabha events for the luminosity calculation The trigger decision is based on three trigger conditions

1 **The lumi trigger.**
An energy deposit of at least 15 GeV on both sides of the interaction point is required In addition the sectors where these energy deposits are observed have to be 'back to back'

2 **The double tag trigger.**
On one side of the interaction point an energy deposit of at least 15 GeV and on the opposite side more than 25 GeV is required This trigger is especially useful in recovering Bhabha candidates in which part of the energy was lost in a dead crystal

3 **The single tag trigger.**
An energy deposit of at least 30 GeV on one side of the interaction point is required Only one out of 40 triggers is accepted Events with a single tag trigger are used to determine the trigger efficiency of the two triggers mentioned above In the off-line analysis the events selected as genuine Bhabhas but only triggered by the single tag trigger count as inefficiency, ε

$$\varepsilon = \frac{N^{\text{Bhabha}}_{\text{single tag only}}}{N^{\text{Bhabha}}} \tag{5 1}$$

where the scaling factor of the single tag trigger is taken into account in $N^{\text{Bhabha}}_{\text{single tag only}}$

Off line, the L3 data reconstruction program (REL3) splits the raw data into several streams containing information dedicated to a specific physics topic The data streams which are used for other than the luminosity analysis are not discussed in this thesis A description of the complete L3 reconstruction can be found in the L3 computing guide [37]

Events with a valid luminosity trigger are saved on the so called LDRE stream (Luminosity Data REduction) The LDRE data is stored on tape, each tape summarising the data from many raw DAQ tapes To facilitate the luminosity analysis another stream is subsequently stored on disk the FBSB banks (Forward BGO Special Bank) These fast accessible files are a subset of the LDRE data, containing part of the reconstructed information The FBSB files are used for alignment and performance studies and are not suited for the final calculation of the luminosity

The geometry corrections, calculated using the FBSB files, are stored in a database and used for the final luminosity calculation In the same database the results of the LEP external survey measurements are stored as well

For the simulated events the data flow is likewise The detector response of the particles produced in the events generated with the Bhlumi programme is simulated using the software package GEANT [38] The Monte Carlo events are then saved in separate LDRE streams and FBSB files and can subsequently be treated in exactly the same way as the real data For the 1993 luminosity determination 4 1 million Bhlumi events are simulated

5.3 BGO

5.3.1 Energy calibration

The energy deposit in a crystal is proportional to the current output of the photo diode on the back-side of the crystal and after digitisation to the recorded pulse height in ADC counts This relation

between energy and pulse height, the *gain*, is determined separately for each crystal. The gain is expressed in number of ADC counts per MeV and is determined in the off-line analysis using the knowledge that a non radiative Bhabha event results in an energy deposit equal to the beam energy on both sides of the interaction point. Therefore the following equation holds

$$\sum_{i}^{N}(ADC^{i}_{\text{pulse}} - ADC^{i}_{\text{pedestal}}) \cdot gain^{i} = E_{\text{beam}} \tag{5.2}$$

where the sum is taken over all crystals in a cluster, with a signal higher than a certain threshold. For a set of calibration events the gains are optimised until a good calibration is accomplished. The pedestals are determined for each LEP fill and typically drift less than 0.4 MeV where the deposited energy ranges from 200 MeV to 20 GeV per crystal.

If serious radiation damage occurs the gain of the crystals can be calibrated for different periods. In 1993, however, the energy calibration was performed for the whole data sample at once.

5.3.2 Shower fit

The position determination of the impact point in the BGO is extracted from the comparison of the distribution of the energy over the crystals with a known electromagnetic shower shape. The energies are expressed in fractions, to allow for a fit procedure which is independent on the energy of the incoming particle. These fractions are defined as the energy deposit in one crystal divided by the sum of the energy deposits in all crystals.

A given particle with energy E_{tot} deposits only a part of its energy in the BGO, E_{dep}. The expected average fraction of this energy deposited in a crystal i is $E^{i}_{\text{predicted}}$. It depends on the crystal's distance to the impact point, ρ. The average transverse shower shape is parametrised by:

$$\mathcal{S} = A_0 \cdot \delta_{\rho=0} + A_1 \cdot e^{-\rho/\sigma_1} + A_2 \cdot e^{-\rho/\sigma_2} \tag{5.3}$$

with $\int_0^\infty \mathcal{S}(\rho)d\rho = \frac{1}{2\pi}$. A_i and σ_i are constants determined with a Monte Carlo study. Using this parametrisation a database entry is made with the predicted fractional energy loss in each crystal, for each possible impact point, on a finite grid. To determine the impact point of a real track, a χ^2 fit is used in which the observed energy fraction in a crystal, E^{i}_{observed}, is compared with the predicted fraction varying the impact point.

$$\chi^2 = \sum_{i=1}^{N} \frac{(E^{i}_{\text{predicted}} - E^{i}_{\text{observed}})^2}{(\Delta E_i)^2} \tag{5.4}$$

where N is the number of crystals and ΔE_i is the estimated error in the fractional energy. The r and ϕ coordinates of the impact point are varied around a starting value which is obtained by a 'centre-of-gravity' calculation. In this case the positions of the centres of the hit crystals are averaged with a weight corresponding to the observed pulse height. The value of χ^2 provides an indication whether the shower originated from an electron or photon, or rather a hadron. The resulting accuracy in the impact point is about 1 mm. The z coordinate is fixed for all tracks; it is defined as the point where the energy density of the shower is at its maximum.

After the impact point is determined with this shower fit, a final correction to the total deposited energy, E_{dep}, is made to improve the estimate of the energy of the incoming particle, E_{tot}.

$$E^{\text{tot}} = \frac{E_{\text{dep}}}{\sum_{i=1}^{N} E^{i}_{\text{predicted}}} \tag{5.5}$$

In this way known imperfections like dead crystals, are automatically taken into account (once a crystal is declared dead the predicted energy fraction is always smaller than one, therefore the total energy is increased)

If more than one cluster can be reconstructed inside one BGO detector, their position and energy are used to determine the momentum vectors corresponding to each cluster If solely the BGO is used the momentum vectors are summed This summation provides the energy and momentum of the originally scattered particle In a study of photon radiation in the final state of a Bhabha event (see chapter 7), the clusters are summed as well to determine the momentum of the electron and photon together In the following description of the event reconstruction for the luminosity determination the BGO impact point is however matched to the track in the silicon under the assumption that the most energetic cluster in the BGO calorimeter corresponds to the electron (positron)

5.4 SLUM

5.4.1 Pedestal subtraction

An important step in the analysis of the silicon information is the selection of strips that are hit A first, conservative reduction of channels was already obtained online by demanding that the signals must have a pulse height at least one ADC count above their pedestal value In some parts of the detector the electronic noise in different channels is correlated To take this correlated part of the noise into account, on an event by event basis, one strip per pitch region is always read The average value of the output of these channels is used to determine a correction so that the real pedestal value of the event can be estimated

After the correlated noise correction the *rms* value of the pedestal fluctuation turns out be 0 7 ADC counts After the pedestal is subtracted from the observed pulse height, the average signal is 10 ADC counts The signal over noise ratio is therefore 14

To select strips that are hit the, pedestal subtracted, signal must satisfy the following require ments

1 **Signal height larger than 5 ADC counts.**

2 **Signal height larger than one sigma.**
This requirement is only effective in case of extremely noisy channels

Each detector hit is now translated in a set of local coordinates, r, ϕ and z, given by the locations of the centre of the strip, Δr and a $\Delta\phi$ are assigned corresponding to the total size of the strip in r and ϕ respectively

To reduce the influence of noisy hits a window around the reconstructed impact point in the BGO calorimeter is formed Only strips within this window are considered for further analysis In order to make a correct extrapolation from the BGO calorimeter to the silicon tracker the two detectors have to be aligned with respect to each other (see section 5 5)

	η_{double}
pions, no material	0 03
electrons, no material	0 11
electrons 0 1 X_0	0 13
electrons 0 2 X_0	0 16
electrons 0 3 X_0	0 25
electrons 0 4 X_0	0 32

Table 5.1: *The results for η_{double} from test beam data the quoted values do not include the material of the detector itself*

5.4.2 Multiple hits

The silicon sensor size and strip pattern is designed such that the signal generated by one traversing particle is typically collected on one strip Ideally a Bhabha event would result in one fired strip per layer per event In practice events are sometimes recorded with multiple strips hit This effect has been studied in a test beam

In the test beam, in the CERN west area, two silicon sectors were placed in front of one BGO sector The reference track coordinates were determined with the help of a straw tube detector placed in front of the silicon detector Two plastic scintillators provided a trigger when a coincident hit occurred The test beam consisted of 50 GeV electrons or pions

The following effects, known to cause multiple hits, have been examined

1 **Multiple particles.**
Due to secondary particles traversing the detector simultaneously with the electron more than one strip can be hit Before entering the sensitive part of the detector the particles traverse a certain amount of material the detector cover and parts of the detector itself To examine the effect different amounts of extra material were placed in front of the detector The traversing electron can either radiate a photon (Bremsstrahlung) or knock out an electron (δ ray emission) If the opening angle between these two particles is large enough two neighbouring strips can be hit A photon will only be observed if it converts into an electron-positron pair A comparison with pions is made because the probability that pions produce secondary particles is small compared with electrons Since the electron and the pion both deposit the same amount of energy the detector response is similar for both particles In figure 5 1 (top) the difference in multiplicity distributions is shown for both pions and electrons To make a quantitative comparison which is not dependent on the trigger inefficiency, the amount of observed hit multiplicity is defined as

$$\eta_{\text{double}} = \frac{N_{\text{double}}}{N_{\text{double}} + N_{\text{single}}} \tag{5 6}$$

The values for η_{double} determined from the test beam data are summarised in table 5 1 From this data it is therefore concluded that the majority of the double hits are caused by secondary particles, rather than by other effects discussed below A maximum of three percent of double hits can be explained by real detector effects

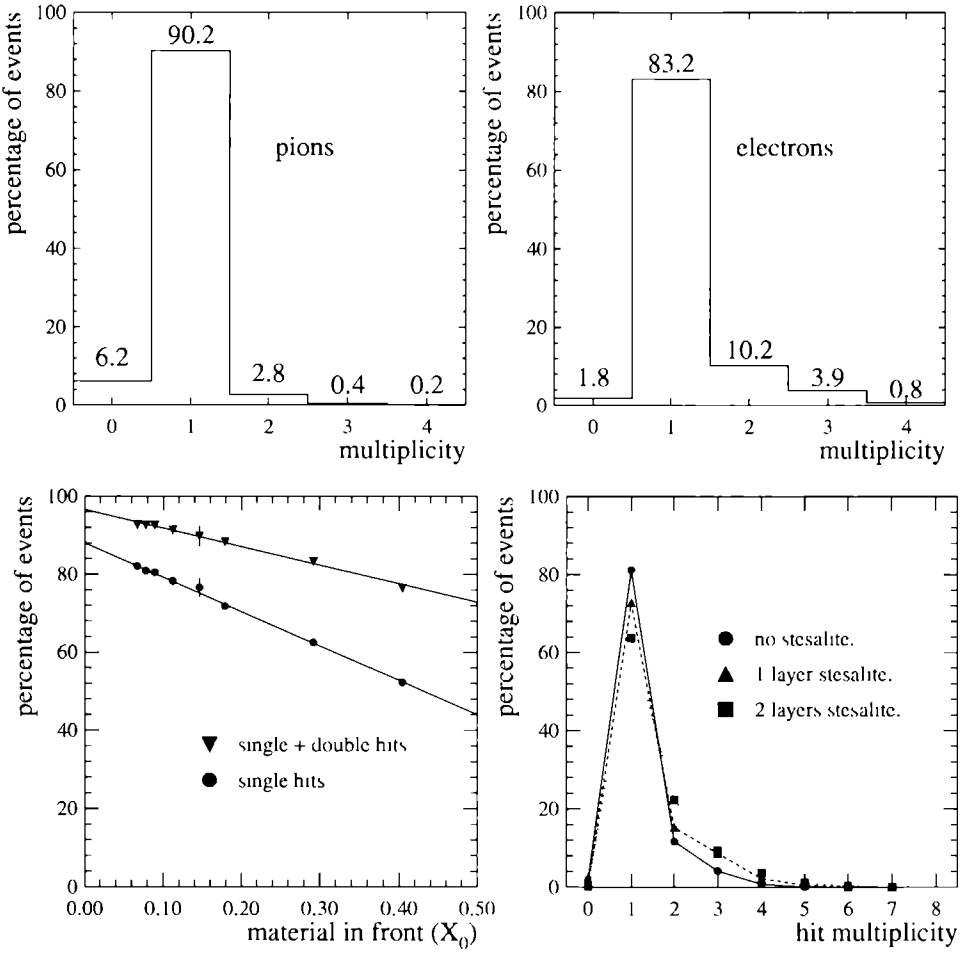

Figure 5.1: *Results from the 50 GeV testbeam. The main difference in the behaviour of pions and electrons is the amount of secondary particles they produce. From data taken with pions (top left) it is therefore proven that the double hits are mainly caused by secondary particles. Only 3 percent of the pions cause double hits, for electrons (top right) this is 11 percent. For electrons the influence of material on the hit multiplicity is shown (bottom). Both the material in front of the detector (left) and the material of the Stesalit layers is important (right).*

In figure 5 1 (bottom) the multiplicity is shown as a function of the amount of material in front of the detector From this plot an estimate can be made of the total amount of material seen by the particles from the detector itself If these points are extrapolated to the point where η_{double} is 0 03, as with pions, the number of radiation lengths is –0 08 This is a reasonable number since the (test beam) detector cover consisted of a 1 mm thick brass plate, corresponding to 0 07 radiation lengths The effect of the detector support material is shown in this plot as well A clear difference is observed in the multiplicity distributions for the first, second and third layer of the detector

2 **Backscattering.**
The electromagnetic shower developing in the BGO may cause particles to backscatter into the silicon detector In the testbeam it was possible to remove the BGO sector and compare the resulting number of double hits No significant difference is observed

3 **Charge sharing.**
When a particle traverses the detector between two strips (up to a few microns from the exact centre) the created charge is distributed over both strips The ratio of the double hits over the single plus the double hits observed with the pion beam, shows that the charge is shared over two strips in only 3% of the cases This three percent still includes the effects of the presence of multiple particles and therefore is a worst case' estimate In the L3 setup the fact that the particles enter the detector typically at an angle of 35 mrad contributes as well, such a particle traversing a 300 μm thick detector corresponds to a transverse displacement of 10 μm, thus causing double hits in a maximum of 2% of the events (obtained by the ratio of the displacement and the typical strip pitch) The degree of charge sharing is influenced by the threshold cut made on the signal In case of a micro strip detector the charge sharing can be used to increase the resolution

4 **Noise.**
Electronic noise somewhere along the readout line causes a fluctuating pedestal signal De pending on the size of the fluctuation this can give rise to a noise hit high enough to pass the pulse height cuts To prevent these hits from biasing the position measurement extremely noisy strips are detected by analysing pedestal runs and subsequent removal of these chan nels in Monte Carlo and data samples During 1993 four strips were found to be noisy hav ing pedestal widths of more than 2 5 ADC counts For the other strips with an average *rms* of 0 7 ADC counts the expected amount of fake hits is expected to be very small

Another effect observed in the test beam data, is an increased amount of multiple hits in the regions where the stainless steel alignment pins of the silicon sensors are located The location of the alignment pins with the resulting increase in multiplicity is shown in figure 5 2 From this study an allowed region is determined for the boundaries of the fiducial volume For the inner boundary this region is determined to be 78 mm $< r <$ 90 mm The outer boundary has to be larger than 140 mm (not shown in the plot)

For the detectors placed in L3 the multiplicity is examined as well The hit multiplicity distri butions for the fine pitched region of all r measuring layers, are shown in figure 5 3 The distri-butions are given for both data and Monte Carlo events At this point certain asymmetries arise between the different r-measuring layers A specially shaped beam pipe is installed on the $+z$ side

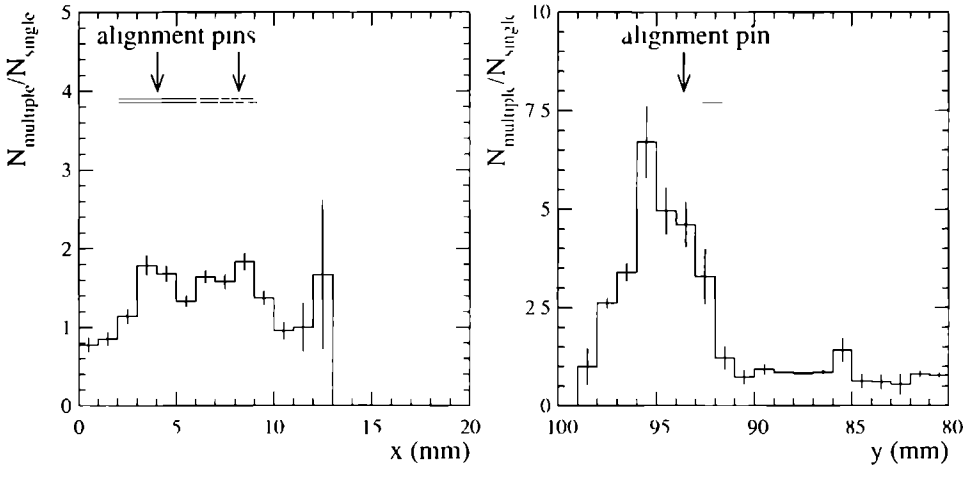

Figure 5.2: *Results from the test beam The correlation between the increased amount of multiple hits and the position of the alignment pins is shown for both the x position (left) and the y position (right) The distribution is obtained by normalising the multiple hits with the single hits The given coordinates are in the testbeam reference frame*

The shape of this beam pipe is designed such that the amount of material in front of the region where the inner boundary of the fiducial volume is situated is minimal Unfortunately it is not possible to install a similar beam pipe on the other side of the interaction point since the L3 micro vertex detector is slid in over this part of the beam pipe during installation, this requires a flat horizontal beampipe This difference in beam pipe structure accounts for the different hit multiplicities for the $-z$ and the $+z$ detectors, as can be seen in figure 5 3

The distributions show that the effect of material in front of the detector is slightly underestimated in the Monte Carlo simulation Therefore the algorithm used for the interpretation of multiple hits, in the luminosity analysis is of critical importance

After the rejection of noise hits the next step in the analysis is the determination of one impact point per event and per layer The events are split up in three categories according to number of hit strips inside a window, projected onto the silicon in front of the most energetic bump in the BGO The size of this window is 5 mm in the r-direction and 2 5 degrees in the azimuthal direction A region of interest is thus created in each layer of the SLUM. The following cases are distinguished

1. **No hits in region of interest.**
   There are no hits inside the window due to inefficiency of the silicon itself (proven to be around 1%) or inefficiency of the fast trigger (1%) The position of the shower in the BGO calorimeter is used as impact point The coordinates are translated to the silicon frame with the help of the results described in the next section

2 **One hit in region of interest.**
   Only one fired strip lies within the window As can be concluded from the multiplicity dis-

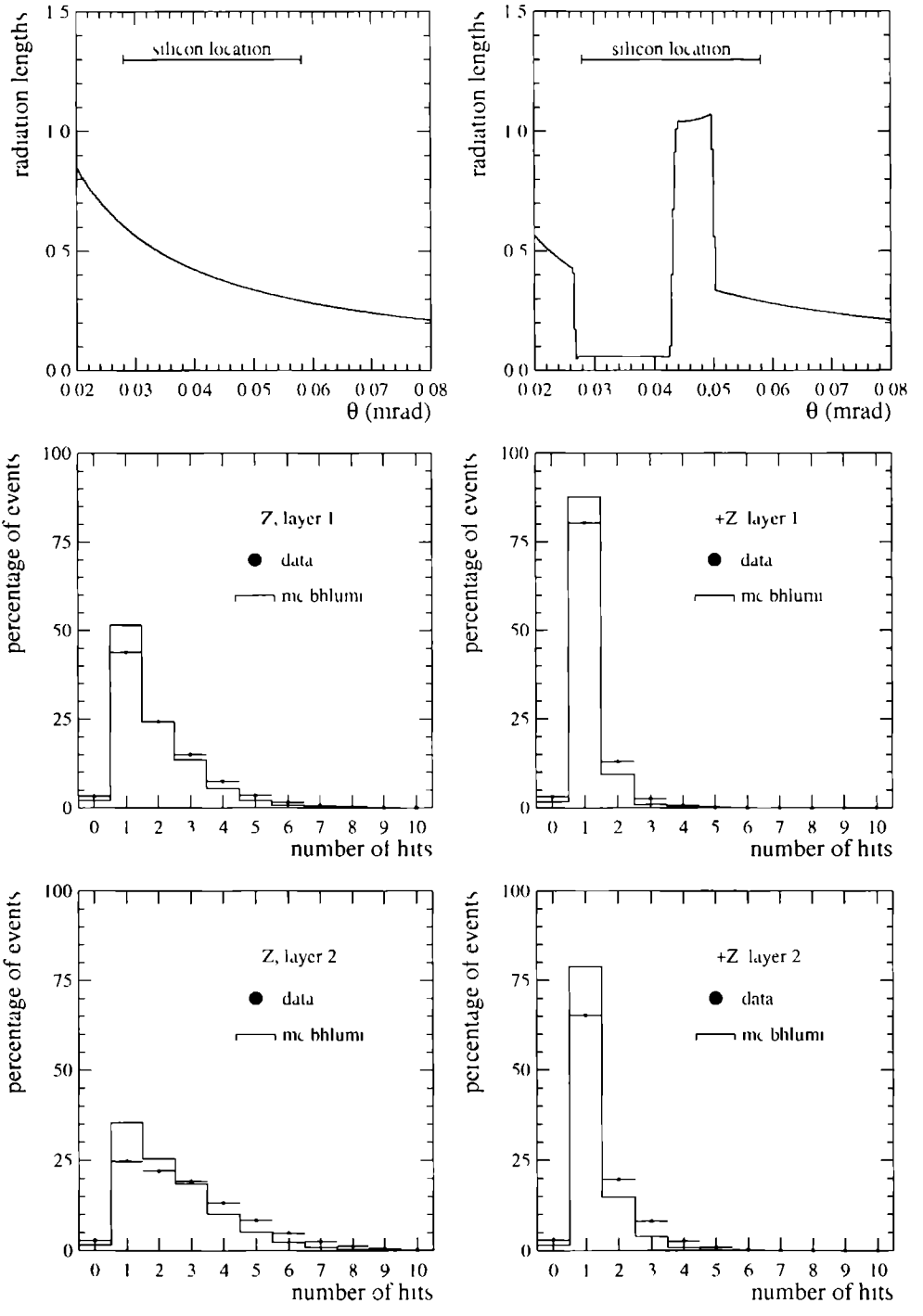

Figure 5.3: *The amount of material in front of the detector seen by a particle emitted at the vertex at an angle θ on −z side (top left) and +z side (top right). On the bottom plots the resulting hit multiplicity distributions in the small pitch region of the first r-layers (middle) and the second r-layers (bottom)*

tributions the largest part of the events fall in this category Although in the first layer on $-z$ only 43% of the hits are single, the first layer on $+z$ has 81% single hits In this case, the position of the centre of the fired strip is used as the impact point

3 **Multiple hits in region of interest.**
More than one strip is fired in the region of interest There are several ways to assign the impact point in this case In the analysis described in this thesis one of the hits is randomly selected It is crucial that no bias is introduced on the overall selection of events and therefore the position resolution is not the most important issue here Another way to determine the impact point is to average the positions of the fired strips The averaging can be performed with the assignment of a weight to each strip The weight is determined by the pulse height of the signal on the strip To use the weighting method correctly the Monte Carlo events should be simulated with realistic pedestals and gains At present the Monte Carlo simulation generates equal pedestals and gains for each channel The advantage of random selection is that the resulting impact point is still expressed in terms of discrete strip numbers and the sharp boundary between the silicon strips can be fully exploited

Summarising the reconstruction method used so far, the BGO provides an energy determination as well as a space point for the reconstructed electron (positron) shower on each side of the interaction point For the events with silicon hits the SLUM provides two space points on each side, to obtain real space points for each r-measuring layer, the measured ϕ-coordinate is extrapolated to both layers assuming a track follows a straight line from the interaction vertex to the luminosity detector

5.5 Alignment of the calorimeter and the tracker

After the installation of the luminosity monitors the knowledge of the detector positions is of the order of a few millimetres The subsequent survey of the BGO is performed with a precision of 300 μm The survey precision of the SLUM position was in the order of a millimetre for 1993, due to the failure of one of the survey tools A precise relative alignment between the BGO and the SLUM is obtained using the recorded data The alignment of the detectors with respect to the centre of the beam is discussed in the next chapter

Schematically, the offsets can be pictured as shown in figure 5 4 One module of the BGO calorimeter, i e one half detector, is shown as seen from the silicon detector frame The alignment of the two detectors is based on the fact that high momentum tracks produced at the vertex result in θ and ϕ hits in the BGO and the SLUM which should coincide Due to offsets and rotations between the two detectors the measured BGO coordinates differ from the measured silicon coordinates The effects of the magnetic field are absorbed in the rotation offset between the two detectors The BGO coordinates expressed in the silicon frame are

$$\begin{aligned} x_{bs} &= x_{bgo}\cos\Delta\phi - y_{bgo}\sin\Delta\phi + dx \\ y_{bs} &= x_{bgo}\sin\Delta\phi + y_{bgo}\cos\Delta\phi + dy \end{aligned} \tag{5 7}$$

where $\Delta\phi$ is the rotation angle, dx and dy are the offsets of the BGO with respect to the centre of the silicon tracker, x_{bgo} and y_{bgo} are the local BGO coordinates and x_{bs} and y_{bs} are the BGO coordinates expressed in the silicon frame With the help of this equation, a chi-square minimisation

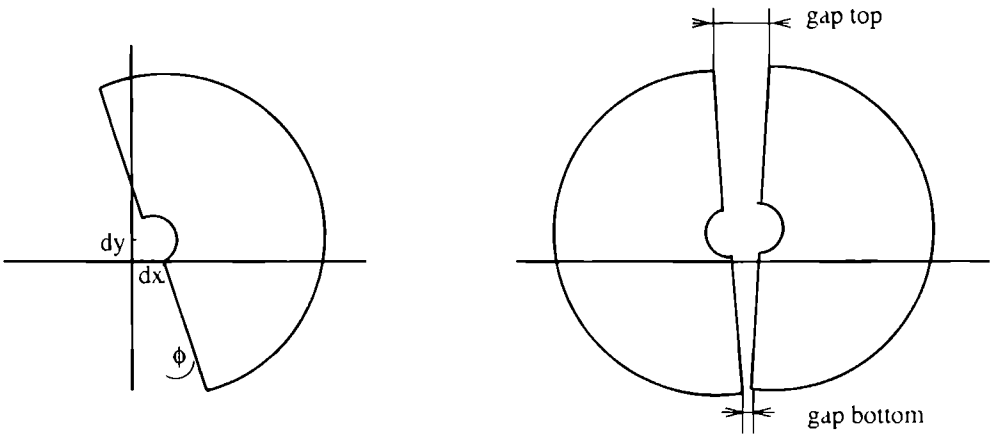

Figure 5.4: *The offset of one BGO module with respect to the silicon tracker*

is performed to determine values of the rotation angle and the offsets The chi square is defined as

$$\chi^2 = \sum_{i=1}^{N} \left(\frac{(x_{bs} - x_{sil})^2}{\Delta x^2} + \frac{(y_{bs} - y_{sil})^2}{\Delta y^2} \right) \tag{5 8}$$

where x_{sil} and y_{sil} are the coordinates of a track measured by the silicon tracker, N is the number of events To perform this fit in an unbiased way only Bhabha events are selected with a single strip hit in the silicon The fit is performed for each run period separately but has shown to be very stable In table 5 2 the results of the fit for the BGO calorimeter modules on $+z$ and $-z$ are shown for the periods 93a, 93b and 93c, separated by a LEP shutdown period

Comparing the offsets in the x direction of the two half detectors, and using the fitted rotation the gap between the two halves is calculated The gap is found to be in the range from 2 1 mm (3 9 mm) at the top to 0 8 mm (0 9 mm) on the bottom side of the BGO, for the detector on the $+z$ ($-z$) side Comparing the gap size for different LEP fills it is shown that the opening and closing mechanism of the BGO calorimeter is reliable as can be seen from table 5 3

The fit is performed on the Monte Carlo sample as well, in this case only an offset in dx should be found, caused by the gap The fitted gap size of 1 4 mm (table 5 2) agrees with the gap size which is implemented in the detector simulation of 1 6 mm The small difference between those two numbers can be explained by the uncertainty in the position of the shower maximum along the z axis For all further analysis the BGO coordinates are translated to coordinates in the silicon frame

In figure 5 5 the resulting alignment between the BGO and the silicon is shown Shown is the difference between the reconstructed BGO coordinate and the silicon coordinate after the offsets obtained from the fit have been implemented

Monte Carlo				
	-x,-z	+x,-z	-x,+z	+x,+z
$d\phi$	-.001	-.001	.000	.000
dX	.890	-.884	.762	-.763
dY	-.009	-.017	.019	.036
1993 data, period A				
	-x,-z	+x,-z	-x,+z	+x,+z
$d\phi$	-.012	.002	-.003	.005
dX	-.062	-1.516	3.397	2.725
dY	-2.638	-3.077	-.704	-1.033
1993 data, period B				
	-x,-z	+x,-z	-x,+z	+x,+z
$d\phi$	-.012	.002	-.003	.005
dX	-.092	-1.536	3.374	2.698
dY	-2.613	-3.062	-.726	-1.010
1993 data, period C				
	-x,-z	+x,-z	-x,+z	+x,+z
$d\phi$	-.012	.002	-.003	.005
dX	-.089	-1.544	3.307	2.692
dY	-2.606	-3.064	-.711	-1.002

Table 5.2: *The offset of the BGO modules on $-z$ and $+z$ for 1993, both for data and Monte Carlo.*

fill nr.	gap size
1	1.39
2	1.42
3	1.38
4	1.46
5	1.39
6	1.39
7	1.38
8	1.36
9	1.38
10	1.34

Table 5.3: *The gap size for different fills during one week, the average gap is 1.38 mm with an rms value of 0.04 mm.*

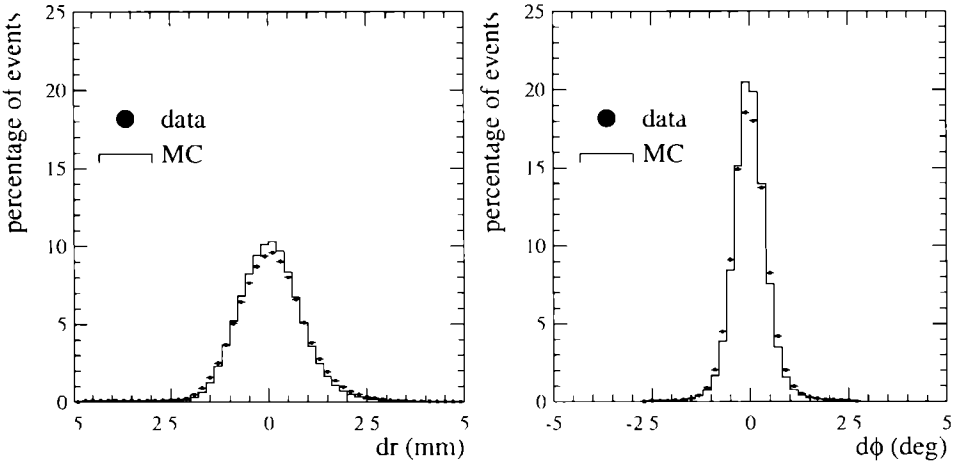

Figure 5.5: *The difference between the reconstructed BGO coordinate and the silicon coordinate. Both the difference in the r-coordinate (left) and the ϕ-coordinate (right) are shown. The widths of the r-distributions are 0.85 mm (MC) and 0.99 mm (Data). The widths of the ϕ-distributions are 0.47 (MC) and 0.50 degrees (data).*

Chapter 6

The Luminosity determination

6.1 Introduction

The method of the calculation of the integrated luminosity is presented in this chapter starting with the equation

$$\mathcal{L} = \frac{N_{\text{Bhabha}}}{\sigma_{\text{vis}}} \tag{6.1}$$

where N_{Bhabha} is the number of selected events, and σ_{vis} is the visible cross section

In section 6.2 the selection of Bhabha events is presented. Important for the event selection is a quantitative study of possible backgrounds and of the trigger efficiency. In section 6.3 the determination of the visible cross section using the Bhlumi Monte Carlo program, is given. It is explained how small differences between the detector geometry in the data and the Monte Carlo are taken into account to obtain the desired accuracy.

The chapter is concluded with a presentation of the resulting luminosity and a discussion on the possible remaining sources of systematic uncertainties.

6.2 Event selection

6.2.1 Selection criteria

A typical small angle Bhabha event is shown in figure 6.1. The parameters relevant to the selection of Bhabha events are **the scattering angles** θ_1 and θ_2, of respectively the scattered electron and positron, **the energies** E_1 and E_2, deposited in the calorimeters, and finally **the azimuthal angles** ϕ_1 and ϕ_2.

Given energy and momentum conservation the energies E_1 and E_2 are both equal to the beam energy and the scattered electron and positron lie in one plane with the beam line. Therefore events are identified as Bhabha events when they satisfy the following criteria:

1. **Energy conservation.**

$$\begin{aligned} E_{\min} &> 0.4\ E_{\text{beam}} \quad \text{and} \\ E_{\max} &> 0.8\ E_{\text{beam}} \end{aligned} \tag{6.2}$$

where $E_{\min}$ is the minimum and $E_{\max}$ the maximum value of the energies E_1 and E_2.

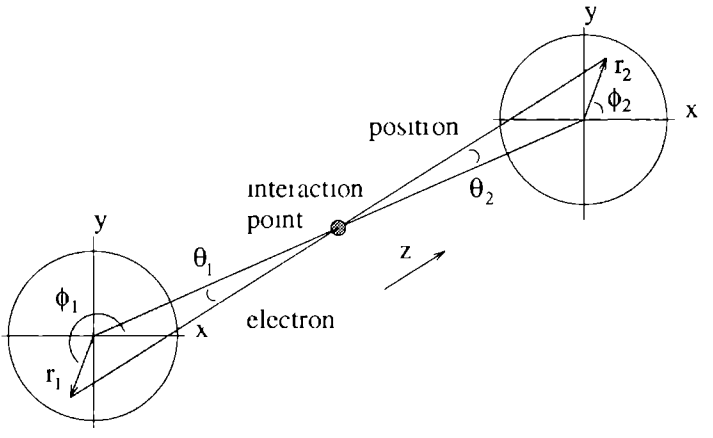

Figure 6.1: *The signature of a non radiative Bhabha event*

2 **Coplanarity.**

$$| \ 180^\circ - \Delta\phi \ | < 10 \tag{6 3}$$

where $\Delta\phi$ the angle between the azimuthal angles ϕ_1 and ϕ_2 expresses the coplanarity of the event

In addition a fiducial volume is defined only particles with impact points inside the boundaries of this volume are accepted To make use of the fact that the tracker consists of four r measuring layers the fiducial volume cut is applied at each layer individually, thus obtaining four event samples Accepted are the events satisfying a *tight* cut on one side and a *loose* cut at the opposite side

3 **Tight fiducial volume.**

$$\begin{aligned} 85 \text{ mm} \ < \ r \ < \ 145 \text{ mm} \\ | \ \phi - 90^\circ \ | \ > \ 11\ 25^\circ \\ | \ \phi \ \ 270^\circ \ | \ > \ 11\ 25^\circ \end{aligned} \tag{6 4}$$

4 **Loose fiducial volume.**

$$76 \text{ mm} < r < 184 \text{ mm} \tag{6 5}$$

The selection criteria are chosen in such a way that the purity of the sample is large while the acceptance of events remains sufficiently large as well In the following sections the selection criteria are further motivated and the resulting event samples for data and Monte Carlo are presented

Energy

The asymmetric energy requirement serves to select Bhabha events including those where part of the energy is lost Due to the radiation of a photon (see chapter 7) energy can escape along the

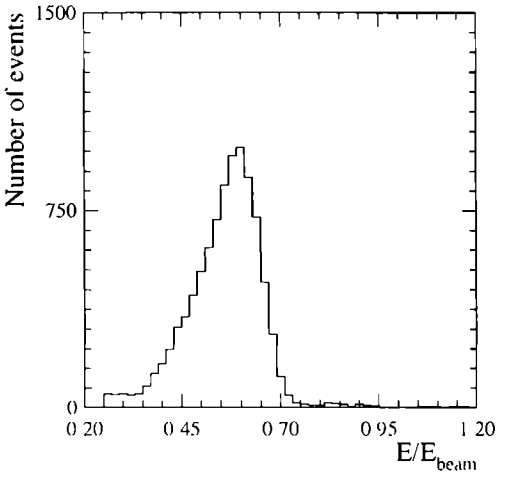

Figure 6.2: *The energy distribution of background events.*

beampipe. Events with an imperfect energy reconstruction, due to a not well functioning crystal, are retained in the sample as well.

Background events in the luminosity monitors are due to collisions of the electron (positron) beams with remaining atoms inside the beam pipe and the resulting off momentum particles. The collisions take place outside the interaction regions and upto a certain energy loss they still pass the quadrupole magnets. The interaction of the beams with remaining particles inside the beampipe due to a limited quality of the vacuum is not included in the Monte Carlo simulations and therefore these events need to be rejected.

Taking the configuration of the bending magnets and the quadrupoles into account the energy distribution of these events can be predicted. The distribution is broad and centred around half the beam energy [39]. If the data sample is studied where all Bhabha events are specifically removed, the observed energy distribution is as shown in figure 6.2. This is in a reasonable agreement with the predicted spectrum.

Due to the trigger requiring an energy deposit on both sides of the interaction point these events are only recorded if a coincidence occurs between a combination of a background and a Bhabha event or two background events. In figure 6.3 (left) it can be seen how the majority of these background events are removed from the data sample. The remaining background is examined after the coplanarity requirement is applied. This is discussed in 6.2.2.

The energy distribution of the final selected Bhabha event sample is shown in figure 6.3 (right) for both Monte Carlo and data. For each event the average energy is, $(E_1 + E_2)/2$, is plotted. The events shown in this distribution satisfy all selection criteria. The agreement between the data and Monte Carlo sample is good. At energies larger than the beam energy a slight enhancement in the data is observed. These are real Bhabha events recorded with a simultaneous 'background' event.

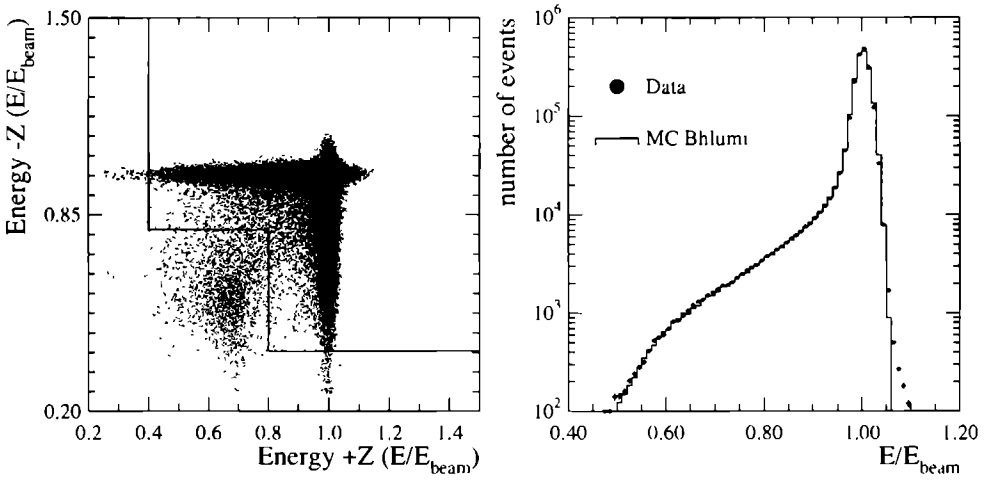

Figure 6.3: *The correlation between the observed energies in the BGO on both sides of the interaction point (left). The energy requirement is indicated with a solid line. Using this cut the random beam-gas interactions are removed from the event sample. In the right plot the energy distribution of the Bhabha events.*

Coplanarity

For each event the azimuthal angle between the ϕ-coordinates of the impact points on $-z$ and $+z$ is calculated.

This angle has to be corrected for the influence of the magnetic field inside the L3 detector and misalignments between the two detector sides. The magnetic field, B, in the detector is approximately 0.5 Tesla. Due to their opposite charge, the electron and the positron are always deflected in the same direction since they are emitted back-to-back. This effect is schematically drawn in figure 6.4. Therefore a small shift in the average value of $\Delta\phi$ is observed. The size of this shift is estimated using the following equation

$$180 - (\Delta\phi) = \frac{6Br^2}{20p \cdot r \sin\theta} \approx \frac{6Bz}{20p} \tag{6.6}$$

with $r \approx z \sin\theta$. Using the magnetic field B = 0.5 Tesla, the momentum p = 45 GeV and z = 2.65 m this equals 0.5°. The expected value of $\Delta\phi$ is therefore 179.5°. The value for $\Delta\phi$ can be directly fitted from the reconstructed Bhabha events. In the data an angle of 179.14° is found, for the Monte Carlo the angle is 179.63°. The difference between the data and Monte Carlo is due to a small relative rotation of the two detectors in the azimuthal direction. The coplanarity distribution of the Bhabha events as a function of the coplanarity is shown in figure 6.4 for both Monte Carlo and data. The selection cuts are indicated with arrows. The events shown in this sample satisfy all the selection criteria except the coplanarity requirement. No significant deviation between the data and the Monte Carlo is observed.

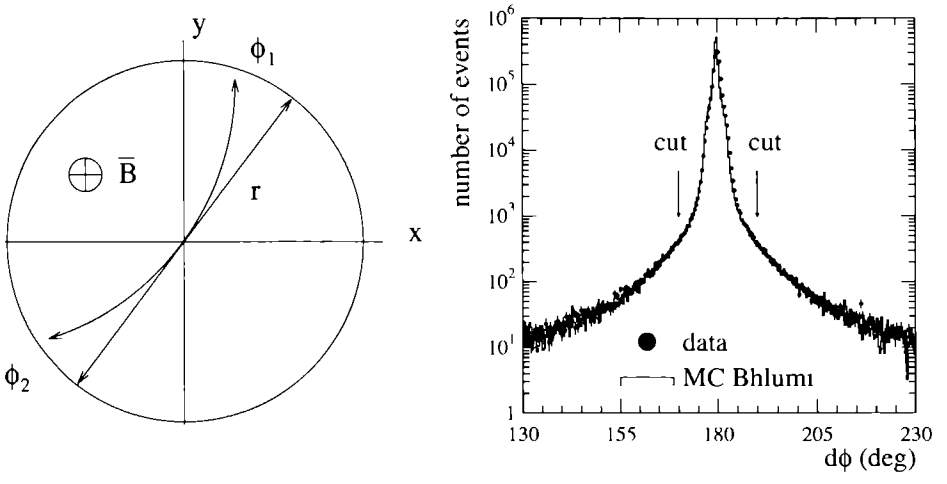

Figure 6.4: *The effect of the B-field (left) The coplanarity of the Bhabha events (right) The broadening of the distribution near the peak is explained by the fact that ϕ is expressed in discrete strip coordinates*

Fiducial Volume

For each silicon layer the Bhabha events inside the tight fiducial volume are accepted if at the same time the particle at the opposite side is within the loose fiducial volume Four samples are obtained which are averaged using the visible cross section determined for each layer separately

$$\mathcal{L} = \frac{1}{4} \sum_{i=1}^{4} \frac{N^i_{\text{Bhabha}}}{\sigma^i_{\text{vis}}} \tag{6 7}$$

where the index i indicates the layer number as follows

$i = 1$	$-z$, inner layer	$i = 3$	$+z$, inner layer
$i = 2$	$-z$, outer layer	$i = 4$	$+z$, outer layer

The visible cross section is discussed in section 6.3.

The *tight-loose* selection strongly reduces the sensitivity for offsets of the beam position with respect to the centre of the detector. This can be seen in figure 6 5 where the relative change in the luminosity is shown as a function of the size of an offset of one of the two detectors with respect to the nominal beam position. Both the *tight-loose* and the *tight-tight* based selection are compared with the nominal luminosity normalised to 1 in this plot. In the left plot the displacement is in the xy-plane, in the right plot the vertex is displaced with respect to the centre of the two detectors in the z direction.

The boundaries of the *tight* fiducial volume are well away from the regions where alignment pins are located As was shown in the previous chapter these alignment pins enhanced the hit

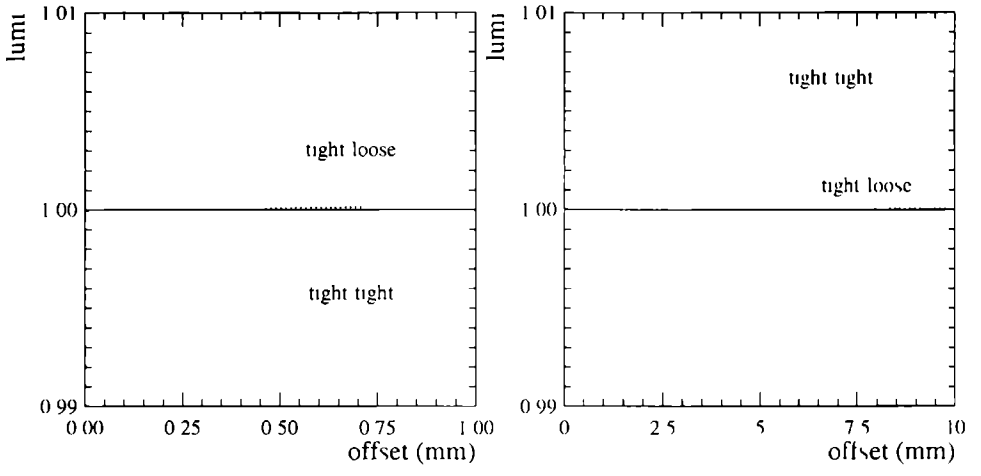

Figure 6.5: *The effect of the* tight-loose *based selection for an offset of the vertex in the xy-plane (left) or in the z direction*

multiplicity locally (see section 5 4 2) In the azimuthal range the small gap in the BGO due to the opening mechanism leads the exclusion of a region of 2 times 11 25 ° This corresponds to one crystal on each side of the gap

For the *loose* cut the reconstructed impact point in the BGO is used The *loose* cut is needed to reject events with a false energy reconstruction In case a scattered particle enters the calorimeter so close to the boundary that only a small part of its energy is contained inside the BGO, the energy reconstruction can fail The *loose* cut is set half a crystal away from the BGO boundary to avoid this effect

In figure 6 6 the distributions for both Monte Carlo and data events as a function of the r co ordinate are shown The distribution is shown for the two inner layers of the detectors on $-z$ and $+z$ In these plots the r coordinates are smeared over the width of the strips, the selection of the events is always in terms of discrete strip numbers

When the plots are carefully examined the influence of the conical flange in the beam pipe on the positive side of the interaction point is visible In the region 110 mm $< r <$ 130 mm a distortion is observed which is not exactly at the same location in data and Monte Carlo This distortion is caused by the edges of the flange and the difference is explained by small offsets between the detector location in data and Monte Carlo The fact that the detector is not at the same z position in the simulation means that the projection of the flange in the beam pipe is not exactly at the same r position ($r = z \tan\theta$) on the detector However the agreement in the region where the fiducial volume cut is made is good To stress the quality of the agreement between data and simulation the inserts show an enlarged view on a linear scale of the area around the fiducial volume boundaries

Intermezzo

In defining the fiducial volume one can use either polar coordinates (θ and ϕ) or cylindrical ones ($r = z \tan\theta$ and ϕ) Although at first glance the difference might seem to be a purely mathematical transformation it leads to a more fundamentally different approach in the data treatment at further examination

If the boundaries of the fiducial volume are expressed in terms of θ_{min} (inner boundary) and θ_{max} (outer boundary) the actual location of the boundary on the silicon sensor depends on its position on the z axis Therefore the boundary on the back and the front side of the Stesalit layers, as well as on the two different r-measuring layers, is at a different strip number

The difference between the cut position on the first and the second layer, for a typical value of $\theta_{min} = 32$ mrad is approximately 3 mm which corresponds to a difference of 6 strips A comparable difference exists between the data and the Monte Carlo events since the detector position on the z axis is not exactly equal in those two samples

If however, the fiducial volume is expressed in terms of r_{min} and r_{max} one can precisely determine the corresponding strip numbers of these radii These numbers are now equal for all sensors, independent of their z positions, both for data and Monte Carlo events

As a result all detector effects can be taken into account Known dead strips and strips not used in the data sample due to excessive noise levels are removed from the Monte Carlo sample as well

The use of the track coordinates expressed in r therefore allows a precise determination of the detector acceptance

Although at the $-z$-side the agreement between data and simulation might look better at first glance there is an enhancement in the data in the number of events at small values of r This is due to particles which shower before they reach the detector Only part of the shower is detected in the silicon detector and the assigned impact point can be systematically shifted to a higher value of r Since the amount of material is slightly underestimated in the Monte Carlo (see section 5 4 2) this could cause a small overshoot in the data at this point

6.2.2 Background subtraction

After the selection criteria have been applied the remaining number of background events is estimated from the coplanarity distribution The background events caused by beam gas collisions are assumed to have a homogeneous $\Delta\phi$ distribution Another source of background events is formed by two photon collisions, $e^+e^- \rightarrow e^+e^-X$ with two tags in the luminosity monitors Also these events have no preference for coplanarity

In a ϕ window located 10 degrees away from the coplanarity peak see again figure 6 4 (right), the number of events in data and Monte Carlo are compared To reduce the influence of radiative events in this study an extra energy requirement is imposed, only events with energy deposits on both sides more than 5% away from E_{beam} are considered

The enhancement of the data is studied in two windows, one on each side of the peak The resulting distribution of the background events is shown in figure 6 7 For this plot the Monte Carlo events are subtracted from the number of events in the data sample Due to statistical fluctuations the resulting distribution is at some points below zero As the background is assumed to be homogeneous the integrated number of events in this region is subtracted from the final Bhabha sample The total amount of background events is 0 003 % of the total sample and the error is therefore assumed to negligible

6.2.3 Trigger efficiency

The trigger inefficiency is examined with the selection of Bhabha events which are triggered by the single tag trigger only (see chapter 5 equation 5 1) For 1993 no significant trigger inefficiency has been measured and the systematic uncertainty on the luminosity determination is assumed to be negligible

The total, background subtracted, number of events found in the data is given in table 6 1 Since the layers are at different z positions the acceptance is quite different During the 1993 run two major access periods occurred, the data is divided in three samples (A, B, and C) separated by these periods

6.3 The visible cross section

6.3.1 Acceptance

The visible cross section is defined as

$$\sigma^{\prime}_{\text{visible}} = \sigma(s)_{\text{Bhlumi}} \frac{N^{\prime}_{\text{acc}}}{N_{\text{gen}}} \mathcal{F}^{\prime}_{\text{geom}} \tag{6 8}$$

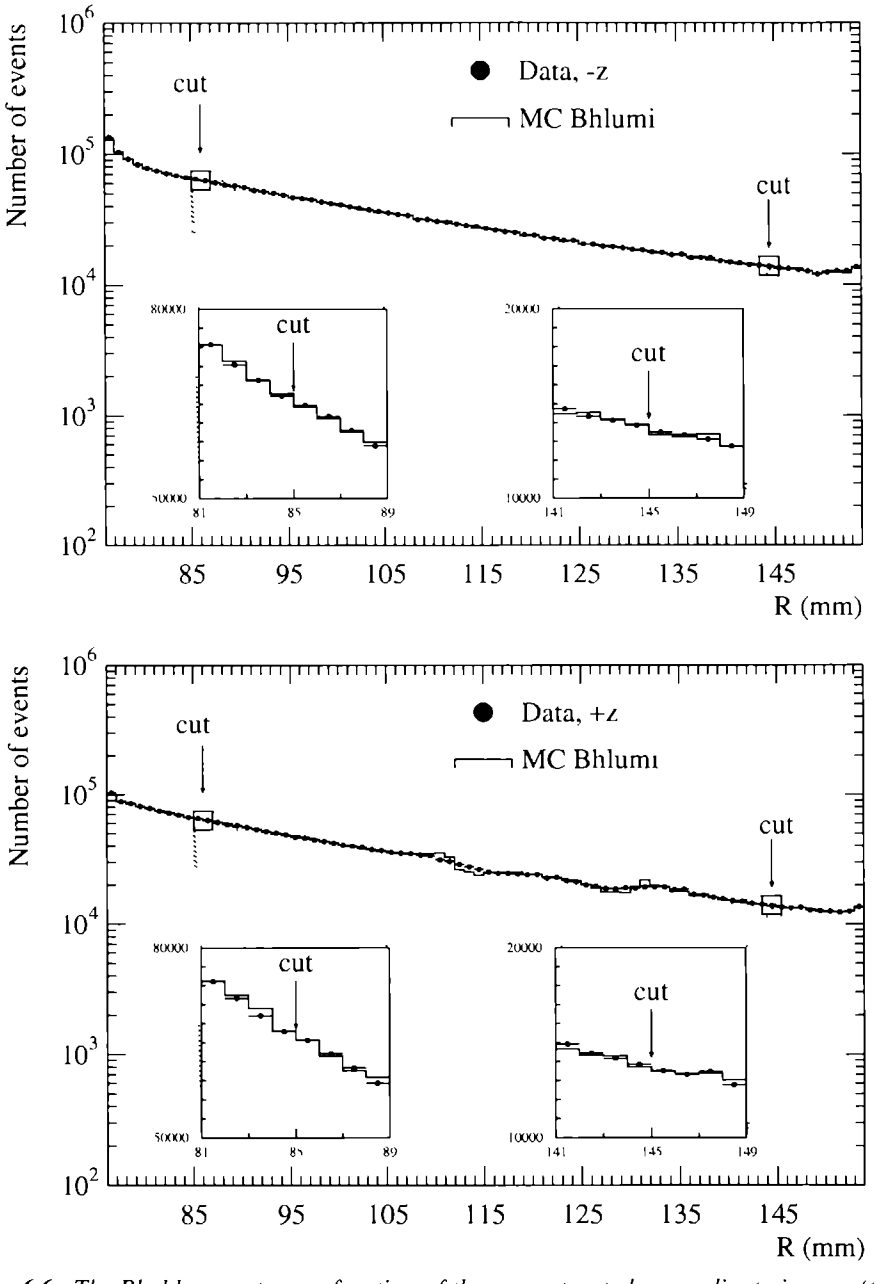

Figure 6.6: *The Bhabha events as a function of the reconstructed r-coordinate in mm, (top −z, bottom +z) both on a logarithmic scale and a linear scale in the inserts*

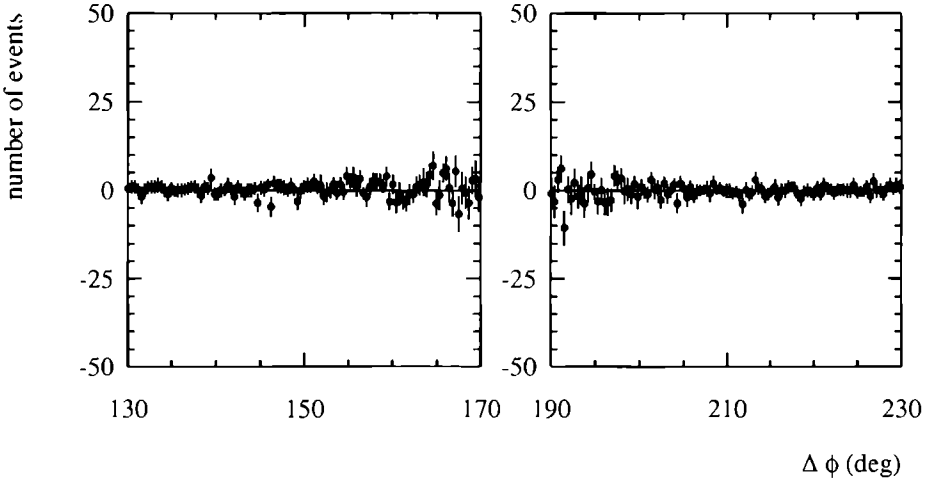

Figure 6.7: *The background events as a function of their coplanarity. In total 80 background events are subtracted from the data sample.*

	1993 A	1993 B	1993 C
layer 1	402500	1196273	675864
layer 2	426158	1267899	716713
layer 3	404253	1201656	678436
layer 4	428599	1274746	719743

Table 6.1: *The number of selected events for the three run periods in 1993*

The theoretical cross section, σ_{Bhlumi}, has been discussed in chapter one. The second factor represents a first approximation of the detector acceptance, with N_{acc} and N_{gen} respectively the accepted Monte Carlo events and the number of generated events. The sample of Monte Carlo events has been generated such that the electron (positron) is scattered in a polar range from 20 mrad $< \theta <$ 200 mrad. From a total of 4.1 million generated events only 0.9 million events pass the fiducial volume cuts (table 6.2). The limited number of Monte Carlo events introduces an error on the acceptance determination. The limitation is due to the fact that an accurate simulation of the detector response to a generated event is very (CPU) time consuming. The resulting contribution to the uncertainty in the visible cross section, $\Delta\sigma_{\text{vis}}^{\text{stat}}$, is 0.09 %.

$N_{\text{gen}} = 4114187$		
	N_{acc}	$N_{\text{acc}}/N_{\text{gen}}$
layer 1	874295	0.2125
layer 2	928526	0.2356
layer 3	873641	0.2123
layer 4	929206	0.2258

Table 6.2: *The number of generated and accepted Monte Carlo events*

The factor $\mathcal{F}_{\text{geom}}$ is a correction to the acceptance for the existing differences between the real detector geometry and its description in the Monte Carlo. It is split in four geometry corrections, all separately calculated for each r-measuring layer, i:

$$\mathcal{F}^i_{\text{geom}} = \mathcal{F}^i_{\text{sens}} \cdot \mathcal{F}^i_{\text{beam}} \cdot \mathcal{F}^i_{\text{vert}} \cdot \mathcal{F}^i_{\text{temp}} \tag{6.9}$$

1. $\mathcal{F}^i_{\text{sens}}$: Correction for small displacements of the silicon sensors on the support structure.

2. $\mathcal{F}^i_{\text{beam}}$: Correction for the offset of the beam with respect to the centre of the detector in the xy-plane.

3. $\mathcal{F}^i_{\text{vert}}$: Correction for the offset of the vertex position in the z-direction.

4. $\mathcal{F}^i_{\text{temp}}$: Correction for the expansion of the detector due to an operating temperature which was higher than anticipated.

The numerical values of these factors, either extracted from the data or from external measurements, are presented in the following sections.

6.3.2 Position of the sensors on the support, $\mathcal{F}_{\text{sens}}$

Using the optical survey measurements described in chapter 4 (see section 4.2) the real location of the sensors on the support structure has been obtained. The offset of the measured position of the inner boundary with respect to the design value is summarised in table 6.3 together with the resulting correction factor. The overall uncertainty on the survey measurements is 6 μm, the corresponding uncertainty in the correction factor is 0.00017.

	offset (μm)	$\mathcal{F}_{sens}$
layer 1	20	0.99940
layer 2	31	0 99914
layer 3	28	0.99920
layer 4	12	0 99966

Table 6.3: *The correction factor $\mathcal{F}_{sens}$, for the difference of the sensor locations with respect to the design geometry.*

6.3.3 Beam offset in the xy-plane, $\mathcal{F}_{beam}$

The LEP beam does not run exactly through the centre of the silicon tracker. Due to the $1/\theta^3$ dependence of the Bhabha cross section this results in a non-uniform distribution of the selected events over the azimuthal angle, as this angle is defined in local detector coordinates For example, an offset of the beam in the positive x-direction results in an enhancement of the number of Bhabha events selected in a small segment around $\phi = 0°$ The offset of the detector is schematically shown in figure 6.8.

The offsets of the beam can be derived from the density distribution in the data sample, using the first order Bhabha cross section

$$\frac{d\sigma}{d\phi} = \frac{Cd\theta}{\theta^3} \approx \frac{Cz^2 rdr}{r^4} \tag{6.10}$$

in a perfect geometry and with C as a constant. In terms of the coordinates measured in the displaced detector frame, r' and ϕ', this is

$$\frac{d\sigma}{d\phi'} = C \cdot \frac{z^2 r' dr'}{((x' + \Delta x)^2 + (y' + \Delta y)^2)^2} \tag{6 11}$$

Neglecting all higher order terms of Δx and Δy this leads to

$$\frac{d\sigma}{d\phi'} = C \cdot \frac{z^2 r' dr'}{(r'^2 + 2\Delta x r' \cos\phi' + 2\Delta y r' \sin\phi')^2} \tag{6.12}$$

Integrating the differential cross section over a region from r_{min} to r_{max}, the number of selected Bhabha events versus the measured azimuthal angle, is expressed as

$$N(\phi') = N_{average} + A\cos\phi' + B\sin\phi' \tag{6.13}$$

where N is the number of selected events and A and B are related to the offsets Δx and Δy according to

$$\Delta x = \frac{3}{8} \cdot \frac{A}{N_{average}} \cdot \frac{(r_{min}^{-2} - r_{max}^{-2})}{(r_{min}^{-3} - r_{max}^{-3})} \qquad \Delta y = \frac{3}{8} \frac{B}{N_{average}} \cdot \frac{(r_{min}^{-2} - r_{max}^{-2})}{(r_{min}^{-3} - r_{max}^{-3})} \tag{6 14}$$

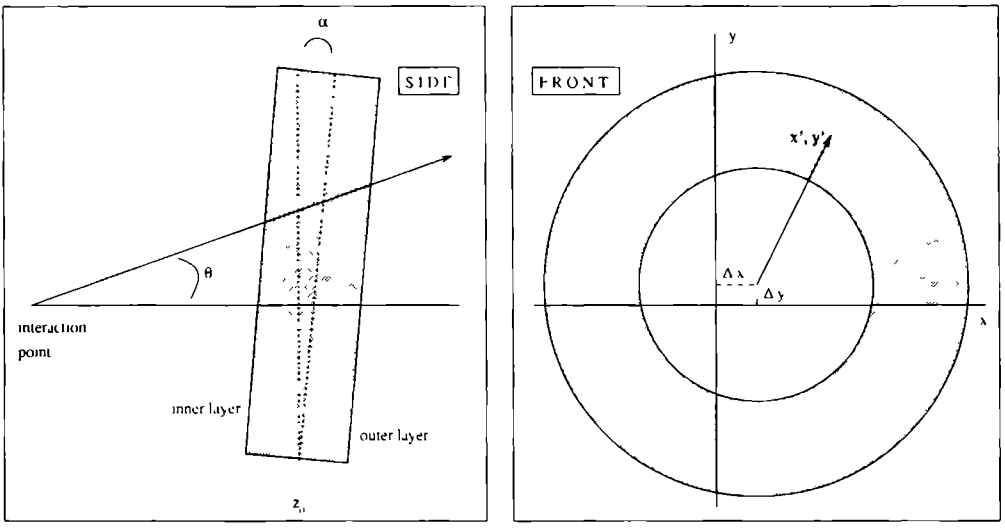

Figure 6.8: *The silicon detector with an offset with respect to the nominal beam position. On the left plot the effect of a rotation around the x axis, on the right plot the effect of an offset in the x,y plane.*

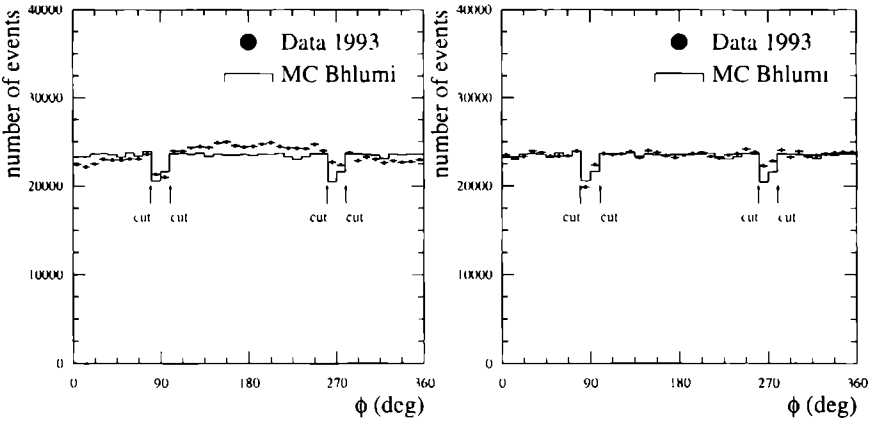

Figure 6.9: *The number of selected Bhabha events as a function of the azimuthal angle, on the left plot the offsets are not implemented on the right plot they are.*

The offsets are fitted from the real data The uncorrected data is shown in figure 6 9 (left) where the deviation with the Monte Carlo distribution is clearly visible After the geometry corrections have been implemented the agreement between data and Monte Carlo is good, see figure 6 9 (right) In table 6 4 the offsets and the corresponding factors are presented The accuracy of the fitted offsets is in the order of 0 1 mm which has a negligible effect on the uncertainty in the visible cross section The error on the fit result is estimated by studying the offset for different subsets of the data samples If the same fit procedure is applied to the Monte Carlo events the resulting offsets are found to be compatible with zero

	$\sqrt{\Delta x^2 + \Delta y^2}$ (mm)			$\mathcal{F}_{\text{beam}}$		
	1993 A	1993 B	1993 C	1993 A	1993 B	1993 C
layer 1	0 83	0 95	1 16	1 00027	1 00035	1 00059
layer 2	1 20	1 40	1 54	1 00070	1 00077	1 00082
layer 3	1 87	2 62	2 13	1 00125	1 00252	1 00183
layer 4	1 67	2 32	2 05	1 00105	1 00186	1 00144

Table 6.4: *The scale factor $\mathcal{F}_{\text{beam}}$ resulting from the offset between the centre of the detector and the beam line The error on the offsets is 0 1 mm*

6.3.4 Distance to the vertex, $\mathcal{F}_{\text{vert}}$

To determine the luminosity per layer the distance from the vertex to each layer must be determined In the Monte Carlo the inner layer is located at z = 2612 45 mm and the outer layer at z = 2692 45 mm on both sides of the interaction point In the data the detector is not exactly at the nominal position, the vertex is not necessarily in the centre of the global L3 coordinate system and in addition it has been noted that the detector was slightly tilted with respect to the xy-plane These three effects are taken into account separately

LEP survey

The detector position in global L3 coordinates is obtained from survey measurements The intrinsic accuracy of these measurements is 0 3 mm Four survey bars had been designed to be attached to brass blocks, fixed at each support layer of the detector, when it was surveyed The design of the survey bars is shown in figure 6 10 Problems with the fixation of the brass blocks complicated the interpretation of the survey measurements Moreover the detector had been tightened only at the foot which resulted in a small tilt in the vertical position due to the the weight of the cables The total systematic uncertainty on the distance between the two detectors on both sides of the interaction point is estimated to be 1 6 mm, which is the quadratic sum of the uncertainty of the detector positions on both sides of the interaction point of 1 1 mm The distance between the inner and the outer layers is measured to be 79 6 $\pm$ 0 2 mm The survey results extrapolated to the position of the foot of the detector are given in table 6 5

The fixation of the detector has been improved before the detector was installed for the 1994 run An aluminium support plate has been designed which is fixed to both the foot plate and the

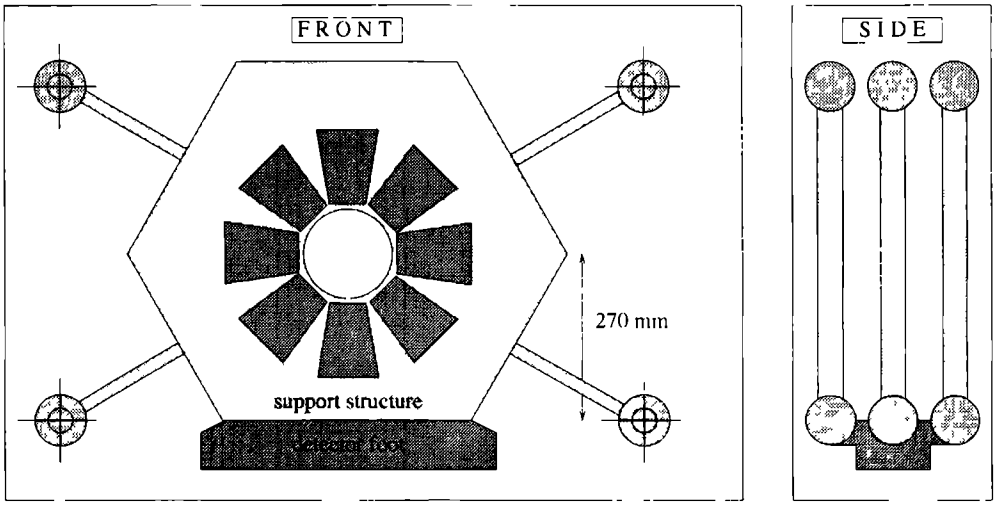

Figure 6.10: *The survey marks used to determine the position of the detector in the L3 global coordinate system.*

z-position (mm)			
layer 1	-2606.14	layer 3	2612.62
layer 2	-2685.78	layer 4	2692.16

Table 6.5: *The z position obtained from survey measurements. The errors on these numbers are 1.1 mm*

support structure of the detector The intrinsic survey precision of 300 μm is obtained for the 1994 run.

Rotation around the x and y axes

Since the LEP survey measurement only provides the z-coordinate at the foot of the detector a correction has to be applied, due to the tilt of the detector with respect to the xy-plane This rotation is determined, using Bhabha tracks from the data sample. The rotation of the detector has been sketched in figure 6.8.

The measured difference in the coordinate between the inner and outer layer is used to calculate the rotation angle, α For the determination of the angle α the coordinates are expressed as

$$\begin{aligned} \theta_{\text{inner}} &= \arctan(r_{\text{inner}}/z_{\text{inner}}) \\ \theta_{\text{outer}} &= \arctan(r_{\text{outer}}/z_{\text{outer}}) \end{aligned} \tag{6.15}$$

The effect of a rotation is to first order determined by a relative offset of the centre of the inner and the outer layer. The observed curves for both detector sides are shown in figure 6.11 as a function of the azimuthal angle. The distribution is to first order given by the equation

$$\theta_{\text{inner}} - \theta_{\text{outer}} = A + B\cos\phi + C\sin\phi \tag{6.16}$$

The constants B and C indicate rotations around the y and x axes respectively. In the data the effect of the rotation around the y-axis is negligible, the rotation around the x-axis is given by

$$\alpha_x = C \cdot \frac{(z_{\text{inner}} + z_{\text{outer}})}{2(z_{\text{inner}} - z_{\text{outer}})} \tag{6.17}$$

The rotation angles around the x-axis are used to extrapolate the survey measurements, which only provided the position of the detector foot, to the centre of the detector. The resulting position of the centre is used as the average position of the detector on the z-axis The precision of the fit is estimated to be 0.2 mrad. The angle α_x and the corresponding corrections to the z-positions at the centre of the detector are given in table 6 6 The difference in the angle between periods B and C is explained by the fact that the detector has been recabled after period B The weight of the cables slightly changed the tilt of the detector.

	1993 A+ B		1993 C	
	α (mrad)	offset (mm)	α (mrad)	offset (mm)
$-z$	12.1	3.3	12.0	3.2
$+z$	8.1	2.4	3.1	0.8

Table 6.6: *Results of the fitted rotation angles and the corresponding corrections to the distance from the vertex to the detector along the z-axis The accuracy in the angles is 0 2 mrad, in the offsets 0 1 mm*

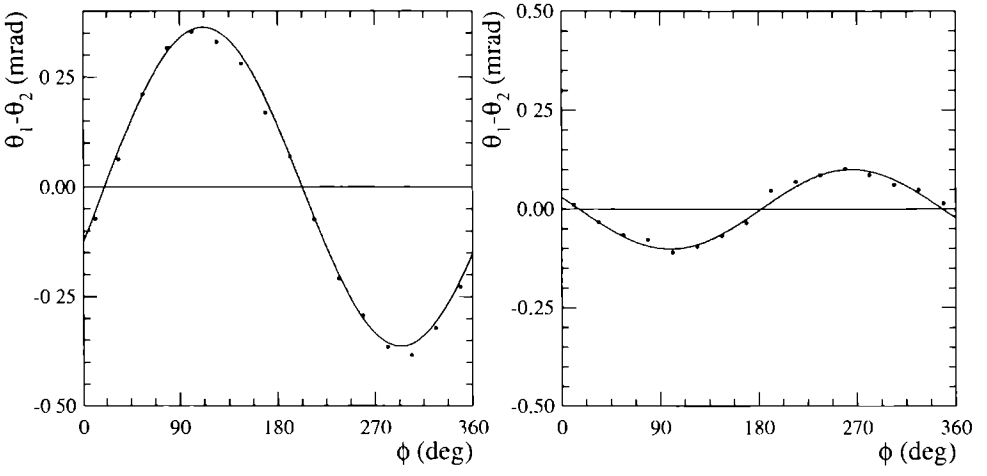

Figure 6.11: *The difference of θ_1 and θ_2 as a function of the azimuthal angle, on both sides of the interaction point. (left $-z$, right $+z$). The fit is drawn with a solid line.*

Vertex position

So far the z-positions of the detector have been expressed in global L3 coordinates. To obtain the luminosity per layer however, the distance from the detector to the actual vertex position is of interest. Therefore the vertex position with respect to the origin of the L3 frame must be determined. Using the notations defined in figure 6.12 the vertex position, z_{vertex}, can be expressed as

$$\begin{aligned} z_{centre} &= (z_1 + z_2)/2 \\ \Delta z &= z_{centre} \cdot \frac{r_2 - r_1}{r_1 + r_2} \\ z_{vertex} &= z_{centre} + \Delta z \end{aligned} \tag{6.18}$$

where Δz is determined from a sample of back-to-back Bhabha events and a Gaussian fit is performed to determine the mean of the distribution. The results are shown for run period C in figure 6.13. The fitted value of $\Delta z = -2.7 \pm 0.2$ mm, corresponds to $z_{vertex} = -0.1 \pm 0.2$ mm. Combining the fits for periods A, B and C the average value of z_{vertex} is found to be -0.25 ± 0.2 mm.

The total distance from each layer to the actual vertex is given in table 6.7 together with the corresponding correction factor to the visible cross section. These numbers are the combined results of the surveyed position (table 6.5), the offset due to the rotation of the detector (table 6.6) and the vertex position. The error on the individual distances is 1.1 mm corresponding to an error on $\mathcal{F}_{vert}$ of 0.0008.

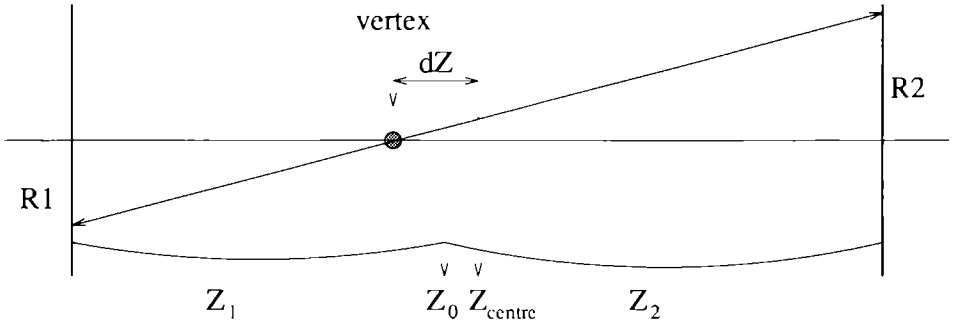

Figure 6.12: *Definition of the quantities relevant for the calculation of the position of the vertex in the z direction, z_0 is the origin of the L3 frame.*

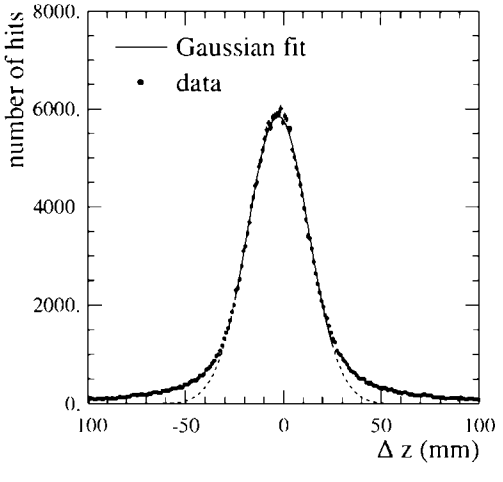

Figure 6.13: *Vertex displacement for the data of period C. The Gaussian fit gives an average displacement of Δz = -2.7 ± 0.2 mm.*

	1993 A+B		1993 C	
	z (mm)	$\mathcal{F}_{\text{vert}}$	z (mm)	$\mathcal{F}_{\text{vert}}$
layer 1	2609.2	1.0054	2609.2	1.0053
layer 2	2688.8	1.0049	2689.0	1.0049
layer 3	2615.2	1.0100	2613.7	1.0088
layer 4	2694.7	1.0093	2693.2	1.0082

Table 6.7: *The final position with respect to the vertex with the corresponding acceptance correction* $\mathcal{F}_{\text{vert}}$

6.3.5 Temperature correction, $\mathcal{F}_{\text{temp}}$

All detector design specifications are specified at a temperature of 20 °C. Also the optical survey measurements have been performed in an environment of 20 °C. However, the operating temperature in the pit was 33 ± 5 °C. To take the resulting expansion of the detector into account the expansion of a spare layer has been studied at NIKHEF while it was heated it from 20 °C to 35 °C. Using the optical survey bench the expansion coefficient has thus been measured to be 15 ± 4 ppm/K. These measurements are in agreement with the temperature expansion coefficient of Stesalit which is 11.5 ppm/K. The expansion is calculated at the point where the silicon sensor is pushed to the alignment pin which is attached to the Stesalit. The expansion with respect to the design value of $r = 75.000$ mm is 15 ± 4 μm for the temperature observed in the L3 pit.

The maximal total expansion of the silicon sensor itself is 3 μm. Since it is not clear how this extrapolates from the inside edge to the boundaries this is taken as a worst case estimate for the uncertainty in the boundary position.

Combining the uncertainties in the temperature (with ± 5 °C corresponding to ± 5 μm), the uncertainty in the expansion coefficient (with ± 4 ppm corresponding to ± 4 μm) and the uncertainty in the expansion of the silicon itself the total error on fiducial volume boundary due to the expansion is estimated to be $5 \oplus 4 \oplus 3 = 7$ μm. The correction factor for the visible cross section is the same for all layers and is $\mathcal{F}_{\text{temp}} = 0.99957 \pm 0.00020$.

6.3.6 Total visible cross section

The total geometry factor is used to calculate the visible cross section for each layer. The visible cross section at $\sqrt{s} = 91.25$ GeV is given in table 6.8 together with the total geometry correction factor $\mathcal{F}_{\text{geom}}$, for each run period.

As was shown in chapter 1 (see equation 1.17) the generated cross section is to be corrected with a factor $\mathcal{F}_{\gamma\gamma}$. $\mathcal{F}_{s/s'}$ depending on the centre of mass energy, $\sqrt{s'}$. For a point with a centre of mass energy of $\sqrt{s'}$ the factor $\mathcal{F}_{s/s'}$ is in the Born approximation equal to s/s'. The product of both corrections factors are given in table 6.9.

With the numbers from these two tables the exact visible cross section can be calculated for each LEP run period.

$\sigma(s)$	N_{acc}/N_{gen}	$\mathcal{F}_{geom}$		
layer 1	68981 34	1.004752	1.004832	1 005033
layer 2	72930.51	1.004459	1.004530	1.004580
layer 3	68843.89	1.010140	1.011427	1 009533
layer 4	72862 33	1.009763	1.010574	1.009000

Table 6.8: *The visible cross section at a centre of mass energy of 91 25 GeV with the correction factors for each period*

$\sqrt{s}$	$\mathcal{F}_{s/s'}$ $\mathcal{F}_{\gamma-Z}$
89 45	1.04100
91.21	1 00131
93 03	0.96238

Table 6.9: *Cross section correction for the three centre of mass energy points at which the LEP machine has been operated in 1993*

6.4 Luminosity

Combining all the numbers of the previous paragraphs the integrated luminosity, averaged over the four layers, can now be obtained. To make use of the luminosity in analyses of other event topologies the luminosity is calculated per run and stored in a database together with the LEP information on the beam energy

The following numbers are integrated over all 1993 runs, seperately for each energy point. The centre of mass energy is obtained from the LEP energy calibration and is split in three points. The 'peak'($\sqrt{s} = 91$ GeV) and two off peak points, 'peak −2' and 'peak +2' (respectively $\sqrt{s} = 89$ GeV and $\sqrt{s} = 93$ GeV). The number of events and corresponding luminosities are given in table 6 10

Bhabha events			
	peak -2	peak	peak +2
layer 1	610959	1070587	584600
layer 2	644892	1129386	617168
layer 3	613067	1074894	586108
layer 4	647465	1135167	618625
Integrated luminosity (1/pb)			
	8.46	15 41	8.75

Table 6.10: *The integrated luminosity for 1993.*

The total integrated luminosity recorded at the L3 experiment in 1993 is

$$\mathcal{L} = 32\,62 \pm 0\,02(\text{stat}) \pm 0\,07(\text{sys})$$

The systematic error is discussed in the following section

6.4.1 Systematic uncertainties

Event selection

After all the corrections of the detector geometry, small differences between the data and Monte Carlo sample still remain The uncertainty, introduced by the application of the selection cuts, is estimated by variation of the cuts around their central value and examining the resulting change in the luminosity The effects of these type of variations are shown in figure 6 14 If variation of the cut over a realistic range shows a systematic change in the luminosity a systematic error is assigned If the systematic error appears to be smaller than the statistical errors and the variation steps cannot be made smaller a worst case estimate of the error is made This estimate, which is actually the maximum sensibility for systematic effects, corresponds to the size of the statistical error on two neighbouring points in the variation plot Calculation of this statistical error is based on the absolute difference in the number of events between the sample at the central value and the sample at the value under study Therefore each point can only be compared with the point at the nominal value of the cut parameter The total error on the event selection, with the individual contributions added in quadrature, is 0 04% (table 6 11)

source	uncertainty (%)
inner boundary	0 020
outer boundary	0 010
min energy	0 020
max energy	0 010
gap-cut	0 020
coplanarity	0 020
Total selection	0 042

Table 6.11: *Systematic uncertainties in the event selection The individual errors are summed in quadrature*

Geometry

The uncertainties in the geometry are summarised in table 6 12 Although the beam position is only known to a precision of 100 μm this has no effect on the luminosity due to the *tight loose* requirement The relatively large error in the total z-distance is caused by problems with the attachment of the survey rods in combination with a rigidity problem of the fixation of the detectors at the foot

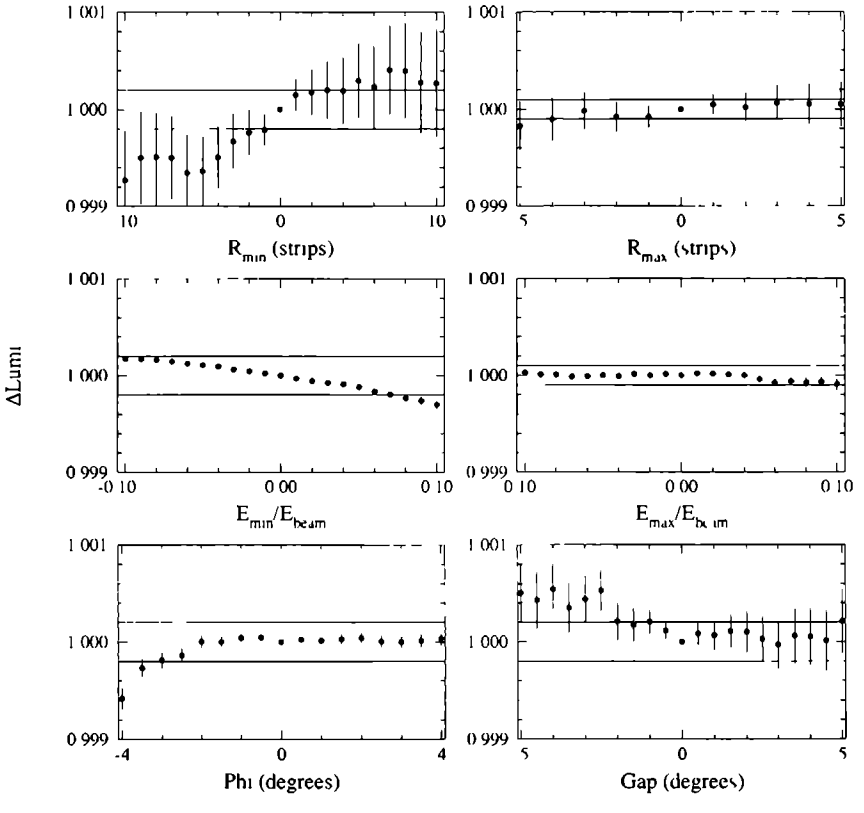

Figure 6.14: *The relative change in luminosity as a function of the variation of the selection criteria.*

source	uncertainty	
survey sensors	6 μm	0 018 %
beam position	0 1 mm	Negligible
Z distance	1 6 mm	0 061 %
temperature effects	7 μm	0 020 %
total geometry		0 067 %

Table 6.12: *Systematic uncertainties in the detector geometry The individual errors are summed in quadrature*

Comparing four layers

A consistency check on the luminosity calculation is the comparison of the four samples In this comparison part of the systematic effects can be studied All systematic errors which are not correlated between the four samples can cause differences in the four curves An error in the z determination of the vertex explains the difference in the samples of $+z$ and $-z$ Differences between the inner and outer layer are to be expected from the error on the inner boundary The total systematic uncertainty is indicated with a solid line

Since the selected event samples are not identical for the inner and outer layer, a statistical error is to be expected as well Since the cut is on a fixed value of r the number of accepted events is larger for the outer layers As can be seen in table 6 1 in the outer layer approximately 2 4 million events are selected versus 2 2 in the inner layer For the Monte Carlo this difference is 0 8 million and 0 72 million This leads to a 0 042 % statistical error between the inner and outer layer

The four event samples are found to be consistent within the errors and therefore no additional error is assigned The overall systematic error on the 1993 luminosity is thus 0 08 % All uncertainties are summarised in table 6 13 A comparison is made with the analysis based on the BGO only The numbers for this analysis are the best results obtained in 1992 [16] Although more events have been generated since than the statistical uncertainty is not adjusted for the extra amount Monte Carlo events since it was not the dominating error

6.5 Lineshape

Using the luminosity calculation in the analysis of the the decay of the Z into a quark pair the cross section is determined at each of the centre of mass energies In figure 6 16 the cross section is shown and compared with the points obtained before 1993 A detailed description of the selection of the events of the type $Z \rightarrow q\bar{q}$ can be found in [40] From the fit the mass m_Z, and the decay width, Γ_Z of the Z boson are determined [41]

$$m_Z = 91190\,0 \pm 5\,4 \text{ MeV}$$
$$\Gamma_Z = 2504\,0 \pm 5\,8 \text{ MeV}$$

Using all the L3 data from 1990 through 1993 the number of light neutrino species can be determined from the mass of the Z boson and the decay widths of the Z into hadrons en leptons The number of neutrinos is $N_\nu = 2\,981 \pm 0\,031$ [42]

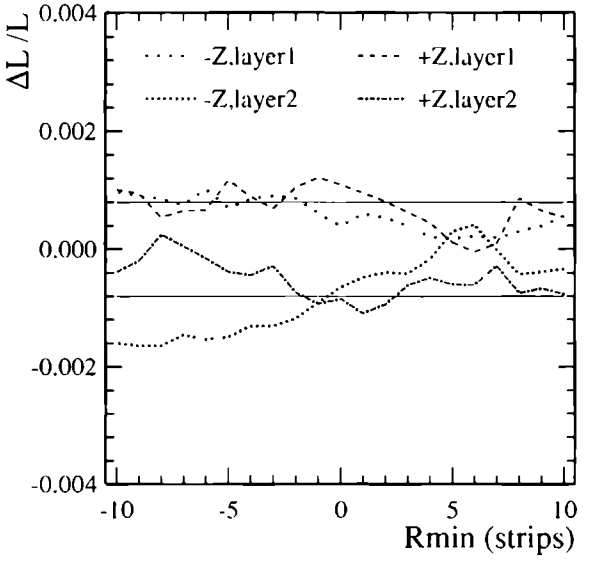

Figure 6.15: *The relative change in the luminosity as a function of the change in the inner boundary for all the four layers*

source	contribution to $\Delta\mathcal{L}/\mathcal{L}$ (%) BGO Analysis	contribution to $\Delta\mathcal{L}/\mathcal{L}$ (%) BGO+SLUM analysis
trigger	negligible	negligible
event selection	0.3	0.042
background subt.	negligible	negligible
geometry	0.4	0.067
total experimental	0.5	0.08
MC statistical	0.1	0.09
theory	0.25	0.16
total	0.6	0.20

Table 6.13: *Systematic uncertainties on the luminosity measurement. Before 1993 the luminosity measurement was performed with the use of the BGO detector alone*

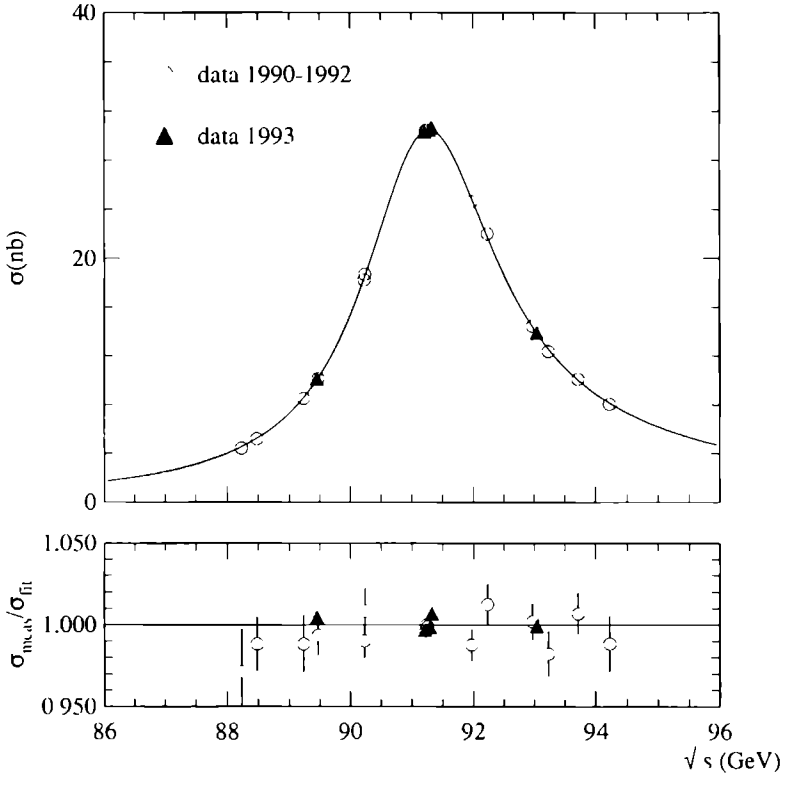

Figure 6.16: *The cross section of the decay of a Z boson into a quark pair The solid line is a fit to the data On the bottom plot the points are compared to the fit value.*

Chapter 7

Radiative Bhabha Events

7.1 Introduction

Radiative Bhabha events have, apart from the electron and the positron, a photon in the final state For a precise measurement of the luminosity these radiative effects are important Firstly, one of the largest contributions to the systematic uncertainty in the luminosity is due to incomplete modelling of higher order effects in the Monte Carlo event generator Secondly imperfections in the detector geometry have a profound effect on the selection of radiative events To investigate the modelling of radiative effects, two very different topologies of radiative Bhabha events are selected [1]

1 Bhabha events with in addition to the scattered electron and positron a photon observed in one or both of the BGO calorimeters This type of event is referred to as a 'final state' radiative event and is written as $e^+e \rightarrow e^+e\,\gamma$,

2 Bhabha events with in addition to the scattered electron and positron a photon(s) escaping along the beam direction This type of events is referred to as an 'initial state' radiative event and is written as $e^+e^- \rightarrow e^+e^-(\gamma)$,

In this chapter the event selection and the comparison between real and simulated data for these two event samples are discussed Both samples are obtained by the application of slightly modified cuts with respect to the standard Bhabha event selection cuts as discussed in the previous chapter

A generator study is made to estimate the amount of events to be expected, in section 7 2 In section 7 3 the final state events are presented followed by the initial state events in section 7 4

All energies are expressed in fractions of the beam energy The coordinates are expressed in θ and all the geometry corrections are implemented

7.2 Generated radiative events

For the study of radiative Bhabha scattering, the Bhlumi (version 2 01) event generator is used At the generator level a Bhabha event sample is selected according to the selection criteria described in the previous chapter For each event of this sample, the energies and momenta of all

[1] Theoretically photons from initial and final state radiation are indistinguishable the expressions initial state and final state are only used to label the two selected event samples

generated photons are added to yield the total photon energy and momentum. Events with a total photon energy of less than 10% of the beam energy are rejected from the sample of radiative events. The polar angle of the total photon momentum vector is used to tag the selected events: Initial state radiation if the polar is below 20 mrad and final state radiation if the polar angle is in the 32-55 mrad range (approximately the fiducial volume used for the luminosity analysis in the previous chapter).

Figure 7.1 shows the energy distribution for all selected Bhabha events and for those classified as initial and final state radiation. Photons which are classified neither as initial state nor final state events, since they are in the polar range from 20-32 mrad explain the events in the tail.

Given the L3 detector geometry the initial and final state radiative event samples, with a photon energy larger than 0.1 E_{beam}, amount to about 7% and 1% of the selected Bhabha sample respectively. This already provides a quantitative estimate on the relative importance of the radiation effects. It also explains why care is required to avoid biases in the Bhabha event selection due to initial state radiation effects.

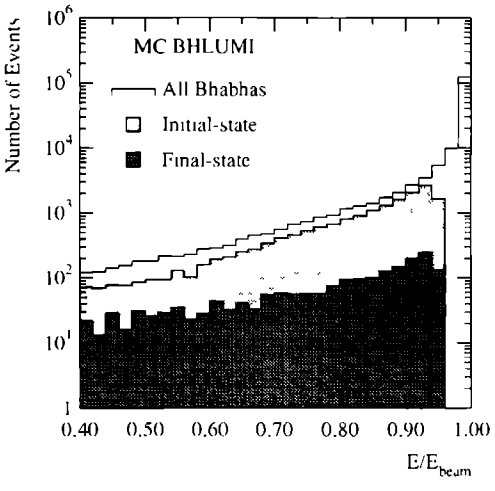

Figure 7.1: *Energy distribution for the generated Bhabha events. The events with initial state radiation or with final state radiation are separately hatched.*

7.3 Final state radiation

In this analysis all the reconstructed clusters in the BGO are considered seperately. The kinematic variables (E, θ, ϕ) of these clusters are defined as described in section 5.3.2. The first indication of a final state event is the presence of a second cluster in one of the two calorimeters. Events with more than two bumps at one side are mainly caused by double final state radiation or an additional photon produced in the material preceding the detector. These events are rejected.

A typical $e^+e \rightarrow e^+e\,\gamma$ event is shown in figure 7 2 Three distinct electromagnetic showers can be identified within the BGO calorimeter The BGO calorimeters alone do not allow a distinction between a γ and an $e^{\pm}$ Therefore the photon is identified as the least energetic of the two showers Using the silicon tracker for electron identification leads to asymmetries in the data and Monte Carlo sample since the amount of material in front of the detector is slightly different Only photons with an energy exceeding 0 1 E_{beam} are retained

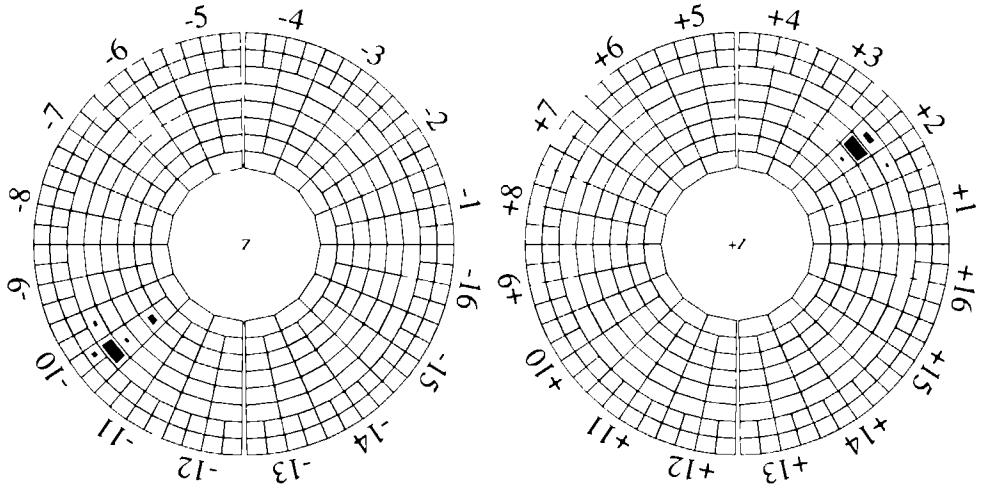

Figure 7.2: *Example of a $e^+e \rightarrow e^+e^-\gamma$ event with all three particles detected in the luminosity monitor On the $-z$ side two separate clusters can be distinguished on the $+z$ side all the energy is contained in one shower*

The fiducial volume requirement ($32 < \theta < 55$ mrad) is applied on the most energetic particle as in the standard luminosity analysis, thus allowing the examination of the same event sample To retain more final state events than in the standard Bhabha sample the particles reconstructed within a single BGO calorimeter are subsequently combined into a single particle' via a vector summation of the two sets of kinematic variables The nominal coplanarity and energy requirements are calculated using the kinematic variables of this particle The summation is only used to apply these cuts, the clusters are still separately identified as photon (least energetic cluster) and electron (most energetic cluster)

For a genuine radiative Bhabha event the sum of the energy of the photon, F_γ, and the energy of the electron (or positron), E_e, must be close to the beam energy If the energy of the two clusters, shown in figure 7 3 (left), is examined a background is observed formed by events with in total more than the beam energy This contamination is caused by coincidences of off momentum particles and real Bhabha events Although the number of background events is small compared to the Bhabha sample used in the luminosity analysis it is the major concern in the final state radiative event selection since these events are specifically selected with the requirement of two BGO clusters at one side

To separate the radiative events from this background the following additional cuts are used:

$$0.9 < E_\gamma + E_{\text{electron}} < 1.1 \quad (7.1)$$

$$E_\gamma > 0.10 \quad (7.2)$$

The effect of these cuts is shown in figure 7.3 (left). In figure 7.3 (right) the measured differential cross section for final state radiation is shown as a function of the photon energy. The cross section is summed over both sides of the detector. The same plot also shows the result of a simulation based on the Bhlumi Monte Carlo event generator and the L3 detector simulation package. The cut-off at $E_\gamma = 0.5$ is due to the specific requirement used to identify the photon. A few events are observed with a photon energy above 0.5 E_{beam} because the reconstructed energy is sometimes slightly above the total beam energy. Data and simulation are in excellent agreement.

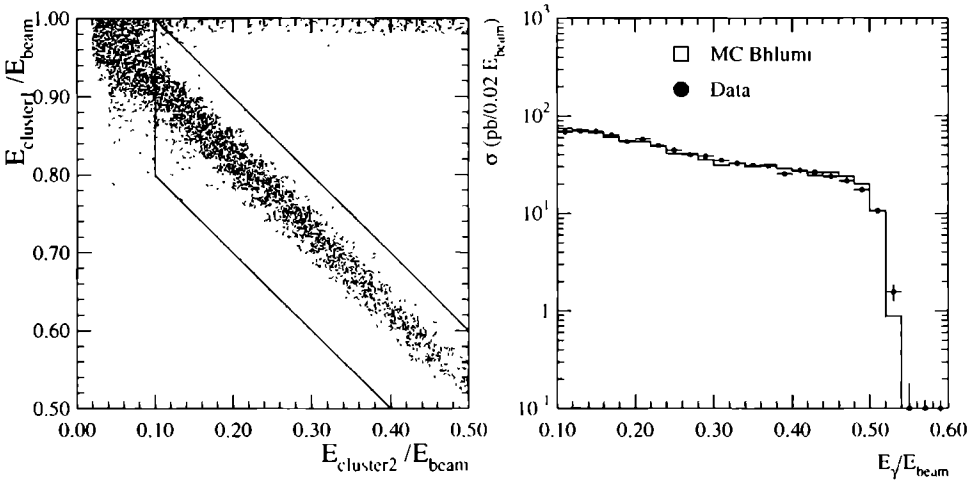

Figure 7.3: *The energy of the most energetic cluster versus the energy of the least energetic cluster (left). The solid lines indicates the selection cuts. The differential cross section for final state radiation (right).*

The ratio of the integrated cross section above $E_\gamma = 0.10$ is:

$$\frac{\left[\int_{0.1}^{\infty}(d\sigma)/(dE_\gamma)dE_\gamma\right]_{\text{data}}}{\left[\int_{0.1}^{\infty}(d\sigma)/(dE_\gamma)dE_\gamma\right]_{\text{MC}}} = 0.993 \pm 0.010 \pm 0.013 \quad (7.3)$$

where, the first uncertainty is the statistical error and the second uncertainty is due to a systematic uncertainty. This systematic uncertainty includes a contribution due to geometric differences between the data and the Monte Carlo.

Due to selection of events with two, and not more than two, bumps in one calorimeter some events have been rejected where a coincidence occurred between a final state event and background event. An estimate of these events is made by the comparison of the data and Monte Carlo

samples with three clusters at one side In the Monte Carlo sample these events are only double final state radiative events In the data there is an additional contribution from background events The total amount of falsely rejected events is estimated to be less than one percent consistent with assigned systematic error

The modelling of the final state radiation in the Monte Carlo is compared with the differential cross section observed in the data, to an accuracy of a percent Since the total fraction of the final state events from all selected Bhabha events is only 2% this already ensures that the systematic effect on the luminosity measurements is negligible

7.4 Initial state radiation

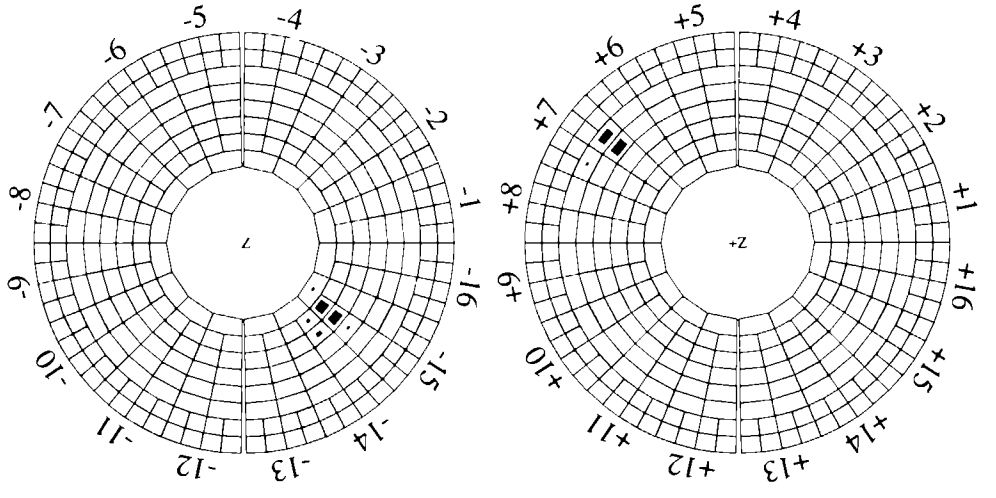

Figure 7.4: *Example of a $e^+e \rightarrow e\ e\ (\gamma)$ event In this case the presence of a photon is deduced from the apparent energy-momentum imbalance The missing energy on the $-z$ side is 0 28 E_{beam}*

A typical $e^+e^- \rightarrow e^+e\ (\gamma)$ event candidate where the photon escapes along the beam line, is shown in figure 7 4 These events are characterised by the presence of two energy deposits in the BGO calorimeters of the luminosity monitor one with an energy close to the beam energy and one on the opposite side of the interaction point with an energy substantially smaller than E_{beam}

The selection of events is the same as the Bhabhas for the luminosity sample except for one difference the tight-loose selection is abandoned for these acollinear events The reconstructed impact points on both sides of the interaction point are needed to reconstruct the total event and therefore the fiducial volume is chosen such that it is completely covered by the silicon To stay as close as possible to the event sample used in the luminosity calculation the cut is again $32 < \theta < 55$ mrad, but the electron and the positron must be inside this volume

Conservation of transverse momentum imposes the following constraints on the measured energies ($E_{1,2}$) and the measured polar angles, ($\theta_{1,2}$) corresponding to the electron and the positron

Assuming a photon escapes along the beam line with energy E_γ and no transverse momentum, the following equations hold

$$\begin{aligned} 2E_{\text{beam}} &= E_1 + E_2 + E_\gamma \\ E_\gamma &= E_1 \cos\theta_1 + E_2 \cos\theta_2 \\ E_1 \sin\theta_1 &= E_2 \sin\theta_2 \end{aligned} \tag{7 4}$$

These relations are used to employ a kinematic fit to test the hypothesis that the complete event consists of the observed electron and positron together with the 'missing' photon Based on these equations, the following χ^2 is defined

$$\chi^2 = \sum_{i=1\,2} \frac{(E_i - E_i^{meas})^2}{(\Delta E_i)^2} + \frac{(\theta_i - \theta_i^{meas})^2}{(\Delta\theta_i)^2} \tag{7 5}$$

The electron (and positron) energies and the polar scattering angles are varied around their measured values to minimise the χ^2 At this minimum the optimal photon energy is obtained as well as improved values for the scattering angles and energies

The errors on the energy measurement (ΔE_i) are calculated using the energy resolution of 1 3% The errors on the polar angles,($\Delta\theta_i$) are the combined errors on the intrinsic position resolution of the detector and the offsets between the detectors on both sides of the interaction point The intrinsic resolution differs per pitch region and is given by the stripwidth/$\sqrt{12}$ Since the photon energy is determined for each event seperately with the kinematic fit these detector offsets do not cancel The detector position is known with a precision of 0 1 mm in the transverse plane and 1 1 mm in the longitudinal direction The resulting geometry error on the measured polar angle is 0 13%

After the χ^2 has been minimised the confidence level is calculated, see figure 7 5 (left) For genuine initial state radiative events the expected distribution is expected to be flat Events which can not be explained with a photon escaping along the beam pipe are seen in the figure as a large peak at small confidence levels and are rejected from the final sample The measured differential cross section for initial state photon radiation is given in figure 7 5 (right) In the same figure also the result of the simulation is given The abrupt drop above 0 35 E_{beam} is caused by the size of the fiducial volume Events which such hard initial state photons are so acollinear that only the electron or the positron is contained inside the volume and the events are therefore rejected The data and the simulation are in good agreement Only events with a fitted photon energy exceeding 0 10 are kept

Again the comparison between data and Monte Carlo is quantified by the ratio of the integrated cross sections above $E_\gamma = 0\ 10$

$$\frac{[\int_0^\infty (d\sigma/dE_\gamma) dE_\gamma]_{\text{data}}}{[\int_0^\infty (d\sigma/dE_\gamma) dE_\gamma]_{\text{MC}}} = 0\ 980 \pm 0\ 007 \pm 0\ 012 \tag{7 6}$$

the first uncertainty is again the statistical error and the second uncertainty is due to systematic uncertainties The systematic error is estimated by variation of the energy scale of the data with respect to the Monte Carlo The uncertainty in the absolute energy calibration is estimated by comparing the energy distribution of the non radiative Bhabha events in both Monte Carlo and data and is found to be 0 1% The corresponding systematic error on the radiative event sample is 1 2%

For the luminosity calculation this effect is negligible since in this case the cut is in the tail of the energy distribution. If the asymmetric energy requirements of 0.4 E_{beam} and 0.8 E_{beam} are varied in the data sample with 0.1% the resulting change in the luminosity is only 0.01% which is compatible with the error assigned to the energy requirement in the selection procedure.

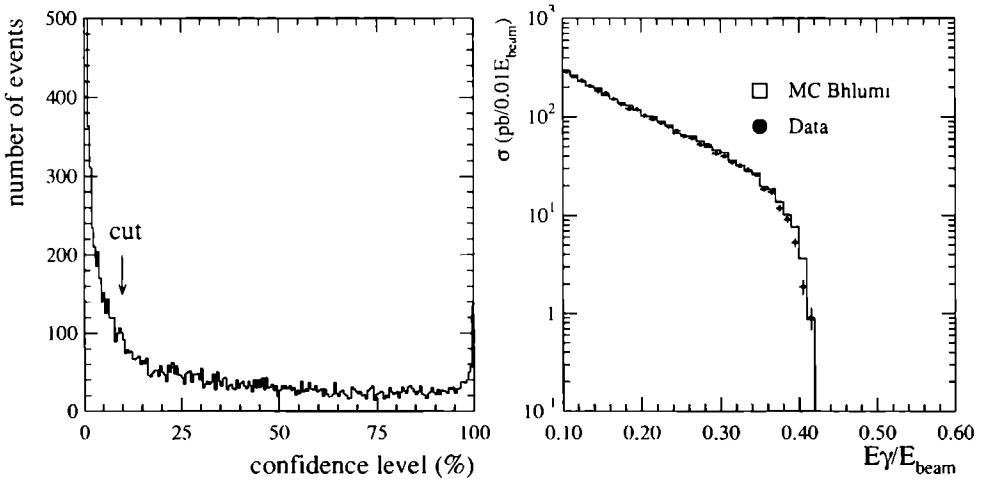

Figure 7.5: *(left) Confidence level of the fitted photon events. (right) Differential cross section for initial state radiation.*

Summary

In this thesis a detailed description is presented of the luminosity measurement at the L3 experiment in the LEP ring. The process used for the luminosity measurement is small angle Bhabha scattering. In 1993 the L3 luminosity detector was upgraded with a silicon strip detector installed in front of the existing BGO calorimeter.

The silicon strip sensors used for the detector are carefully tested. It has been found that the leakage current through the strips is low, in the order of 10 nA/cm^2. The surface current is not negligible and can even increase to several μA per sensor. The performance of the sensors is not affected since the current is absorbed by the guard ring. In the L3 detector the depletion of the sensors must be monitored constantly to avoid signal loss due to a drop in the effective bias voltage over the sensor.

In 1992 the silicon detector has been tested in a 50 GeV electron test beam. From the test beam data it is concluded that the performance of the detector is good: the average signal to noise ratio is 14, and less than three percent of the traversing particles cause hits on adjacent strips. It is also shown that the alignment pins on the support structure lead to an increased level of multiple hits in a region of several millimetres around the pins.

The first year of operation of the silicon detector was successful. Only four of the 8192 strips were found to be dead and four other strips showed such a noisy behaviour that they could not be used in the data analysis.

The visible cross section of the Bhabha process in the luminosity detectors is determined using the Monte Carlo generator Bhlumi. The systematic uncertainty on this cross section is 0.16%. Since the simulation of Monte Carlo events is very CPU time consuming only a limited number of events can be simulated. The statistical error on these events is included as a systematic effect and is 0.09%

The experimental uncertainties in the luminosity determination are mainly determined by a finite knowledge on the positions of the sensors on the support structure (9 μm) and a problem with the rigidity of the detectors in the z direction (1.6 mm). The contribution of these effects to the total uncertainty in the luminosity determination are 0.03% and 0.06% respectively.

The Bhabha scattering events with in addition to the electron and the positron, a photon are of special importance for the luminosity determination. A distinction is made between 'initial state' photons and the 'final state' photons, produced in the angular region below 20 mrad and the region between 32 and 55 mrad respectively. The determination of the cross section for the radiative photons is mainly limited by the uncertainty in the absolute energy scale. The agreement between the data and Monte Carlo is found to be 1%.

The overall experimental uncertainty in the luminosity measurement with the L3 detector is 0.08%.

Samenvatting

In dit proefschrift wordt een gedetailleerde beschrijving gegeven van de helderheidsmeting bij het L3 experiment in de LEP opslagring Het proces dat wordt gebruikt om deze helderheid te meten is Bhabha verstrooiing onder kleine hoeken

In 1993 werd de helderheidsdetector van het L3 experiment verbeterd met silicium strips die voor de bestaande BGO calorimeter zijn geplaatst Deze silicium strip sensoren zijn uitgebreid getest De lekstroom door de strips is laag, in de orde van 10 nA/cm^2 Er wordt echter een significante oppervlakte stroom waargenomen die op kan lopen tot enkele µA per sensor Het gedrag van de sensoren wordt hierdoor niet aangetast omdat deze oppervlakte stroom geabsorbeerd wordt door een extra strip die aan de rand van de detector loopt, de 'guard ring' Het gevolg is wel dat de effectieve spanning over de sensoren voortdurend bewaakt moet worden om te voorkomen dat het signaal kleiner wordt door een vermindering van de depletie van de sensor

In 1992 is de silicium detector getest in een testbundel van 50 GeV electronen Uit de gegevens van deze test kan geconcludeerd worden dat de detector zich goed gedraagt de signaal ruis verhouding is 14 en in slechts drie procent van de gevallen leidt een passerend deeltje tot een signaal in een van de aangrenzende strips Tevens wordt aangetoond dat de uitlijn-pinnen op de draagstructuur leiden tot een vermeerdering van het aantal gevallen waarin op meerdere strips een signaal wordt gemeten, in een gebied van enkele millimeters rond deze pinnen

Het eerste jaar dat de silicium detector is gebruikt was succesvol Slechts vier van de in totaal 8192 strips bleken niet te functioneren en vier andere strips vertoonden zoveel ruis dat ze niet bruikbaar waren in de analyse van de gegevens

De werkzame doorsnede van de Bhabha verstrooiing, zichtbaar met de helderheids detectoren is bepaald met het Monte Carlo programma Bhlumi De systematische onzekerheid in deze werkzame doorsnede is 0 16% Omdat de simulatie van de detectorrespons op deze verstrooiingsprocessen zeer veel CPU tijd vergt is slechts een beperkt aantal gevallen gesimuleerd De statistische onzekerheid is daardoor 0 09% en wordt als extra systematische onzekerheid in de helderheidsmeting toegekend

De experimentele onzekerheid in de helderheidsmeting wordt hoofdzakelijk bepaald door een eindige kennis van de positie van de sensoren op de draagstructuur (9 µm) en een probleem met de stijfheid van de draagstructuur in de richting van de bundelas (1 6 mm) De bijdragen van deze effecten tot de totale onzekerheid zijn respectievelijk 0 03 % en 0 06 %

De gevallen van Bhabha verstrooiing waarin naast het electron en het positron ook een foton wordt geproduceerd zijn erg belangrijk voor de helderheidsmeting Er wordt onderscheid gemaakt tussen fotonen uit de begin- en eindtoestand, respectievelijk geproduceerd onder een hoek van 20 mrad of minder en een hoek tussen 32 en 55 mrad De bepaling van de werkzame doorsnede van deze processen wordt beperkt door de experimentele onzekerheid in de absolute energiekalibratie van de calorie meter Er wordt overeenstemming tussen data en simulatie aangetoond op het pro

cent niveau

De uiteindelijke experimentele onzekerheid in de bepaling van de helderheid met de L3 detector is 0.08%.

Bibliography

[1] S.L. Glashow, Partial symmetries of weak interactions, *Nucl Phys* , **22** (1961) 579.

[2] S. Weinberg, A model of leptons, *Phys Rev. Lett.*, **19** (1967) 1264.

[3] A. Salam, Relativistic groups and analyticity, *Proc 8th Nobel Symposium Aspenasgarden*, (1968) 367.

[4] LEP working group, Updated parameters from the Z lineshape and asymmetries, internal note LEPLINE 94-01, 1994.

[5] D. Griffiths, Introduction to elementary particles, J. Wiley & Sons, 1987.

[6] A. Arbuzov et al., Small angle Bhabha scattering for LEP, CERN 95-03, 1995.

[7] D. R. Yennie, S. Frautschi and H. Suura, The infrared divergence phenomena and high-energy processes, *Annals of Phys.* **13** (1961) 379-452.

[8] S. Jadach et al., QED multi-photon corrections to Bhabha scattering at low angles. Monte Carlo solution., *Phys. Lett.*, **B268** (1991) 253,
S. Jadach et al., Monte Carlo program Bhlumi-2.01 for Bhabha scattering at low angles with YFS exponentiation., *Comp Phys. Comm.*, **70** (1992) 305.

[9] S. Jadach et al., Higher-order radiative corrections to low angle Bhabha scattering. the YFS Monte Carlo approach, *Phys Lett.*, **B353** (1995) 362,
S. Jadach, W. Placzek and B. F. L. Ward, Precision calculation of the γ-Z interference in the SLC/LEP luminosity process, *Phys Lett* , **B353** (1995) 349.

[10] J. R. J. Bennett et al., Design concept for a 100 GeV e^+e^- storage ring (LEP), CERN 77-14, 1977.

[11] S. Meyers, The LEP collider, from design to approval and commissioning, CERN 91-08, 1991.

[12] S. Meyers, LEP status and plans, SLAC preprint, SL 95-066, 1995

[13] The working group on LEP energy, The energy calibration of LEP in the 1993 scan, CERN-PPE 95-10, 1995.

[14] R. Bailey et al., LEP operation in 1993 with the Pretzel scheme, *Proc of the fourth European Particle Accelerator Conference*, London, June 27 - July 1 (1994) 439-441.

[15] L3 collaboration, The Construction of the L3 experiment, *Nucl Instr & Meth* **A289** (1990) 35 102

[16] L3 collaboration, Results from the L3 experiment at LEP, *Phys Rep* , **236** (1 & 2) (1993) 1 146

[17] LEP survey group, private communication with J C Gayde

[18] J A Bakken et al , Results on the calibration of the L3 BGO calorimeter with cosmic rays, CERN-PPE 93 184,1993

[19] M Merk, Study of Bhabha scattering at the Z^0 resonance using the L3 detector, PhD thesis, University of Nijmegen, 1992

[20] I C Brock et al , Luminosity measurement in the L3 detector at LEP, submitted to *Nucl Instr & Meth* , 1996

[21] G Bellini et al , Live target performances in coherent production experiments, *Nucl Instr & Meth* , **107** (1973) 85-92

[22] J Kemmer, Fabrication of low noise silicon detectors by the planar process, *Nucl Instr & Meth* , **169** (1980) 499-502

[23] E H M Heijne et al , A silicon surface barrier microstrip detector for high energy physics, *Nucl Instr & Meth* , **178** (1980) 331-343

[24] F Sauli, Instrumentation in high energy physics, World Scientific, London, second edition, 1992

[25] P G Rancoita, Silicon detectors in high energy physics, *Riv della Nuovo Cimento*, **Vol. 5** (1982) Nr 7

[26] W L Brown, Introduction to semiconductor particle detectors, *IRE Trans Nucl Sci* , **Vol. NS8** (1961) Nr 2

[27] Particle Data Group, Review of Particle Properties, *Phys Rev* **D50** (1994) Part I

[28] M S Longair, High Energy Astrophysics, Vol 1, Cambridge University Press second edition, 1992

[29] A N Kalinovsky, Passage of high energy particles through matter, American Institute of Physics, New York, second edition, 1989

[30] T Ferbel (editor), Experimental techniques in high energy nuclear and particle physics, World Scientific, New York, second edition, 1991

[31] G Keil and E Lindner, Low-noise oxide passivated p+n silicon detectors, *Nucl Instr & Meth* , **101** (1972) 43 46

[32] F. Goulding and W Hansen, Leakage current in semiconductor junction radiation detectors and its influence on energy resolution characteristics, *Nucl Instr & Meth*, **12** (1961) 249-262

[33] S. M Sze, Physics of semiconductor devices, Wiley Interscience, New York, second edition, 1981.

[34] G. Raven, Measurement of Invisible Z decays, PhD thesis, University of Utrecht, 1995.

[35] F. Beissel et al , Construction and performance of the the L3 central tracking detector, *Nucl Instr & Meth* **A332** (1993) 33.

[36] E. Beuville et al , A low-noise, low power analog CMOS signal processor for multi-element silicon particle detectors, CERN-EF 89-09, 1989

[37] M N. Kienzle - Focacci, L3 user guide, Version 2, 1992

[38] The L3 detector simulation is based on GEANT Version 3.15 See R Brun et al., GEANT 3, CERN-DD/EE 84-1 (revised), 1987

[39] G. von Holtey, Estimates of particle backgrounds at the LEP detectors, CERN/LEP-BI 88-52, 1988.

[40] H. Kuijten, PhD thesis, University of Nijmegen, to be published

[41] S. Dutta et al., Results on electroweak parameters from L3, L3 note 1620, 1994

[42] E. N Koffeman, Improved luminosity measurement in L3 and determination of the number of neutrinos, *Proc of Meeting of the division of particles and fields of the American Physical Society, DPF-94, Aug 2-6 1994, Albuquerque, New Mexico*, World Scientific, **Vol. 1** (1995) 404-407

Acknowledgements

Without the support of all technicians and physicists who created LEP and L3 the work described in this thesis would not have been very meaningful

Special thanks I would like to express to those who introduced me to high energy physics and CERN Marcel Merk and Frank Linde, I learned a lot every time you disagreed with each other

In many discussions Piet Duinker stimulated me to see things in a wider perspective Gerjan Bobbink I would like to thank for many useful suggestions for trouble-shooting Gerhard Raven en Bram Bouwens made me appreciate the virtues of UNIX

From the first day I arrived in Geneva, Marcel and Esther Merk supported me in an invaluable way At CERN I especially enjoyed the cooperation with all the colleagues of the Carnegie Mellon University Without Ian Brock I would not have enjoyed making plots as much as I did Yorgos Tsipolitis and Helmut Vogel gave me much friendly advice

At NIKHEF I always felt welcome in the electronics department, with or without questions Special thanks to Paul Rewiersma, Henk Groenstege, Marenko Gospic and Arthur de Waard, although I realise I bothered many others From the design and construction department I would like to thank Henk Schuylenberg, Ilja Cerjak, Joop Buskens, Joop Roverkamp and Arnold Rietmeyer who made a large effort to swallow all our last minute changes

A very special connection I feel with my fellow writers Monty, Hoite en Rob, Erwin Good luck to Jan

Thanks to my family and most of all to Marcel who must have suffered whenever I had problems with one of the people listed above!

Els Koffeman was born in 1967 in Nuenen. During her education she developed a special interest in research. In 1986 she went to the University of Eindhoven to study technical physics. She stayed a short time in Paris at the laboratory of musical acoustics of the "Université Paris VI". She finished university with a study about the application of a nuclear technique on the analysis of small amounts of elements in biological tissue. In 1991 Els Koffeman started to work at the NIKHEF institute in Amsterdam on the development of a silicon strip detector to be used for the luminosity determination at the L3 experiment. For this work she stayed in Geneva in 1992 and 1993. The design and construction of this detector and the analysis of the luminosity are presented in this thesis.In 1995 Els Koffeman started to work on the inner detector for the ATLAS detector which hopefully will be built for the future LHC collider at CERN.